Crystal Plasticity Based Numerical Modelling of Dynamic Recrystallization in Magnesium Alloys

by

Evdokia Popova

A thesis
presented to the University of Waterloo
in fulfillment of the
thesis requirement for the degree of
Doctor of Philosophy
in
Mechanical Engineering

Waterloo, Ontario, Canada, 2015
© Evdokia Popova 2015

I hereby declare that I am the sole author of this thesis. This is a true copy of the thesis, including any required final revisions, as accepted by my examiners.

I understand that my thesis may be made electronically available to the public.

Abstract

The automotive industry has not been able to take full advantage of the lightweight of magnesium, or its alloys, because of its reduced formability at room temperature. In order to enhance the workability of magnesium and restore its ductility, elevated temperature forming needs to be performed. Hot working of metallic alloys is often accompanied by dynamic recrystallization (DRX), whereby the deforming grain structure is partially or completely replaced by new defect free grains during deformation. Dynamic recrystallization allows the final microstructure, as well as the properties of the material (grain size, texture strength), to be controlled. Therefore, DRX can be used as a tool to design a materials microstructure.

Because it would be advantageous to be able to redesign the material properties of magnesium, particularly for the automotive industry, this work takes a step towards such an outcome by presenting a new model that predicts DRX in magnesium. The model predicts DRX in magnesium alloys by using a crystal plasticity based finite element model (CPFEM) coupled with a probabilistic cellular automata model (CA). The CPFEM employs microstructural information obtained by electron backscatter diffraction (EBSD) as input and computes dislocation density evolution corresponding to the active deformation modes. Because DRX proceeds via nucleation of new grains and their subsequent growth, a nucleation criterion based on the local mismatch in dislocation density is employed. Subgrains formed during deformation constitute the nuclei, and only those subgrains that have a boundary with misorientation above a threshold value can grow. The probabilistic CA is used to identify successful nucleation sites. The growth of viable nuclei depends on the difference in the stored energy of the nucleus and the stored energy of the surrounding matrix. As such, the model is developed to predict the texture of magnesium alloys that have experienced dynamic recrystallization solely from the initial texture and the applied strain path.

The model is then extended to include deformation twinning and it can then be used to study its effect on the evolution of DRX. Deformation twinning is activated when the c-axis of hexagonal close packed (HCP) crystal is under a tensile load and leads to the reorientation of the crystal by specific angle. However, rather than including both contraction and extension twins, only extension twins are considered in the model due to their important role during deformation at room temperature and above. Extension twins grow during deformation at ambient temperatures and their influence on the texture formation at elevated temperatures is not well studied. Contraction twins were not included in the model because they are known to have negligible effect on the final texture of magnesium alloys due to their relatively low thickness and inability to grow. In order to investigate

the effect of the extension twins on DRX evolution, a reorientation of the entire element is performed to the dominant twin orientation before DRX is initiated. The approach is similar to the PTR scheme (predominant twin reorientation).

To validate the capability of the developed model, first, tensile simulations are performed on rolled AZ31 commercial magnesium alloy at 300°C. The tensile test along the rolling direction is a slip dominated deformation. The softening behaviour as well as the final texture are compared with available experimental data. Then, in order to activate twinning, the compression test is simulated on the extruded AZ31 alloy along extrusion direction (ED). Various temperatures are simulated to investigate the effect of the twinning at higher temperatures. Finally, the parametric study is accomplished to examine the effect of the different parameters in the model on the evolution of DRX. The simulations with the new model show excellent agreement with experiments presented in the literature.

Acknowledgements

First and foremost, I would like to acknowledge and thank my supervisor Dr. Kaan Inal for his encouragement, support and guidance throughout my PhD. I am grateful for this opportunity to pursue my PhD degree, and without my supervisor this work would not be possible. Thank to Professor Inal, these 4.5 years of my graduate research were on a positive note.

I would like to thank Dr. Abhijit Brahme for sharing his knowledge and wisdom that helped me to overcome the challenges I faced during my graduate studies, for his guidance, advices and friendship.

I am grateful to a good friend of mine and colleague Dr. Yauheni Staraselski, who has been always out there for me when I needed, for his endorsement and great help during my PhD.

I would also like to thank Dr. Raj Mishra for his scientific input and discussions, for providing experimental data, without which this work would not be the same as it is now.

I would like to thank Dr. Mohammed Cherkaoui, Dr. Michael Worswick, Dr. Mary Wells and Dr. Susan Tighe for serving on my committee and providing many helpful comments that helped in the improvement of this thesis.

I would like to acknowledge all my friends, who were like a family to me in Canada.

And last but not least, I would like to thank my parents and relatives back home in Yakutia, without whom I would not be where I am today.

Dedication

This thesis is dedicated to my parents and relatives in Yakutia.

Table of Contents

List of Tables

List of Figures

xii

xiii

xiv

Nomenclature

$\dot{\gamma}_{(\alpha)}$ rate of shear strain on α slip system

$\dot{f}_{(\beta)}$ the rate of the volume fraction of twinning system β

γ_a accumulated shear on all the slip systems

μ shear modulus

ω_{switch} switching parameter

Ω spin tensor

$\rho_{GN(e)}^{\alpha}$ edge part of the geometrically necessary dislocations (GNDs) density

$\rho_{GN(s)}^{\alpha}$ screw part of the geometrically necessary dislocations (GNDs) density

ρ_{GN}^{α} geometrically necessary dislocations (GNDs) density

σ Cauchy stress

τ dislocation line energy

$\tau_{(\alpha)}$ resolved shear stress on the slip system α

τ_c critical resolved shear stress (CRSS)

θ misorientation angle

ξ random number

b Burgers vector

c constant of the order 0.5

F	deformation gradient
F^*	elastic part of deformation gradient
F^p	plastic part of deformation gradient
f_β	volume fraction of twinning system β
H_m	activation enthalpy
$h_{(0)}$	initial hardening rate of the slip system
$h_{(\alpha\beta)}$	latent hardening matrix
$h_{(\beta)}$	hardening rate of the slip system
K	constant of the order 10
L	dislocation mean free path
M	grain boundary mobility
M_0	pre-exponential factor
$m_{(\alpha)}$	plane normal vector of slip system α
N	switching variable for nucleation
n	hardening exponent
N^s	number of slip systems
N^{tw}	number of twin systems
P	stored deformation energy
S	grain boundary energy per unit area
$s_{(\alpha)}$	direction vector of slip system α
T	rotation matrix of the element
v	velocity
v_i^j	velocity of the current element i with respect to its neighbour j

D   strain rate

L   velocity gradient

Chapter 1

Introduction

Magnesium, being the lightest of the structural metals, is receiving significant interest from automotive industry. Because magnesium is 36% lighter than aluminum, and 76% lighter than iron, while also boasting the highest strength-to-weight ratio of all the structural metals (demonstrated in Fig. 1.1), magnesium could be used to replace aluminum in vehicles [1]. By replacing aluminum parts with magnesium parts, vehicle weight can be reduced, and thus, fuel efficiency can be improved.

Currently, the amount of magnesium used in cars ranges between 14 and 26 kg saving about 20% of weight over aluminum [3]. Fig. 1.2 shows an application of magnesium products in a car, which is limited to cast alloys, and it is used in such car parts as steering wheel, transmission panel, gear box etc. The reason for the limited use of magnesium alloys in vehicles is its poor formability at room temperature caused by the low symmetry of the crystal structure and high anisotropy [4].

There are several ways to overcome this problem, the most effective of which are to use rare earth elements in the alloys [5] or to control the microstructure (grain size, texture strength) [6]. The latter can be attained by high temperature deformation, which is accompanied by dynamic recrystallization (DRX).

Dynamic recrystallization takes place during hot working of metallic alloys, which can soften and restore the ductility of the metals [7]. Moreover, recrystallization can be used as a tool to control the final texture and grain size of metals, both of which play a significant role in the formability of the metals [8]. Fig. 1.3 presents an example of the flow curves obtained from tensile tests of Mg AZ31 alloy at various temperatures. At higher temperatures, the elongation can reach more than 100%, while at room temperature failure occurs at a strain of about 20%.
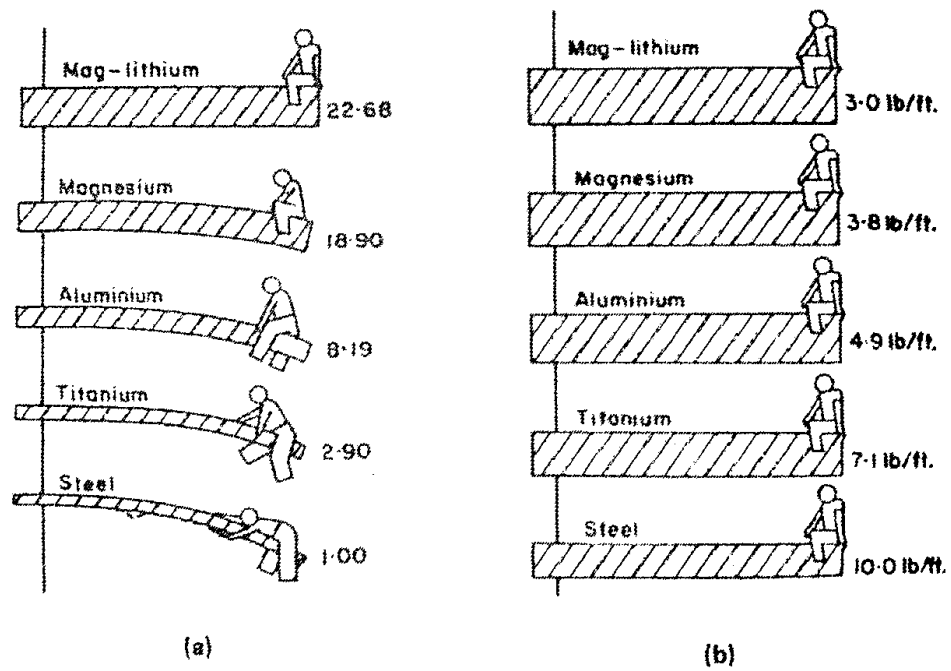
Figure 1.1: Comparison of (a) beams of equal weight and (b) beams of equal stiffness in various materials [2]
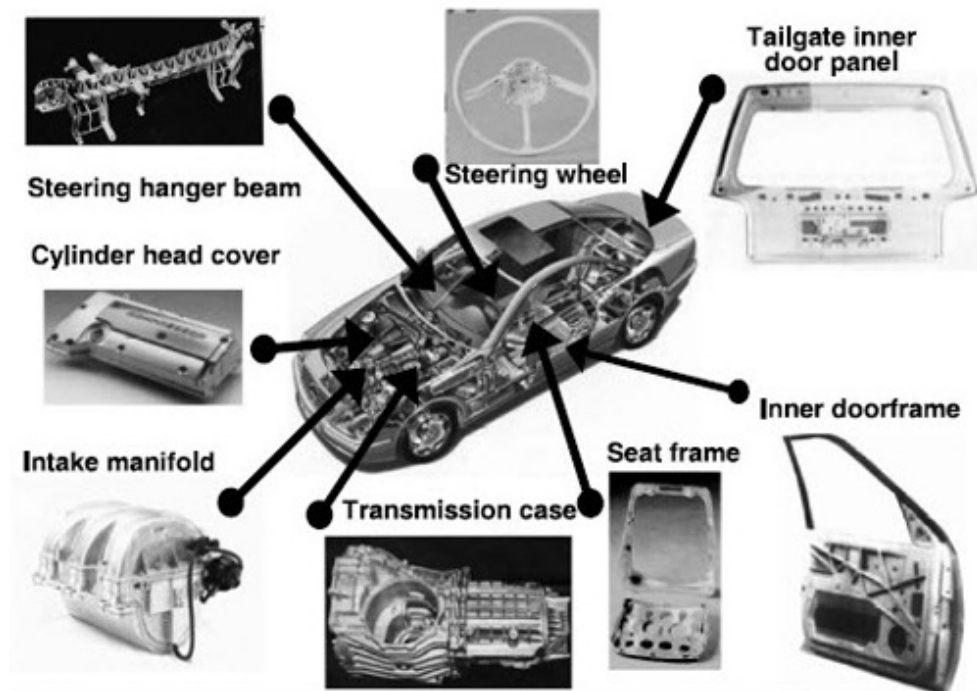
Figure 1.2: Application of magnesium alloys in the car [1]

The process of dynamic recrystallization is a complex phenomenon, which occurs with migration of high angle grain boundaries driven by the stored energy associated with dislocations. DRX plays an important role in the texture formation during an elevated temperature deformation. However, the experimental methods used to provide a processing window for each alloy, as well as the optimal parameters needed to achieve certain characteristics for the alloy (grain size, texture strength) are both time-consuming and expensive. Therefore, the development of a numerical model, which is able to predict and investigate the effect of various DRX parameters on the texture formation in Mg alloys, is needed to save cost, at the very least. Yet, this model can also be used to compliment the experimental techniques that are currently in place.
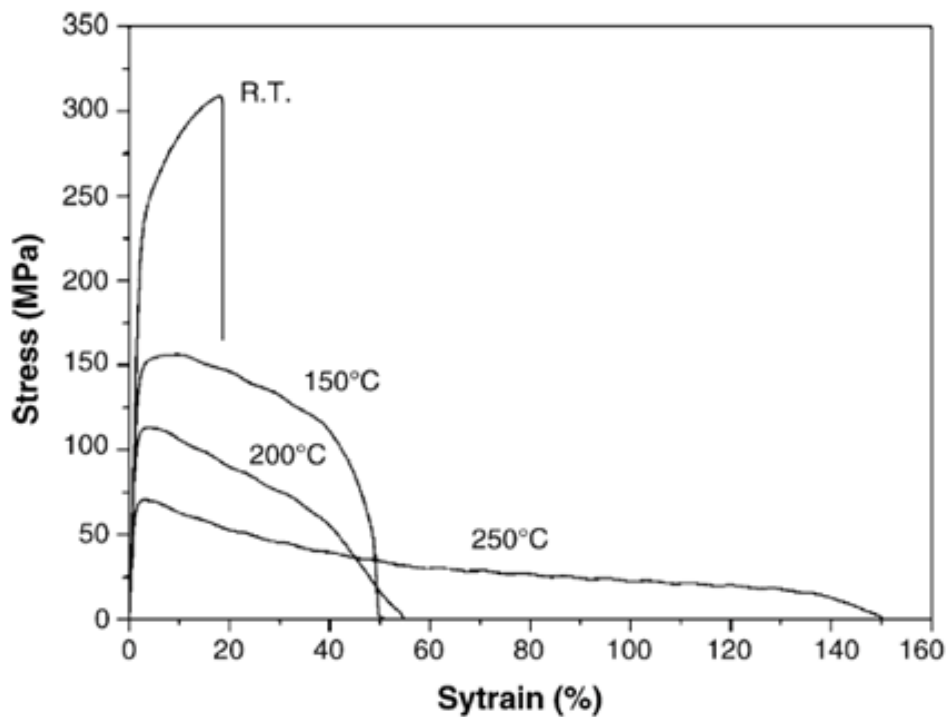
Figure 1.3: Flow stress of magnesium alloy AZ31 deformed at various temperatures [9]

In Mg alloys, DRX is observed at temperatures as low as 150°C. Temperatures lower than 200°C are defined as low temperatures for DRX. Table 1.1 presents the deformation mechanisms that accompany various temperature plastic deformations in Mg.

Numerous computational models to simulate DRX are available, and the most widely used models are categorized as follows: Monte Carlo, Cellular Automata, phase-field and

4

Table 1.1: Governing deformation mechanisms during DRX at different temperature ranges [10]

Temperature	Deformation mechanisms
$< 200C$	twinning, basal slip and $\langle c + a \rangle$ pyramidal slip
$200 - 250C$	cross-slip to form new grains from the subgrains (continuous DRX)
$300 - 450C$	dislocation climb causes bulging of original grain boundaries and sub-grain growth

vertex models. However, most of these are either phenomenological or have restrictions in texture prediction. Yet, the crystal plasticity theory is an established model that accounts for both the initial and the evolving texture of metals. With increasing computational resources, the crystal plasticity framework looks like an attractive tool for modelling polycrystalline materials, because it is able to predict texture development, which is vital in modeling DRX [11].

This research project presents a new model to simulate dynamic recrystallization in HCP metals. The new model is based on a deterministic approach and employs the crystal plasticity finite element method (CPFEM). The main goal of the work is to implement a 2D computational model that is able to simulate texture evolution and mechanical response of magnesium alloys during dynamic recrystallization. The model is a hybrid of the probabilistic cellular automata coupled with the crystal plasticity finite element method. The CPFEM provides a deformation gradient, which is used then to calculate the dislocation density in the DRX part of the code. One of the benefits of using CPFEM is that it can obtain an inhomogeneous distribution of deformation gradient, which is essential in accurately representing the dislocation density. Moreover, the inhomogeneous distribution of dislocation density is also relevant because it can determine the nucleation sites with greater precision. The nucleation criterion employed in the model is based on the local dislocation density mismatch. The growth of the successful nuclei is determined by taking a probabilistic step by a switching parameter based on the grain boundary velocity.

The thesis has the following structure. The important terms used in the work are explained in Chapter 2, which includes the deformation mechanisms in hcp metals and also the recrystallization terms. Then, the literature review on both experimental and theoretical research on DRX is presented in the Chapter 3, where the main types of DRX models are discussed with their major advantages and drawbacks. In Chapter 4, the scope and the main objectives of the work are presented in detail.

In Chapter 5, the modelling framework is introduced. This Chapter is divided into three parts: first, a brief introduction to the finite element method is given, then the

crystal plasticity constitutive model for HCP materials is presented. The crystal plasticity formulation is based on the well-known Asaro-Needleman framework with proposed modification taking into account deformation twinning for HCP metals [12, 13, 14]. This formulation is implemented into a 2D in-house FE code.

The new model for dynamic recrystallization is presented in the next section of the chapter, which is also divided into three parts. First, the nucleation criteria for recrystallization is introduced along with the critical condition for DRX initiation. Second, kinematics of grain growth are given. And, third, the local behaviour of recrystallized grains is analyzed. Various challenges regarding the implementation of the method are also discussed in this chapter.

The main results and their discussions follow in Chapter 6. First, the results of the tensile simulations performed on magnesium alloy AZ31 are presented. This strain path does not involve the deformation twinning, because the c-axis is not under a tensile load, hence, twinning is unfavourable. The next results demonstrate the incorporation of the deformation twinning within the developed model. The results of the compression test simulations of extruded Mg alloy are presented for different DRX temperatures.

Chapter 7 includes a parametric study of the effect of the various model parameters on DRX behaviour. The critical conditions are investigated on their effect on the texture and stress-strain behaviour. While the mobility of the grain boundary is varied between a step function and one-peak function due to the lack of the experimental data for Mg. The effect of the functions on the microstructure evolution is examined.

Finally, conclusions and recommendations for future work are presented in Chapter 8 and Chapter 9 respectively.

6

Chapter 2

Background

2.1 Crystal structure of magnesium

Crystal structures are divided into three types: face centered cubic crystals (FCC - aluminum, copper etc.), body-centered cubic (BCC - steel) and hexagonal close-packed crystal structure (HCP - magnesium, titanium, zirconium etc.) (Fig. 2.1). Magnesium has hexagonal close-packed crystal structure, and hence, more complex deformation mechanisms compared to FCC and BCC metals [15].

body-centred cubic (bcc)   face-centred cubic (fcc)   hexagonal close-packed (hcp)
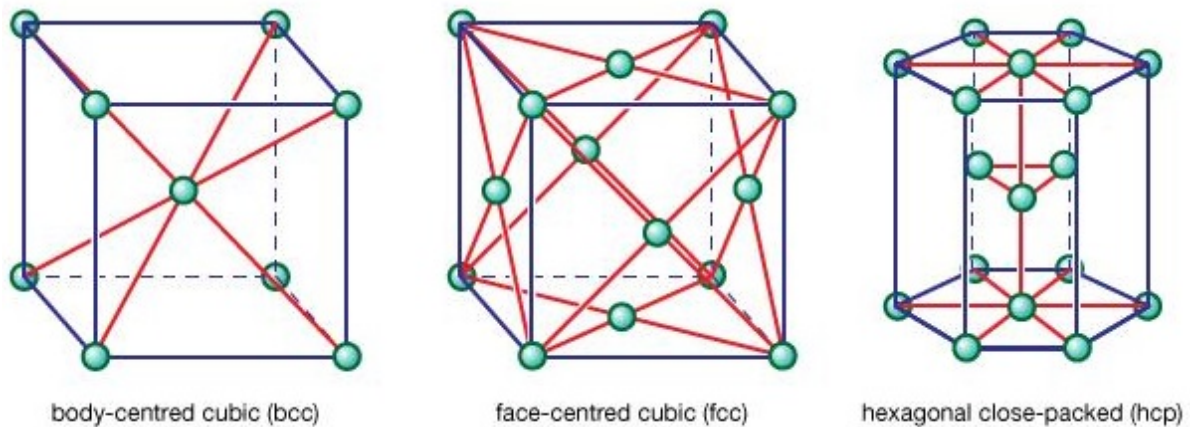
Figure 2.1: Crystal structures: FCC, BCC, HCP [16].

In HCP crystals, there are a_1, a_2, a_3 axes, which have 120° between each other and the c-axis, which is perpendicular to them (Fig. 2.2). In the current framework, these axes are

transformed to the Miller orthonormal coordinate system for calculation convenience using the well-known procedure, which can be found, for instance in [17]. It should be mentioned that the ideal c/a ratio is $\sqrt{8}/3 = 1.633$ (which does not exist in any pure metals) and magnesium has a c/a ratio of 1.624, which is very close to ideal.
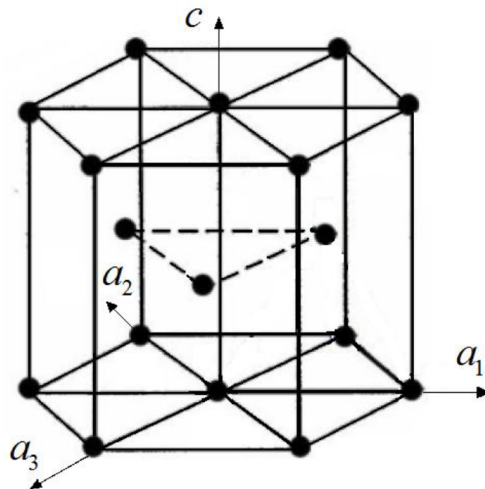
Figure 2.2: Hexagonal close packed crystal axes.

2.2 Deformation mechanisms in HCP crystals

In HCP metals, the major deformation mechanisms are crystallographic slip and deformation twinning. A brief description of each mechanism is given below.

2.2.1 Slip

Slip is a main deformation mechanism in crystallographic materials [18]. When a load is applied, the plastic deformation proceeds by shearing on the slip system (slip plane m and direction s) as shown in Fig. 2.3. The Schmid's law states the condition for slip to occur ('yield' point for crystallographic slip):

$$\tau_c = \pm\sigma_x cos\psi cos\phi \tag{2.1}$$

which is called a *critical resolved shear stress* (CRSS).
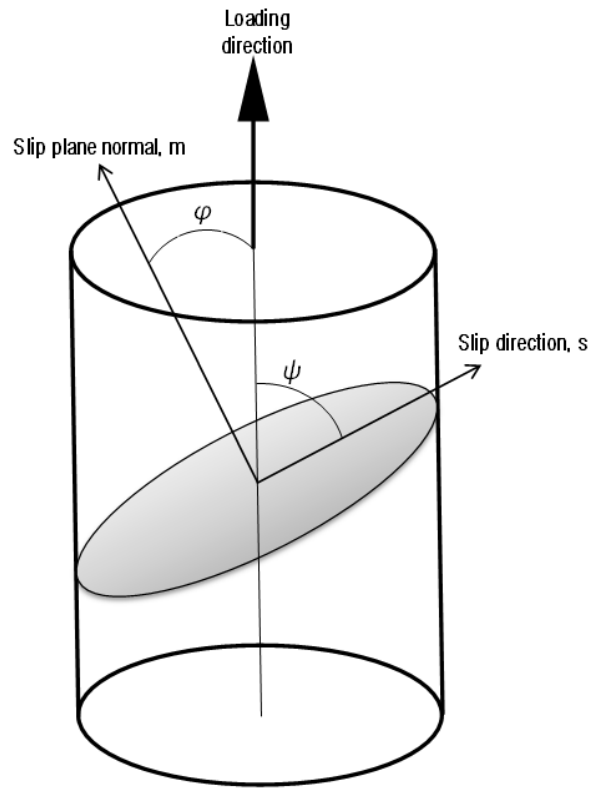
Figure 2.3: Shearing on a slip system [18]

Unlike fcc and bcc crystals, hcp has more complex slip systems. The major slip planes in HCP crystal are shown in Fig. 2.4. Basal slip system is the most active slip system in magnesium alloys and has the lowest CRSS value, while pyramidal $\langle c + a \rangle$ slip system has the highest CRSS at room temperature.
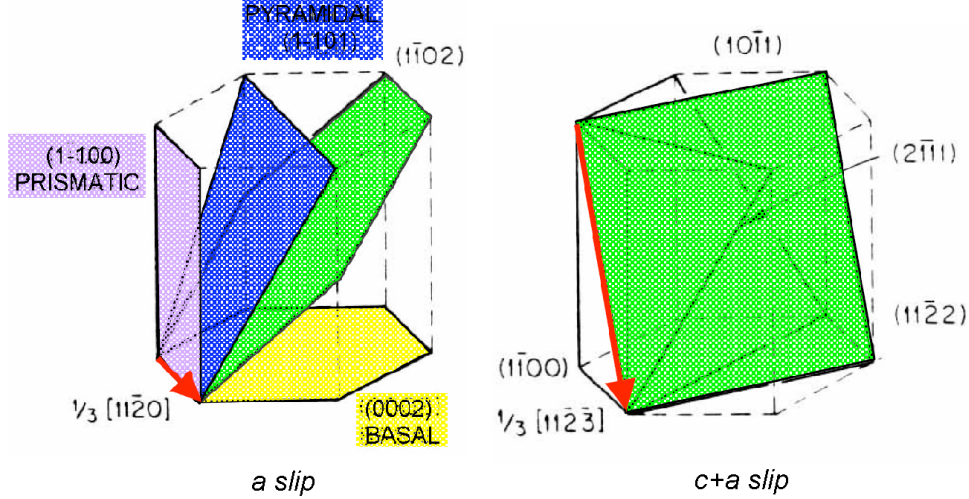
Figure 2.4: Main slip systems in HCP crystal

Note that each slip system, α, is defined by slip plane normal $m_{(\alpha)}$ and slip direction $s_{(\alpha)}$, which are orthogonal vectors.

2.2.2 Deformation twinning

Twinning is a complex deformation mechanism, when the lattice undergoes an abrupt rotation relative to specific planes [18]. The newly formed orientation is a mirrored orientation of the initial matrix grain. The schematic representation of twinning is given in the Fig. 2.5. In HCP metals, twins can be divided into two different types: extension and contraction twins. The extension twin occurs, when the c-axis is under tensile loading, rotating the lattice by 86.6° degrees, while contraction twin occurs when c-axis is under compression and the rotation angle is 56.6°.

The main difference of twinning from slip is a magnitude of rotation. Slip causes a slight rotation to the crystal lattice, while the rotation due to twinning is much larger. Another difference is that the shear displacement due to twinning is one directional, i.e. shear in one direction is not the same as in its opposite direction. Slip can occur on the specific plane in both direction.
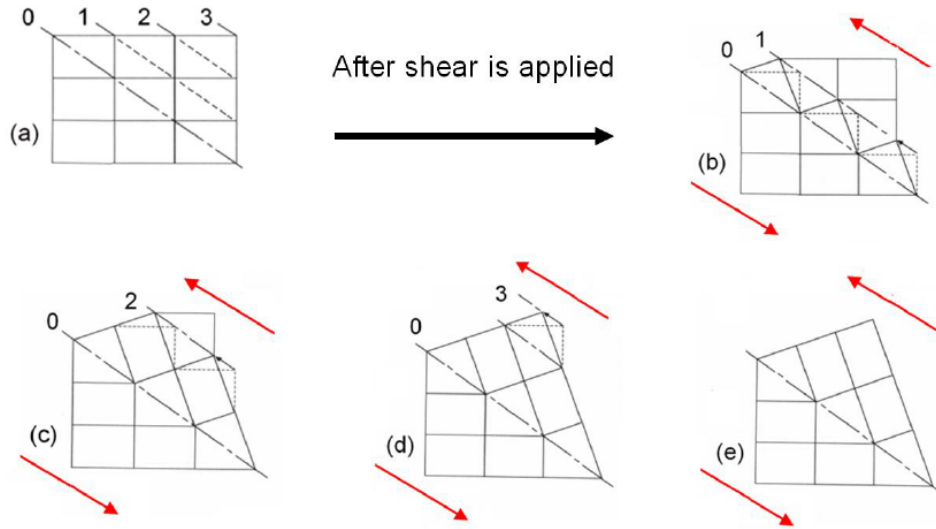
Figure 2.5: Schematic representation of deformation twinning [18]

Table 2.1: Slip and twinning systems used in the model

Slip systems	$\{0001\}\langle1\bar{2}10\rangle$	Basal
	$\{10\bar{1}0\}\langle1\bar{2}10\rangle$	Prismatic $\langle a\rangle$
	$\{1\bar{1}01\}\langle11\bar{2}0\rangle$	Pyramidal
	$\{1\bar{2}12\}\langle1\bar{2}1\bar{3}\rangle$	Pyramidal $\langle c+a\rangle$
Twinning systems	$\{10\bar{1}2\}\langle\bar{1}011\rangle$	Extension twin

2.3   Texture

Crystallite aggregates consist of grains, each of which has its orientation. The distribution of those orientations is usually not random [19]. A preferred orientation of the crystals in the material is called texture. It can be presented in terms of a pole figure. Fig. 2.7 presents a standard projection of the hexagonal planes on the spherical . The pole figure has equivalent 12 sections.
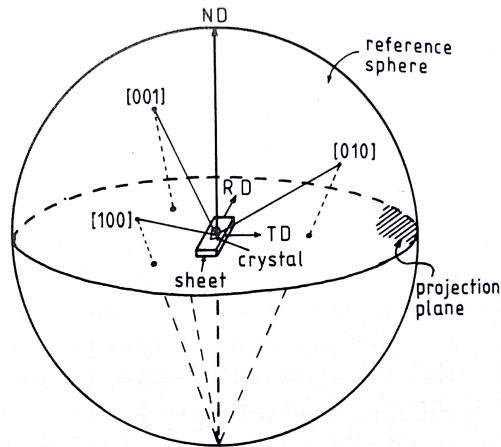
Figure 2.6: Schematic representation of the projection sphere [19]
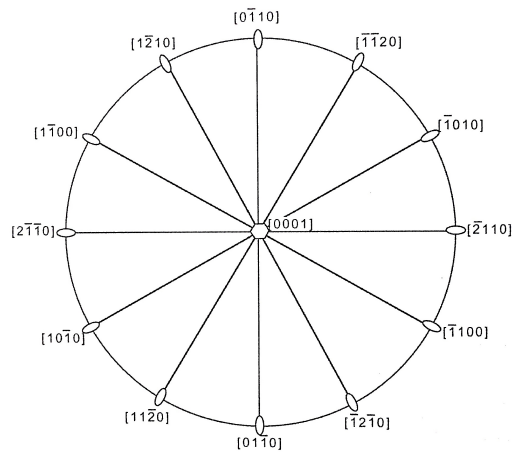
Figure 2.7: Projection of hexagonal crystal orientations [20]
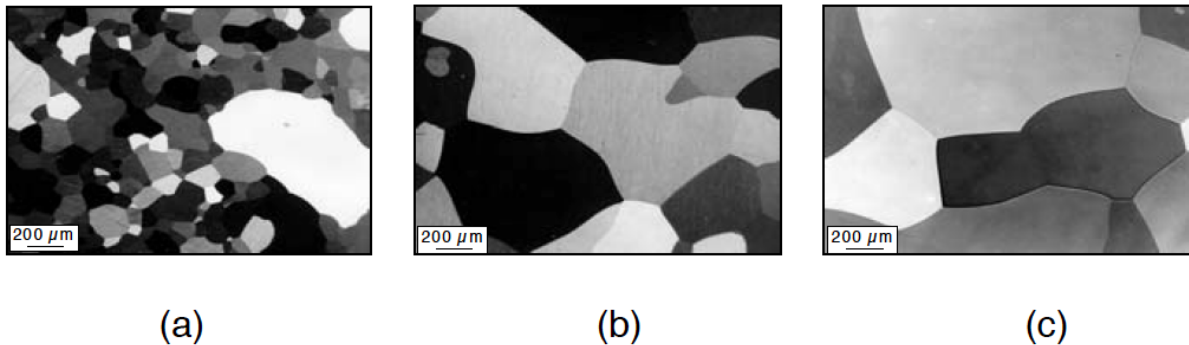
Figure 2.8: Change in microstructure during annealing of Al-0.1% Mn after 95% cold rolling [22].

2.4   Recrystallization

Recrystallization is a collective term to describe the change in orientations of grains by grain boundary motion [21]. It proceeds via formation and migration of high-angle grain boundaries driven by the stored energy associated with dislocations. After plastic deformation, the stored energy renders a driving force for further deformation or the recovery process. Static recrystallization (SRX) happens during annealing treatment of the material, while dynamic recrystallization (DRX) occurs during plastic deformation at elevated temperatures. In Fig. 2.8, a few steps of recrystallization process are shown. As it can be seen from the final microstructure, a few grains have grown consuming the other small grains.

In the literature, dynamic recrystallization mechanisms are divided into two main types, *discontinuous DRX* states for nucleation and growth of high-angle boundaries; *continuous DRX* states for a recovery process of low-angle boundary movement consuming dislocations and forming high-angle boundaries [23].

It is known that DRX and SRX take place by the grain growth phenomenon. *Normal grain growth* is a process when all grains grow roughly at the same rate of boundary migration resulting with almost the same size. *Abnormal grain growth* is the growth of a few orientations (nuclei) at the expense of other grains. An example microstructure of abnormal grain growth is presented in Fig. 2.9. The final microstructure after abnormal grain growth is dominated by those nuclei orientations, and the sizes of recrystallized grains are much larger than the others [21].

13
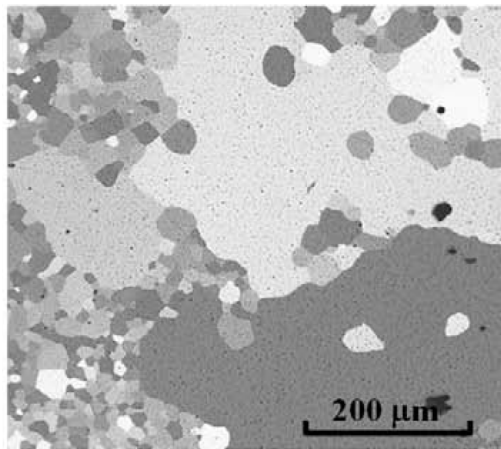
Figure 2.9: Abnormal grain growth showing abnormally large grains along with smaller grains [24].

Chapter 3

Literature Review

3.1 Crystal plasticity models

The crystal plasticity model has been an established tool to simulate the mechanical response of a crystalline material at the grain scale. The following types of the models can be distinguished:

1. **Sachs model** [25] has an assumption of homogeneous distribution of the stress over all the grains in the aggregate.

2. **Taylor type models** [26] assume that all grains in the sample deform the same way, hence, have the same strain distribution.

3. **Self-consistent models** (VPSC, EPSC, EVPSC) [27][28] solve an Eshelby type problem for effective heterogeneous media in an infinite domain.

4. **Crystal plasticity finite element models** [29] [12][30] can account for local strain partitioning.

The Sachs model imposes the direction of stresses in every crystal (eigenvalues) to be equal to the external stress, however, the shear strain in each crystal will not be the same (based on the active slip systems), and therefore, the compatibility is violated [31]. The widely used Taylor model makes the assumption of equal deformation gradient over the polycrystalline material, implying the same deformation in each grain [26]. Although the Taylor model gives a good prediction of the texture evolution, the homogeneous distribution of the strain gradient makes it not suitable for dislocation density calculations.

Another approach, the visco-plastic self consistent model (VPSC) has also been used to simulate the texture evolution of polycrystals during deformation. However, this model does not take into account grain-to-grain interactions. Thus, the three approaches described above do not consider explicitly the interaction between grains in a polycrystal, and they make simplifying assumptions about either the stress or the strain distribution being homogeneous.

The so-called crystal plasticity finite element model (CPFEM) is based on the discretization of the sample, and solve equilibrium of the forces and the compatibility of the displacements [11]. Crystal plasticity model formulations consist of the constitutive equations that consider the anisotropy of the grain deformation, for example, dislocation-density based models [32], mechanical twinning [33] [12][34]. One of the main advantages of the CPFEM is the ability to account for inter- and intra-grain interactions that can be used to calculate the dislocation density distribution. Since the stored deformation energy comprises of dislocations, calculation of dislocation density is one of the major parts in modeling recrystallization. Thus, CPFEM has an advantage over the other models in modeling DRX.

Crystal plasticity models for hexagonal close-packed (HCP) crystal structured metals are more complicated, since HCP materials have more complex deformation mechanisms than FCC or BCC metals. Deformation twinning is one of main challenges while modeling the deformation of HCP metals using crystal plasticity models. Various approaches to incorporate twins within the crystal plasticity models were introduced by Kalidindi [12], Staroselsky and Anand [35], Van Houtte [36], Tome et al. [27]. The problem still remains as one of the 'hot topics' in the computational materials science. In the CPFEM, deformation twinning is implemented as a pseudo-slip mechanism [12], activated based on the Schmid's law. The volume fraction of twins is tracked during the simulations, and the stresses are calculated as a volume average in the twinned region and in the matrix separately.

3.2   Dynamic recrystallization

Numerous experimental and numerical studies have been published to investigate both dynamic and static recrystallization. This chapter gives a brief literature review of the current status of research on recrystallization problem. First, experimental works are reviewed, and then the major types of the models are listed by category. The reviewed literature is mainly for magnesium alloys, which is the primary material of this work.

3.2.1 Experimental Work

Aluminum is already well investigated and established in the automotive industry, whereas magnesium and its alloys are still being studied extensively [37]. Due to the lightweight of magnesium alloys and their potential to reduce the weight of the vehicles, the interest of the automotive industry is high. However, a hexagonal close-packed (HCP) crystal structure and consequent anisotropy makes magnesiums formability poor at room temperature. Therefore, in order to attain the ductility, magnesium alloys have to be deformed at high temperatures [38]. During the elevated temperature forming operations, dynamic recrystallization plays a significant role in the final texture formation as well as the overall formability [39]. Therefore, there is a wide range of experimental studies on dynamic recrystallization in magnesium and its various alloys.

Deformation in magnesium alloys can be divided into slip or twin dominated deformations. For example, during the tensile deformation of AZ31 alloy (pole figure is presented in Fig. 3.1) along rolling (RD) or transverse direction (TD), no prominent twinning is observed, while the compressive test along the same directions results in a twinning texture, whereby almost all the grains undergo twinning [40]. During the elevated temperature deformation, non-basal slip systems are activated, namely, pyramidal $\langle c+a \rangle$ slip systems that provide the additional deformation mechanism, which can suppress twinning [41] [42]. The deformation twinning is most active at room temperature, however, it was also observed during the higher temperature deformations as well [23]. Since dynamic recrystallization in magnesium alloys was reported at temperatures as low as $150°C$ [37], it is important to study the effect of the deformation twinning on DRX.

There are limited works available on deformation twinning behaviour and its effect on texture evolution during DRX. The commercial magnesium alloy $AZ31$ was studied for DRX at different temperatures and strain rates [43, 23, 44]. Most of the DRX experiments reported in literature for AZ31 Mg alloy were performed under uniaxial compression, and various effects of the texture, strain rate and temperature were investigated. The initial texture of $AZ31$ and deformation mode effects were studied in [45, 46, 47, 48]. The experimental results showed that the initial texture has a significant effect on the stress-strain response as well as on the twinning behaviour at different temperatures and strain rates. It was found that deformation twinning active at the beginning of deformation can delay DRX at $300°C$. Proving this observation in another work [49], it was also concluded that $\{10\bar{1}2\}$ twins appeared at the initial stage of the deformation before DRX started and were not dominant deformation mechanisms above $200°C$. It was shown in [45] that the texture evolution is more sensitive to strain rate at 400 C in AZ31 Mg alloy, and a very small amount of twins were observed.
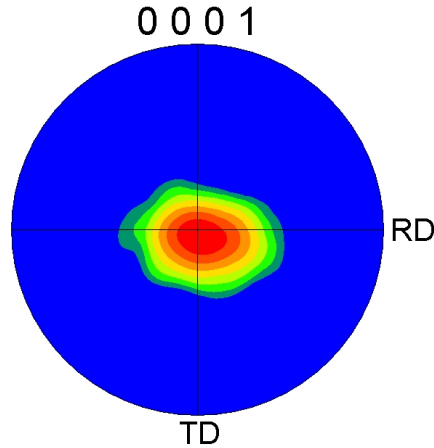
Figure 3.1: {0001} pole figure of commercial magnesium alloy $AZ31$ shows strong basal texture

In [50], the authors assumed that extension twin boundaries are highly mobile, and therefore, that they grow to thicken rather than to serve as a recrystallization site. The same assumption was made in the work by Ma et al. [51], where EBSD analysis showed the presence of twins during an extrusion of Mg AZ61 alloy at 450 C, emphasizing the importance of twins at high temperatures. The major suggestion was that at the elevated temperature extrusion, $\langle c+a \rangle$ type dislocations are generated, which can also be favourable for deformation twinning [52]. However, at the strain rates $\dot{\epsilon} < 0.1s^{-1}$, the effect of the twinning was negligible at high temperature deformation [53]. Some elevated temperature tests also revealed very few twins [23][54] [55], which can be explained by the activation of non-basal slip systems, namely, pyramidal $\langle c+a \rangle$ slip system. The authors in [10] reported active twinning, basal and $\langle c + a \rangle$ slip systems during deformation at < 200 C in ZK60 alloy. Twins were observed in TEM analysis after hot torsion at temperatures between $180 - 360$ C and strain rates 0.01 and $1.0s^{-1}$ [43]. As the temperature decreased, the twin boundaries became less sharp and resulted in serrated boundaries.

Magnesium AZ31 alloy was tested in tension and compression at 200 C and 400 C and strain rates 0.01 and $10^{(-4)}s^{-1}$ in [56]. Texture analysis showed that during 200 C compression test along extrusion direction (ED), most of the grains underwent twinning. The c-axis of HCP crystal was perpendicular to the compressive loading direction, which is favourable for the activation of twinning. The flow curves during the channel die compression of pure Mg and AZ31 alloy revealed the plateau-type behaviour and rapid hardening at the temperatures of 200 C and 300 C and the strain rate $10^{-4}s^{-1}$ in [57] [58]. Usually, this is a sign of active deformation twinning. In [23], the SEM plots were presented with
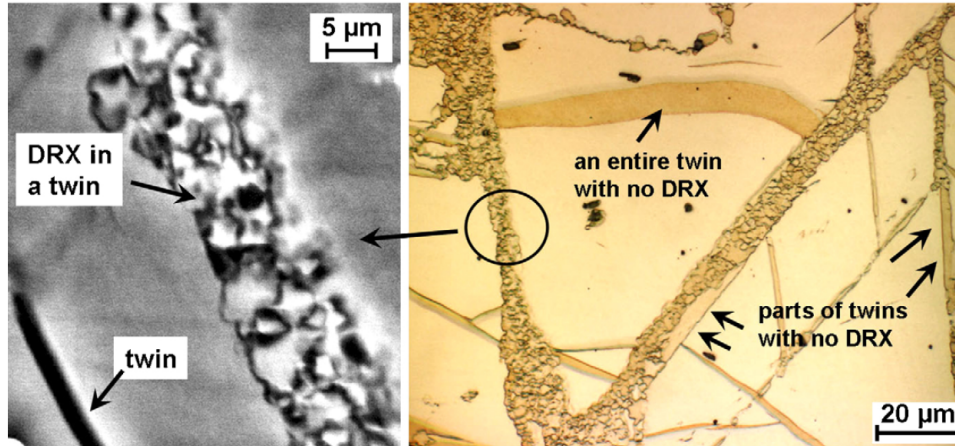
Figure 3.2: Experimental observation of the DRX inside of deformation twinning [23]

extension twins without recrystallization at the end of the deformation (Fig. 3.2). The reason why twins were left unrecrystallized was unknown, however, the authors suggested that they might have appeared during unloading of the sample.

In the other work by Al-Samman et al. [23], it was assumed that the deformation twinning can be a potential nucleation site for DRX, since the stored energy of twinning is higher than in the matrix, and twins also provide a high angle boundary (86° for extension twins). However, recrystallization that occurs inside twin lamellae was restricted within twin area, which was observed in the experimental studies of the single crystal, as in [59] for example (Fig. 3.2). This observation was also confirmed by the other studies of single crystals under compression and tension at different temperatures [60, 61, 62].

Even though compression tests are reported for DRX studies, there is very little data available in the literature regarding tensile tests of AZ31 where DRX was also studied. Thus, texture evolution studies during the tensile deformations at 400 C and 500 C demonstrated that the initial weak fiber texture formed a strong texture after DRX [63]. Analysis of Schmid factors showed that $\{0001\}\langle11\bar{2}0\rangle$ slip system is the most active, but at larger strains, the $\{11\bar{2}2\}\langle11\bar{2}\bar{3}\rangle$ slip system became the most dominant deformation mechanism. These results proved that the non-basal slip system is active at elevated temperatures.

Other experimental research on the tensile deformation of $AZ31$ also showed the presence of non-basal $\langle c + a \rangle$ slip and the preservation of the initial wire texture [9, 64].

Recently, in [65], it was reported that, with increasing temperature and decreasing strain rate during tensile tests of magnesium alloy AM30, twinning was not the main deformation mode. Other magnesium alloys, namely those that include rare earth (RE)

19

metal particles were investigated to evaluate the role of particle-stimulated recrystallization (PSR) in extrusion texture[66]. Second phase particles can initiate the creation of a new orientation, different from the deformed one, and the second phase particles also seem to improve the strain hardening and formability of these alloys. Magnesium alloy $ZK60$ exhibited continuous dynamic recrystallization between the temperature range of $200 - 250$ C and pre-existing grain boundary bulging mechanisms were also observed besides subgrain growth at higher temperatures [10, 67].

The three main conclusions from the experimental literature review are the following:

- At the elevated temperatures, magnesium and its alloys demonstrate the activity of non-basal slip systems, i.e. $\langle c + a \rangle$ pyramidal and prismatic.

- Twinning still plays an important role on the DRX evolution and texture formation at temperatures up to $\sim 300C$.

- Double twins and recrystallized grains inside the twin domains are observed during DRX.

The detailed review of the experimental studies of DRX in magnesium alloys demonstrates the need for accurate models to investigate the DRX phenomenon. It is important to understand which deformation mechanisms are active and which conditions can lead to the preferred/desirable texture of the metals and/or which can restore the ductility. Moreover, there is a need in the research to study the effect of twinning during high temperature deformation to provide insights into the role of twinning during DRX. Since the limit of the experimental tools such as EBSD, TEM, SEM and others are not able to give full picture of DRX mechanisms, physical models can help researchers to explain various phenomena including the nucleation of DRX.

The experimental results and observations reviewed above will be used in the developing the model as well as in the calibration of the model parameters, and the model validation.

3.2.2   Modelling Dynamic Recrystallization

Recrystallization is known to be one of the main processes during the hot working of metals. Experimental techniques on their own are too time consuming and expensive to provide a processing window for each alloy. Therefore, being able to predict the behaviour of the material and microstructure evolution would provide an alternative opportunity to control various material properties [68]. Grain size control and texture development as well as understanding the kinetics of grain boundary motion during plastic deformation are the main

advantages of accurate modelling of DRX [69]. However, the modelling of dynamic/static recrystallization still remains a challenging problem. As computational power increases, new tools become available for modelling DRX phenomenon such as molecular dynamics, atomistic level simulations and crystal plasticity models.

First attempts were taken in early $30s$, when the analytical model was developed by Johnson and Mehl [70], Avrami [71], Kolmogorov [72], which is the so-called JMAK theory. In this model, the volume fraction of DRX was represented by an empirical equation:

$$f_{DRX} = 1 - exp(-kt^n) \tag{3.1}$$

where k is the nucleation rate function, t is the time and n is the Avrami exponent. This analytical expression describes the behaviour of the volume fraction of recrystallized grains with respect to the matrix and it is used by many researchers for model verification.

In [73], a theoretical model for subgrain growth by boundary migration during annealing was developed. The model was applied to two-phase alloys and pure metals. Another subgrain growth model was proposed later in [74] for heavily deformed aluminum. A numerical model to predict stress-strain curve during DRX was developed in [75], where the model took into account dynamic recovery as well as grain size.

However, with the development of powerful computational resources, various new numerical models were developed to simulate the process of recrystallization. As one can expect, each of these models has its own strengths and weaknesses. A number of overview papers are available in the literature on the modeling of both dynamic and static recrystallization [68, 8, 69, 76] . Accordingly, the most known models can be divided into the following groups:

- Monte Carlo models

- Phase-field models

- Vertex models

- Cellular Automata models

A brief literature review on each of these models is presented below, while a detailed overview can be found in [68, 8, 69, 77].

Monte Carlo models

The Monte Carlo probability technique with application to recrystallization was used in the Potts model, which is a modified Ising model [78]. Extensive studies were performed to model recrystallization and grain growth using the Monte Carlo method in [79, 80, 81, 82, 83, 84, 85, 86, 87, 88, 89, 90].

In the Monte Carlo models, the domain is divided into lattice sites by a grid. The index s_i is assigned to each site, and this index is the same within one grain. The schematic representation is given in the Fig. 3.3, where grain boundaries are represented with bold lines. Every lattice site is assigned its state variables. The switching parameter for the Monte Carlo step, ω_{switch}, depends on the energy change ΔE:

$$\omega_{switch}(\Delta E) = \frac{1}{2}\omega_0 \left[1 - tanh\left(\frac{\Delta E}{2kT_s}\right)\right] \tag{3.2}$$

where ω_0 is the reduced mobility between the current s_i and neighbouring s_j sites, T_s is the simulation temperature and k is the Boltzmann constant. According to the Monte Carlo method, a random number $\xi \in [0, 1]$ is generated, and the switch is accepted if $\xi \leq \omega_{switch}(\Delta E)$; when the switch is accepted, the current site s_i takes an orientation of the neighbouring site s_j. The energy of the system is calculated as (consistent with Potts model) :

$$E = \sum_{i=1}^{N} \left(\sum_{j=1}^{n} \frac{1}{2}\gamma(s_i, s_j) + E_s(s_i)\right) \tag{3.3}$$

where E_s is the stored energy and $\gamma(s_i, s_j)$ is the boundary energy which depends on the state of the current site s_i and the neighbouring site s_j, n is the number of the neighbours for the current site and N is the total number of the grid sites.

Monte Carlo models are attractive with their simplicity as a numerical model, and they are relatively easy to implement. Hence, the computational costs of the model are minimal. However, since the update of the microstructure in Monte Carlo models happens randomly, the process of defining correctly the nucleation sites becomes extremely important, since the final texture is highly dependent on the initial determination of the nuclei. Various nucleation models for Monte Carlo simulations were examined in [91, 92]. Another disadvantage of the model is a non-trivial correlation of the simulation time and length with physical time and length. Therefore, there is a need for scaling or matching with experimental data. Possible solutions of this problem were discussed in [93, 94]. Nevertheless, Monte Carlo models are successfully used for grain growth problems as well as dynamic recrystallization modeling, where they showed good agreement with both exper-

9	9	9	9	9	9	9	3	3	3	3	3	3	27	27	27	27	27	27	27	27	27	27	27
9	9	9	9	9	9	3	3	3	3	3	3	3	3	3	27	27	27	27	27	27	27	27	27
9	9	9	9	9	9	3	3	3	3	3	3	3	3	3	3	27	27	27	27	27	27	27	
9	9	9	9	3	3	3	3	3	3	3	3	3	3	3	3	27	27	27	27	27	27	27	
2	2	3	3	3	3	3	3	3	3	3	3	3	3	3	3	14	14	27	27	27	27	27	
2	2	2	3	3	3	3	3	3	3	3	3	3	3	14	14	14	14	14	27	27	27	27	
2	2	2	2	3	3	3	3	3	3	3	3	3	3	14	14	14	14	14	14	14	14	27	27
2	2	2	2	3	3	3	3	3	3	3	3	3	3	14	14	14	14	14	14	14	14	14	14
2	2	2	2	2	3	3	3	3	3	3	3	3	3	3	14	14	14	14	14	14	14	14	14
2	2	2	2	2	2	3	3	3	3	3	3	3	3	3	3	14	14	14	14	14	14	14	14
2	2	2	2	2	2	2	3	3	3	3	3	3	3	3	3	14	14	14	14	14	14	14	14
2	2	2	2	2	2	2	3	3	3	3	3	3	3	3	3	14	14	14	14	14	14	14	14

Figure 3.3: Schematic representation of domain division for Monte Carlo method [68]

imental results and theory [83, 95, 96, 79] Further details on this model can be found in [69, 97].

Phase-field models

Another type of model used to simulate the recrystallization problem is the so-called phase-field models. In this model the phase-field parameter ,η_k, is introduced, which represents the fraction of k phase. The phase-field parameter ,η_k, must satisfy the following condition:

$$\sum_{k=1}^{N} \eta_k = 1, \text{ where } \eta_k \geq 0, \forall k$$

For example, η_k can represent a grain in the polycrystalline aggregate with N grains. In that case, η_k is equal to 1 in the kth grain, and equal to 0 in the other grains. Grain boundary is defined as a separate phase (Fig. 3.4) unlike in MC or CA models, where the boundary is not identified explicitly.

The method is computationally expensive, since it is based on the minimization of the energy, which is represented as a functional of the phase-field variables and their gradients. Therefore, the model is usually limited to 2D applications, however, a modified phase-field model was implemented to allow simulations of recrystallization problems in 3D [98].

23

Figure 3.4: Schematic representation of the domain with grain boundaries in the phase-field model [77]

A multi-phase-field model for dynamic recrystallization (MPF-DRX) was employed in [99], where the deformation of the grain was taken into account by resizing the grid. Their results of single grain growth simulations were in good agreement with theory.

A comparative study of phase-field modeling with Potts model for a grain growth problem was performed in [100]. Both models gave very similar results. Phase-field modeling studies can also be found in [101, 102, 103].

Vertex models

Vertex models (otherwise called front tracking models) were developed for curvature-driven grain growth problems. Comparing to MC or CA models, where the curvature of the grain boundary cannot be well described, vertex models have an advantage of introducing a deterministic grain boundary [104].

In this method, grain boundaries are considered as line segments and connected with vertices. Vertices are located at triple junctions (2D) and assumed to be in equilibrium. A grain boundary is described by its velocity v, which depends on the grain boundary mobility μ and the grain boundary energy γ [77]:

$$v = \mu(\theta, T)\gamma(\theta, T)k$$
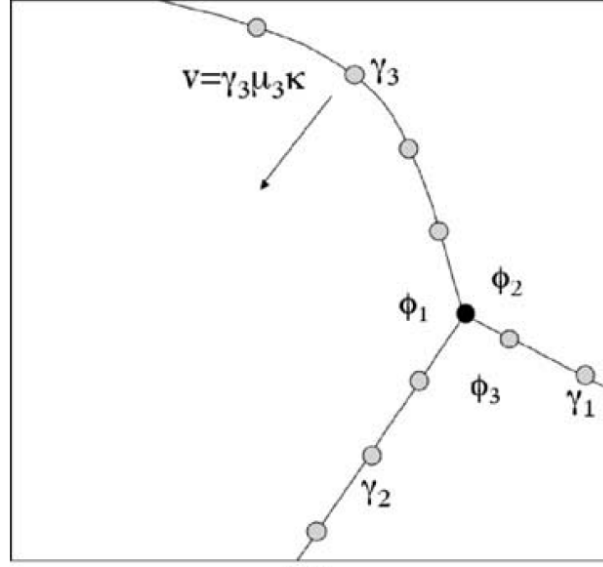
Figure 3.5: Schematic of vertex model grain boundary [77]

where T is the temperature, θ is the misorientation and k is the grain boundary curvature. The triple points are moved to the directions perpendicular to the plane at each time step depending on the transformation rules that are defined. The angles of the nodes ϕ_i can be found from:

$$\frac{\gamma_1}{sin\phi_1} = \frac{\gamma_2}{sin\phi_2} = \frac{\gamma_3}{sin\phi_3}$$

where γ_i are the grain boundary energies. The detailed formulation of the kinematics included in the vertex models can be found in [105].

This technique was used to simulate grain growth problems in [106, 107], while the stored energy along with mobility of grain boundaries was combined in [104] for cold rolled copper, and thus, they were able to model primary recrystallization as well. Simulation results showed good match with experimental data.

Even though the methodology is computationally expensive, 3D vertex models were also implemented and compared with 2D models [108]. The comparison showed that there is a deviation in a small grain size distribution, but 2D model was proved to be valid for the grain growth problems in thin films [109].

Finally, vertex model can also be used to simulate particles or solutes included in the microstructure, treating them as points at the nodes [97].

Overall, the vertex model is an attractive technique to simulate grain growth with improved representation of grain boundary curvature. However, it is not commonly used as MC or CA models because of its complexity of defining the kinematics of the movement of the nodes, as well as translation rules [68].

Cellular Automata

Cellular automata (CA) was first introduced by von Neumann for Turing automata [110]. Later, it was adopted for recrystallization problems [111]. CA method, when applied to recrystallization problems, is based on the discretization of time, physical space, and orientation space. Each discrete cell has its own state variables, which define the current status of the cell. Often dislocation density and crystal orientation are used as state variables in recrystallization problems. CA can be defined on the two- or three-dimensional lattice considering the first, second, and third order neighbor for the calculation of the local driving forces, while an initial state is assigned to represent the microstructure. An illustration of the grain boundary determination is presented in Fig. 3.6. The state of each cell depends on the state of the neighbouring cells by a transition rule.

In recrystallization problems, a cell will be recrystallized if any neighbouring cells were recrystallized before [77]. The state of the entire aggregate is updated simultaneously, unlike in Monte Carlo models, for which the update of each site occurs randomly. The so-called deterministic CA switches the state of a cell by replacing the neighbor cells depending on the rate equation, however, the probabilistic CA calculates the switching probability of each cell and makes the switching based a probabilistic step [111]. Switching parameters are generally used as a function of the previous state of a cell and the state of the neighboring cells.

CA is defined as a general algorithm with a possibility to use a wide variety of state variables and transition rules. Therefore, it is an attractive candidate for modeling recrystallization problems. Another advantage of the CA models is that they are computationally simple while modeling physical processes [111].

One of the major problems with the CA models is the correlation of simulation time with real time, similar to MC models. However, CA has been successfully used in the materials science problems such as recrystallization [112, 112, 113, 114, 115, 116, 117].

Since a simulated area in the CA is discretized, a finite element can be coupled to model a real microstructure. If the time-scaling is calibrated correctly, the finite elements can represent cells. This is one of the main advantages of coupling CPFEM and CA [112].
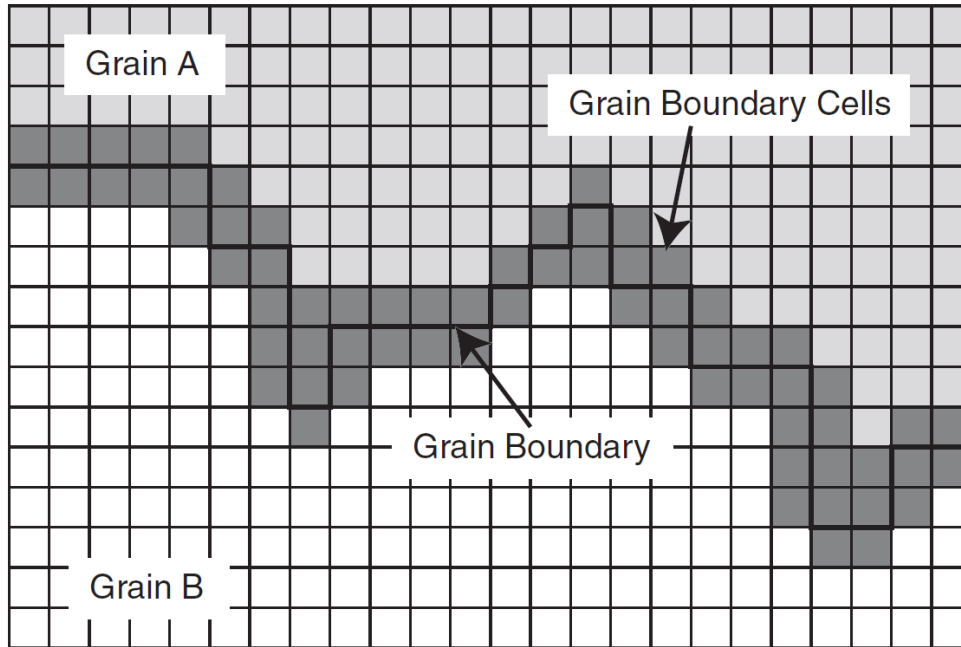
Figure 3.6: Schematic of grain boundaries in cellular automata [118]

Phenomenological and Crystal Plasticity models

The available models are not limited to the list above, and there are various other approaches to model DRX. The main drawback of most of them is that they are phenomenological, so the flow stress is represented by some empirical equations.

In the overview [68], *level set models* are mentioned for recrystallization problems. In this method, the boundary curvature is defined as an interface, which doesn't have to be tracked. However, the mesh used in the method should be fine enough, which causes computational inefficiency. Nevertheless, the level set method was coupled with crystal plasticity to model static recrystallization in [119]. Another use of this method was presented in [120] for modeling multiple junction movement.

Crystal plasticity models coupled with other methods can be used to simulate recrystallization problem. The ability of such models to account for texture development and local strain partitioning is the main advantage of using them. However, crystal plasticity models require significant computing power, which makes these models less available. In the literature, crystal plasticity finite element method (CPFEM) along with other models has been used to model static/dynamic recrystallization. [99, 121, 122, 123, 124, 112, 125]. Thus, CPFEM coupled with phase-field models to simulate recrystallization problem was pre-

27

sented by Takaki et al. [99, 121, 122], where the Kocks-Mecking (KM) equation was used to calculate dislocation density evolution giving the initial value to all the grid points. Furthermore, the macroscopic stress was related to the average dislocation density by Bailey-Hirsch equation. Potential nucleation sites were based on the critical value of the dislocation density and depending on the nucleation rate of the unit area per grain boundary, nuclei were placed randomly. In the works of Radhakrishnan et al. [123, 124], CPFEM was coupled with Monte-Carlo method. A new nucleation criterion based on the assumption that nucleation occurs potentially in the areas with high recovery rate was developed and implemented into a coupled mesoscale model to simulate the deformation and recrystallization in fcc and bcc bi-crystals and polycrystals.

Brown and Bammann [126] proposed a phenomenological plasticity model that is capable of simulating both static and dynamic recrystallization. No critical condition for nucleation was employed, rather, the volume fraction of recrystallized material was assumed to evolve according to the empirical equation. The model showed the ability to predict single and multiple peaks behaviour of the flow stress of the copper at different temperatures and strain rates. However, the microstructure evolution was not presented in this work.

Another approach to model DRX was presented by Xiao et al. [127]. In this work, CA was coupled with a topology deformation technique to take into account the effect of the grain topology change on microstructure evolution during DRX. The dislocation density was uniformly distributed in each grain, and the nucleation criterion based on the critical amount of dislocation density was implemented. The microstructure evolution was modeled depending on the plastic deformation of recrystallization grains with different initial crystallographic orientations. This model is not a finite element model, and no real microstructure was used for simulations.

The recent work of Li et al. [125] proposed a crystal plasticity model to simulate DRX in a two-phase titanium alloy. In this study, the grains were assumed to have a spherical shape and consisted of matrix (M-grain) and recrystallized grain (R-grain). Dislocation density was calculated depending on the volume average of M and R grains separately, and a nucleation criterion based on the critical value of the dislocation density was employed. Nucleation rate depended on the temperature and strain rate as well as the radius of the nuclei and M-grain to account for the effect of the nucleation site. Since the M and R grains were based on the volume fraction of the spheroidal grains, the model was not capable of modeling real microstructure evolution.

CPFEM coupled with cellular automata (CA) model with probabilistic switching rule was presented previously by Raabe and Becker [112] to simulate static recrystallization in aluminum alloys. In their work, CPFEM was used to deform the material, and the final

microstructure and accumulated shear strain were then used as input to the CA model for the recrystallization problem. Even though this model provided valuable insight to static recrystallization phenomenon, its application to simulate DRX is not straight forward since modeling DRX would require a synchronous coupling between CPFEM and CA.

3.3   Summary

An overview of the current state of literature has been introduced in this Chapter. Experiments on dynamic recrystallization, mainly on magnesium alloys are analyzed to form the basis of a numerical model. In particular, deformation twinning behaviour at elevated temperatures has been reviewed. Also, the main types of models to simulate recrystallization problems have been introduced with a brief description of each approach.

In order to model DRX, first, dislocation density has to be introduced. While the existing models use empirical equations to calculate the evolution of dislocation density, there are very few models that use a deterministic approach. The main challenge in the calculation of the dislocation density is accounting for grain interactions, because the dislocation density is related to the gradient of plastic deformation with distance, therefore, it requires the information from neighbours. Therefore, CPFEM has an advantage over the other grain-scale models, since it is based on the discretized sample and provides neighbouring elements' data. Moreover, crystal plasticity models can simulate microstructure evolution during deformation, which is another reason CPFEM is suitable to model DRX. Another important phenomenon that has to be captured during DRX simulations is the softening behaviour of stress-strain curve, for which the Kocks-Mecking equation is widely used in the literature. The Johnson-Mehl-Avrami-Kolmogorov empirical equation is used in the literature to simulate the evolution of DRX. Thus, most DRX models involve empirical equations.

The literature review of the existing models shows that models that can predict both microstructure evolution as well as softening behaviour of the flow stress during DRX without phenomenological expression, are rare. Most models use phenomenological expressions to calculate some components of DRX modeling. While phenomenological models can be used to investigate separate aspects of DRX, there is a need in a mechanism based DRX model for HCP metals in order to provide information on the DRX process and study the effects of various parameters (such as nucleation growth rate, critical conditions) on DRX evolution.

In the next chapter, the scope and objectives of the current work are presented.

Chapter 4

Scope and Objectives

Modelling the DRX phenomenon is a challenging problem mainly due to its multiscale nature, as it involves the effects of the impurities, precipitation, dislocation motion, movement of the grain boundaries etc. Moreover, DRX is widely accepted as a problem, which is not completely deterministic due to the concurrency of the grain boundary motion and the complexity of the solutions from dislocation based mechanics (such effects as interactions between boundaries during recrystallization can have more than one stable state solutions [128]). The main scope of this research is to investigate the effect of different microstructural features and deformation mechanisms on DRX evolution including softening in the flow curve and texture formation. Also the work aims to provide some insights into the material's behaviour during DRX. Thus, the main objectives of the current research are to:

1. Develop a mechanism-based predictive model that can capture microstructure evolution and stress-strain response during DRX in HCP materials using as input EBSD data and strain path. The model consists of the crystal plasticity finite element method and the DRX block. The DRX block, in turn, includes Cellular Automata with a nucleation criterion.

2. Incorporate deformation twinning into the model and investigate its effect on the final microstructure after DRX.

3. Validate the model (final texture, flow curve) with the available experimental data:

   - Slip based deformation (tensile test of AZ31 alloy).
   - Deformation including twins (compression test of the extruded Mg alloy).

4. Study the effect of the various parameters in the model on the results (threshold values for nucleation criteria, grain boundary mobility).

Detailed objectives:

1. The model is a hybrid model, which couples CPFEM with probabilistic cellular automata. The 2D crystal plasticity finite element code is developed for HCP metals. The CPFEM can account for experimental measurements like grain size, shape, texture as well as experimental flow stress measurements and critical resolved shear stress to accurately predict deformed state at each time step. The CPFEM is used to calculate state variables such as dislocation density, crystal orientation, velocity and then, it is then passed to the DRX block. A brief flow chart of the input/output of the model is presented in Fig.4.1.
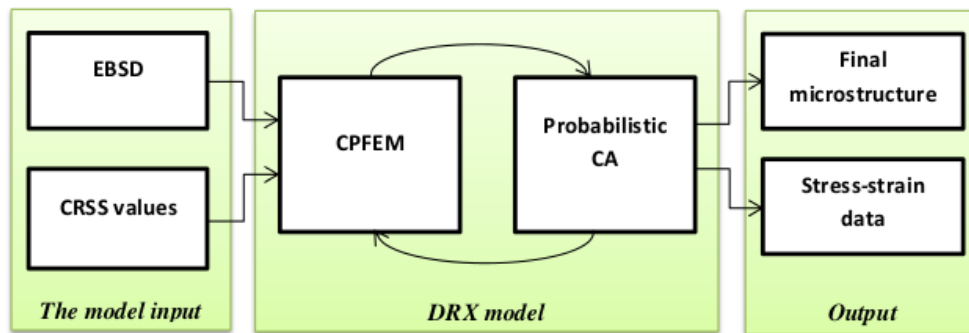
Figure 4.1: Flow chart of the coupling of CPFEM and CA

The DRX block consists of the probabilistic cellular automata (CA) model and the kinetics of DRX. The CA formulation uses the state variables to determine the location of nuclei and their growth. The state variables are dislocation density, orientation of the grain, and recrystallization state. The probabilistic switching rule is employed for the growth of the recrystallized grains, which is based on the velocity of the grain boundary.

DRX proceeds by way of the grains' nucleation and the subsequent growth of the nuclei. Therefore, one of the most important parts of modelling DRX is to determine nucleation of DRX. In this work, a new nucleation criterion has been developed based on the local mismatch in dislocation density. No assumption is made about the location of the successful nucleation sites, and it is calculated purely from the local grain orientations and the deformation states. This criterion can be implemented only

31

if the real microstructure is employed as input, since it is based on the inhomogeneous distribution of the dislocation density within a grain and across the grain boundary (which can be predicted by CPFEM). The nuclei form from the subgrains, which develop high angle grain boundaries during the deformation from the low angle grain boundaries. The nuclei have the same orientation as the matrix grain, and a new orientation is not generated during this process. Therefore, a random texture cannot be formed from a strong initial texture.

The proposed model couples CPFEM and CA to work synchronously, and a new method is presented to address the complicated problem of time and length scaling. A parameter Δt_{DRX} is introduced, the value of which can be calculated based on the finite element size. The finite elements coincide with CA cells; therefore, the cells are represented by elements, eliminating the need to map the data from one model to the other. The element size in the model is the same as EBSD step size, which usually varies from 2 to 5 microns. The effect of second phase particles, solid solutions and other precipitates is not taken into account in the model. The framework can be used to model dynamic recrystallization in any single-phase metals.

2. The model is extended to incorporate deformation twinning, which is one of the major deformation mechanisms in HCP metals. The effect of the twin orientations on the final texture after DRX is studied by reorienting an element to the dominant twin orientation before DRX starts. The reorientation procedure is similar to the PTR scheme offered by Tome et al. [27].

3. The model is validated using available experimental data. First, tensile test is simulated on Mg AZ31 alloy, which has a strong basal texture. The tensile load is applied in the rolling direction (RD), when the deformation is dominated by basal and prismatic slip systems. Then, a compression test is preformed on the extruded Mg alloy, when twinning is a favourable mechanism. The slip and twinning systems' activities are analyzed during the deformation at various temperatures. The final DRX texture and the softening behaviour is then validated.

4. The developed model involves a number of parameters that affect the results of the simulations, and their influence needs to be studied. Thus, the main parameters of the model are the critical conditions used for DRX initiation and grain nucleation. Also, the grain boundary mobility curve is varied between the step function and one-peak function due to the lack of the experimental data for Mg.

Chapter 5

Modeling Framework

In this chapter, the modeling framework is presented. First, the crystal plasticity constitutive model is briefly introduced, and then, the new DRX model is proposed.

5.1   Crystal Plasticity Constitutive Model

A new in-house finite element code based on the crystal plasticity theory is developed. The well-known framework of Asaro and Needleman [129] with the assumption of pseudo-slip to simulate twinning [12] is employed in this model. The formulations presented below can also can be found in [13], where the same framework was used to implement a Taylor-type model for HCP metals. However, in order to model the recrystallization problem, there is a need in the neighbouring of the grains, which can be attained using finite element mesh. The grid provides the possibility to calculate a dislocation density, which is an incompatibility of the deformation between the neighbouring elements. This is one of the major reasons why the crystal plasticity finite element method (CPFEM) is chosen.

The crystallographic slip and deformation twinning mechanisms considered in the model are presented in Table 2.1. A lattice undergoes plastic deformation by elastic deformation and rigid body rotation (Fig. 5.1).

The deformation gradient can be expressed as:

$$F = F^* F^p \tag{5.1}$$

where F^* includes elastic deformation and rigid body rotations, while F^p represents crystallographic slip and deformation twinning. Rotation of lattice vectors $s_{(\alpha)}$ and $m_{(\alpha)}$ can
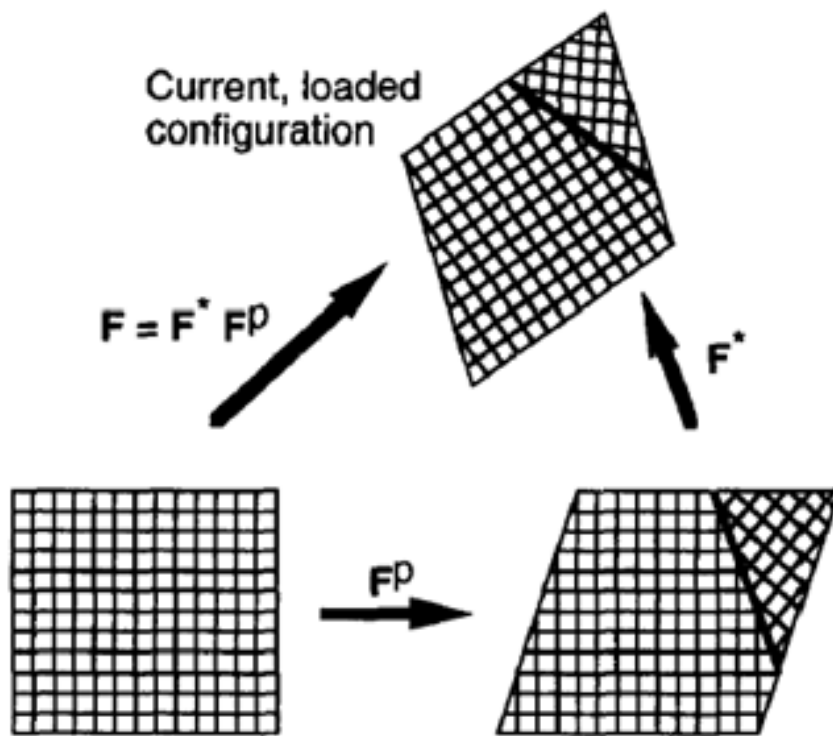
33

Figure 5.1: Schematic of deformation gradient decomposition

be specified by:

$$s^*_{(\alpha)} = F^* s_{(\alpha)}, m^*_{(\alpha)} = m_{(\alpha)} F^{*-1} \tag{5.2}$$

The velocity gradient is written as:

$$L = \dot{F}^* F^{*-1} + F^*(\dot{F}^p F^{p-1}) F^{*-1} \tag{5.3}$$

Symmetric and antisymmetric parts of the relations 5.3 give a strain rate, D, and so-called spin, Ω, which can also be divided into elastic and plastic parts:

$$D = D^* + D^p, \Omega = \Omega^* + \Omega^p \tag{5.4}$$

For computational simplifications, symmetric and skew-symmetric tensors for slip systems are calculated as follows:

$$P_{(\alpha)} = \frac{1}{2} \left[s^*_{(\alpha)} \otimes m^*_{(\alpha)} + m^*_{(\alpha)} \otimes s^*_{(\alpha)} \right] \tag{5.5}$$

$$W_{(\alpha)} = \frac{1}{2} \left[s^*_{(\alpha)} \otimes m^*_{(\alpha)} - m^*_{(\alpha)} \otimes s^*_{(\alpha)} \right] \tag{5.6}$$

where α denotes the slip system. Hence, the plastic strain rate and spin can be presented respectively as:

$$D^p = \left(1 - \sum_{\beta=1}^{N^{tw}} f_{(\beta)} \right) \left[\sum_{\alpha=1}^{N^s} P_{(\alpha)} \dot{\gamma}_{(\alpha)} + \sum_{\beta=1}^{N^{tw}} P_{(\beta)} \dot{f}_{(\beta)} \gamma^{tw} \right] + \sum_{\beta=1}^{N^s} \left[f_\beta \sum_{\alpha=1}^{N^s} (P^{tw\beta}_{(\alpha)} \dot{\gamma}^{tw\beta}_{(\alpha)}) \right] \tag{5.7}$$

and

$$\Omega^p = \left(1 - \sum_{\beta=1}^{N^{tw}} f_{(\beta)} \right) \left[\sum_{\alpha=1}^{N^s} W_{(\alpha)} \dot{\gamma}_{(\alpha)} + \sum_{\beta=1}^{N^{tw}} W_{(\beta)} \dot{f}_{(\beta)} \gamma^{tw} \right] + \sum_{\beta=1}^{N^s} \left[f_\beta \sum_{\alpha=1}^{N^s} (W^{tw\beta}_{(\alpha)} \dot{\gamma}^{tw\beta}_{(\alpha)}) \right] \tag{5.8}$$

where f_β is the volume fraction of twinning system β and $\dot{f}_{(\beta)}$ is its rate, γ^{tw} is shear strain on twinning systems and $\dot{\gamma}_{(\alpha)}$ represents shear rate on the slip system α. N^s and N^{tw} correspond to number of slip systems and number of twin systems respectively.

35

The shear rate and rate of twinning are given by the following power-law equations:

$$\dot{\gamma}_{(\alpha)} = \dot{\gamma}_{(0)} sgn\tau_{(\alpha)} \left| \frac{\tau_{(\alpha)}}{g_{(\alpha)}} \right|^{1/m} \tag{5.9}$$

$$\dot{f}_{(\beta)} = \frac{\dot{f}_{(0)}}{\gamma^{tw}} sgn\tau_{(\beta)} \left| \frac{\tau_{(\beta)}}{g_{(\beta)}} \right|^{1/m} \tag{5.10}$$

where $\tau_{(\alpha)}$ is the resolved shear stress on the slip system α, and is calculated as $\tau_{(\alpha)} = P_{(\alpha)} : \sigma$, $g_{(\alpha)}$ is the hardness of the slip system, where the evolution can be calculated by the hardening law:

$$\dot{g}_{(\alpha)} = \sum_{\beta} h_{(\alpha\beta)} \left| \dot{\gamma}_{(\beta)} \right| \tag{5.11}$$

where $h_{(\alpha\beta)}$ is the hardening moduli:

$$h_{(\alpha\beta)} = q_{(\alpha\beta)} h_{(\beta)} (\text{no sum on} \beta) \tag{5.12}$$

where $h_{(\beta)}$ is a hardening rate of the slip system and $h_{(\alpha\beta)}$ is the latent hardening matrix. The hardening rate is given as follows:

$$h_{(\alpha)} = h_{(0)} \left[\frac{h_{(0)}\gamma_a}{\tau_{(\alpha)}n} + 1 \right]^{n-1} + h_1 \tag{5.13}$$

where $h_{(0)}$ is the initial hardening rate of the slip system, n is the hardening exponent and γ_a is the accumulated shear on all the slip systems:

$$\gamma_a = \int_0^t \sum_{\alpha=1}^{N^s} |\dot{\gamma}_{(\alpha)}| \mathrm{d}t \tag{5.14}$$

Finally, the Cauchy stress is calculated as a sum of stresses in the matrix and in the twinned region:

$$\sigma = \left(1 - \sum_{\beta=1}^{N^{tw}} f_{(\beta)} \right) \sigma^{mt} + \sum_{\beta=1}^{N^{tw}} f_{(\beta)} \sigma^{tw\beta} \tag{5.15}$$

The deformation twinning affects the deformation gradient by the rotation of the lattice. An initial transformation matrix was proposed by Van Houtte [36], considering m as a

twin plane normal:

$$Q_{ij} = 2m_i m_j - \delta_{ij} \tag{5.16}$$

Hence, the elastic moduli for the twinned region can be recalculated as:

$$E_{ijkl}^{tw} = E_{mnop}^{mt} Q_{im} Q_{jn} Q_{ko} Q_{lp} \tag{5.17}$$

The DRX framework and its coupling with the CPFEM is described in the next section.

5.2 New Dynamic Recrystallization Model: Probabilistic Cellular Automata

A new approach is presented in this research to model dynamic recrystallization in HCP metals. The model is coupled with crystal plasticity finite element method described in the previous section. The proposed approach can be divided into three main parts:

- Modelling and prediction of nucleation.

- Grain growth and its kinematics during DRX.

- Local behaviour (flow stress) of recrystallized grains.

5.2.1 Modelling of a grain nucleation

The concept of *recrystallization nuclei* as initiators of growth based on the dislocation density was introduced in the work of Cahn [130]. The major assumption was to identify subregions with high dislocation density mismatch with surroundings.

There are two main critical conditions used in literature, a criterion based on the critical value of the dislocation content [131], and a geometrical criterion, which constitutes the initiation of DRX once pre-existing subgrain reaches the critical size [132, 133] (Fig. 5.2). Experimental observations show that subgrains grow by sweeping away dislocations and leaving a relatively clean grain [7]. In order to satisfy to the mechanical instability, regions with lower dislocation content surrounded by neighbours with higher dislocation density are chosen as potential nuclei.

In this research, the initiation of DRX is assumed to occur with subgrain formation at grain boundaries. Two critical conditions are introduced in the model to identify potential
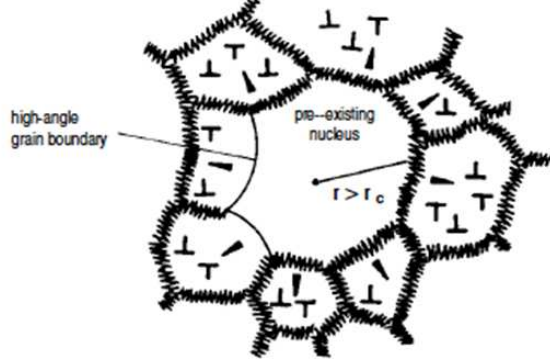
Figure 5.2: Schematic representation of the nucleus [134]

nucleation sites. Subgrains that share high angle boundary with neighbouring grains can become potential nucleation sites if (i) their dislocation density reaches a certain threshold value (the model parameter that will be defined later), (ii) the difference in the dislocation density between those two grains is greater than the defined critical value (the model parameter that will be defined later). However, before introducing any nucleation criteria, the dislocation density has to be calculated.

Dislocations can be divided into two categories, geometrically-necessary dislocations (GNDs), which occur due to geometrical constraints of the crystal lattice, and statistically-stored dislocations (SSDs), which accumulated during plastic deformation by trapping to one another [135].

As it was mentioned in previous chapters, the CPFEM allows to calculate dislocation density, which is related to the gradient of plastic deformation. It should be noted that only GNDs are considered here. The relation was first introduced by Nye [136] and is called Nye tensor:

$$\alpha = -(\nabla \times \mathbf{G}) \tag{5.18}$$

where $\mathbf{G}$ is "the lattice correspondence tensor" [137]. The formulation of Nye tensor was taken forward to a new definition by Arsenlis and Parks [138]. In the new definition, dislocation density is calculated based on the local crystal frame for each slip system α using its descriptive vectors $\mathbf{s}_{(\alpha)}$ (slip plane normal) and $\mathbf{m}_{(\alpha)}$ (slip direction) and shear strain γ on each slip system as follows:

$$\rho_{GN(e)}^\alpha b = -\nabla\gamma^\alpha \cdot \mathbf{m}^\alpha = -\gamma_{,\mathbf{k}}^\alpha \mathbf{s}_{\mathbf{k}}^\alpha \tag{5.19}$$

$$\rho_{GN(s)}^\alpha b = \nabla\gamma^\alpha \cdot \mathbf{n}^\alpha = \gamma_{,\mathbf{k}}^\alpha \mathbf{n}_{\mathbf{k}}^\alpha \tag{5.20}$$

where (e) and (s) are for edge and screw parts of dislocation density respectively, and

$\mathbf{n}^\alpha = \mathbf{s}^\alpha \times \mathbf{m}^\alpha$. Equations 5.19 and 5.20 are re-derived from the Nye's tensor, projecting the total deformation gradient as defined earlier on the particular slip plane and direction. This formulation gives more representative information about the contribution of particular slip plane to the dislocation density.

The total GND density tensor can be consequently obtained from:

$$\rho_{GN}^\alpha = \sqrt{(\rho_{GN(s)}^\alpha)^2 + (\rho_{GN(e)}^\alpha)^2} \tag{5.21}$$

Since statistically stored dislocations density (SSD) cannot be accurately measured by existing experimental techniques (EBDS, SEM, TEM) [139], it is not considered in the current model. However, the possible effect of SSDs on the DRX phenomenon can not be excluded and dislocation density based crystal plasticity models are available in literature to account for both GND and SSD [32]. Finally, it should be mentioned that the *dislocation density* represents another *state variable* for the CA model.

Critical condition for DRX initiation

The onset of DRX is known to occur right before the peak stress is achieved in the stress-strain curve [140]. In order to eliminate the subgrains from nucleating at the very early stages of deformation, a critical threshold value for the dislocation density is introduced (Fig. 5.3).

The critical condition for subgrain bulging was first introduced by Roberts and Ahlblom [132]. Then, it was adopted as a nucleation criterion in many recrystallization studies [99]. In this work, it is used as an initiation criterion, so that DRX can start only when the dislocation density reaches the critical value:

$$\rho_{cr} = \left(\frac{20S\dot{\epsilon}}{3bLM\tau^2} \right)^{1/3} \tag{5.22}$$

where S is the grain boundary energy per unit area, M is the grain boundary mobility, τ $(c\mu b^2)$ is the dislocation line energy and L is the dislocation mean free path, which is defined as $L = K/c_2\sqrt{\rho}$, the constants K, c are of the order 10 and 0.5 respectively.

The parameters K and c in 5.22 can be determined by curve-fitting to the experimental stress-strain curve. For simplicity, the constants (K, c, c_2) are combined into one constant value, and the effect of this parameter on the simulations will be studied in Chapter 7. It can be seen in Fig. 5.4, depending on temperature and strain rate, the behaviour of the flow
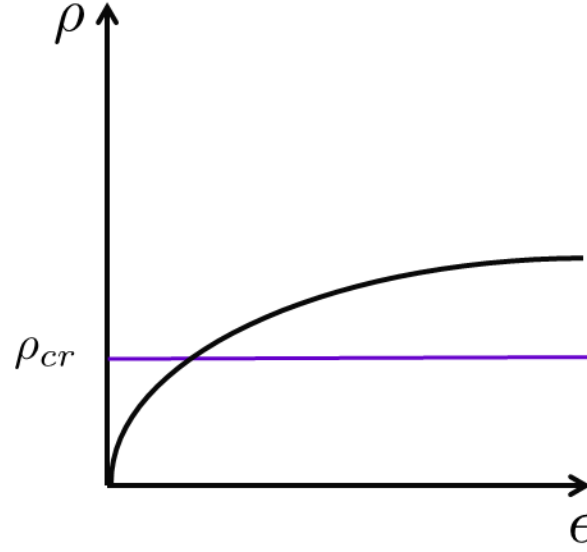
Figure 5.3: Schematic representation of the ρ_{cr}.

stress is different, and the onset of DRX occur at different strains. Therefore, the critical value has to be calibrated based on a simulated temperature. A schematic example of the fitting procedure is presented in Fig.5.5, which shows that the best match is obtained from the simulation number 2 (crit2) (the values are not presented since the figure is used for illustration purposes).

After determining the initiation of DRX, the nucleation criterion has to be introduced (which subgrains will grow). The next subsection presents a new nucleation criterion used in the present work.

Determining nuclei

In the current model, the potential nucleation sites are the subgrains with high angle grain boundaries formed during deformation. Disorientation angle is calculated between the current element and its neighbours according to the well-known formula:

$$\theta = min \left[cos^{-1} \left(\frac{tr(T_i T_j^T) - 1}{2} \right) \right] \tag{5.23}$$

40

Figure 5.4: Schematic of single and multiple peaks of stress-strain curve

Figure 5.5: An example of calibration of ρ_{cr} value.
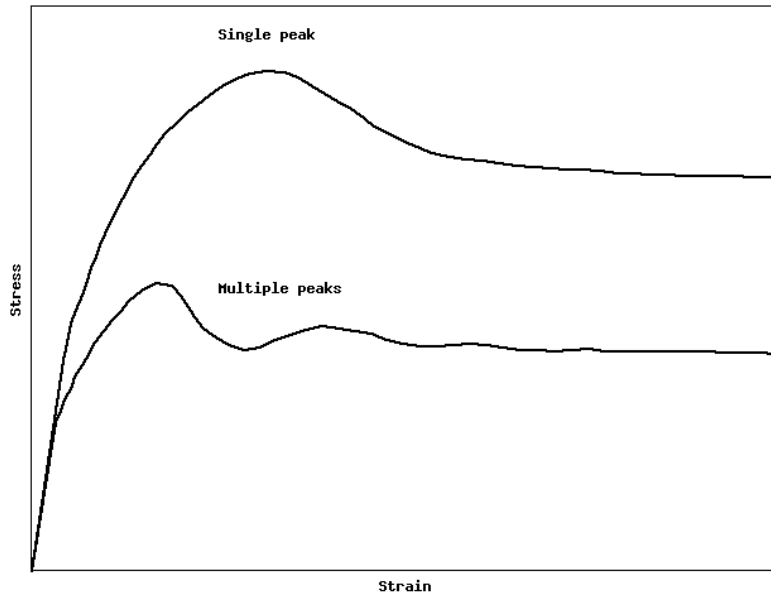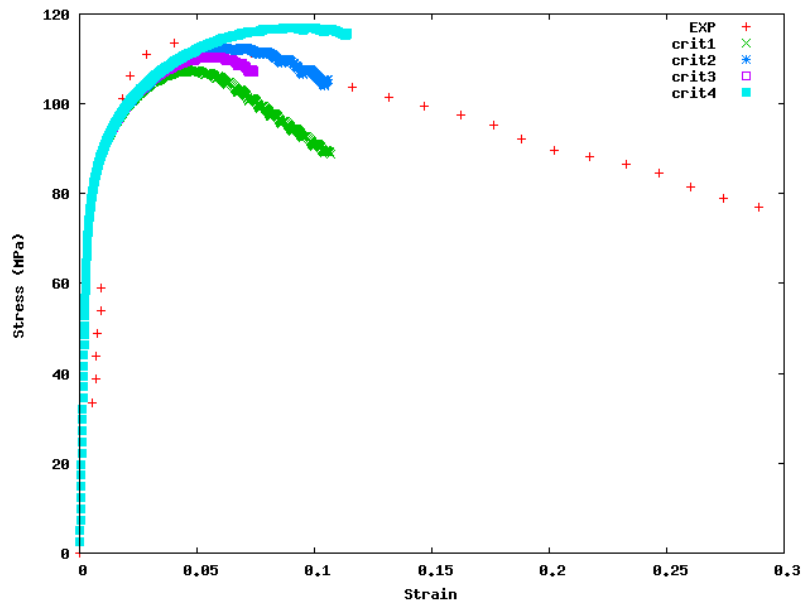
where T_i and T_j are the rotation matrices of the current element and the neighbour element. They determine the orientation of the element. Disorientation angle is the minimum misorientation angle among all possible angles that is obtained by applying the symmetry operators. The *orientation matrix T* will be employed as one of the *state variables* in the new model. The boundaries with high disorientation angle are the potential nuclei, and a critical angle, θ_{cr}, is taken to be 15∘ that represents high angle grain boundaries.

Experimental observations show that subgrains grow sweeping away dislocations and leaving relatively clean grains [7]. In order to satisfy to the mechanical instability, grains with lower dislocation content surrounded by neighbours with higher dislocation density will be chosen as nuclei. The criterion is presented in [141], based on the difference ("jump") in the dislocation density (DDT) between the neighbouring elements i and j:

$$d\rho_{ij} = \rho_i - \rho_j \tag{5.24}$$

where ρ_i, ρ_j are the total dislocation densities of the elements i and j respectively. The subscript GN is dropped from the formulation for simplicity.

A critical value for the dislocation density mismatch is chosen to be proportional to the maximum value of the dislocation density that occurs at this time step over the sample, ρ_{max}:

$$d\rho_{cr} = C_0 \rho_{max} \tag{5.25}$$

This critical value controls a number of the new nuclei that occur throughout the deformation, therefore, in order to control the rate of nuclei, the evolving value is used, ρ_{max}, which is representative at each time step. If a constant value was used, the nucleation rate would be growing with deformation. The average value of the dislocation density is not used since it decreases with the evolution of DRX (see schematic in Fig. 5.6). Therefore, the maximum value of dislocation density is used in a threshold value for nucleation criterion. The constant, C_0, ranges between 0.1 and 0.9, and it has to be calibrated for each simulation conditions (temperature and strain rate). The effects of this parameter are studied in Chapter 7.

Thus, in order for the subgrain to become a potential nucleation site, the following conditions have to be satisfied:

- a subgrain has to be have a high angle grain boundary $\theta \geq \theta_{cr}$;

- a dislocation content of the element has to reach a critical value $\rho \geq \rho_{cr}$ (eqn.5.22);

- a dislocation density "jump" has to be more than a critical value $d\rho_{ij} \geq d\rho_{cr}$.

42
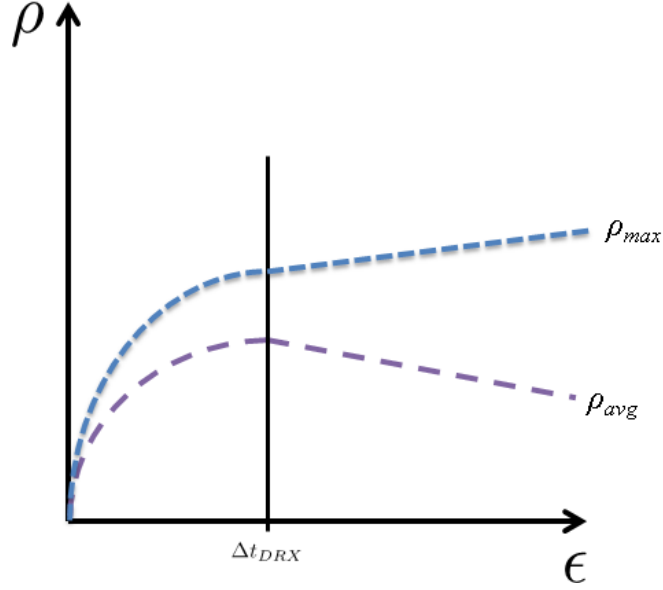
Figure 5.6: Schematic of evolution of ρ_{max} and ρ_{avg}.

A threshold values employed in the model are the parameters of the model and their effect on the nuclei and DRX evolution is investigated in Chapter 7.

5.2.2 Grain growth and its kinematics during DRX. Probabilistic Cellular Automata.

After potential nucleation sites are identified, the kinematics of the nuclei growth needs to be introduced. Driving force for the grain boundary migration is provided by the stored energy, which is proportional to the velocity of the grain boundary. A grain boundary velocity depends on the mobility of the grain boundary, M, and the difference in stored energy, ΔP as follows [134]:

$$v = M\Delta P \tag{5.26}$$

The stored deformation energy consists of the dislocations stored after cold working in metals, and it can be calculated as [134]:

$$P = \frac{1}{2}\rho\mu b^2 \tag{5.27}$$

where μ is the shear modulus. The driving force for boundary migration has the dimension of energy per unit volume, which is equivalent to pressure. Taken $\rho \sim 10^{15}$ m^{-2}, $\mu \sim 10^{11}$ J/m^3, $b^2 \sim 10^{-19}$ m^2, then P $\sim 10^7$ J/m^3 = 10 MPa [134].

The mobility, M, represents the ability of the grain boundary to migrate, and in order to satisfy to the kinematic instability, boundaries should have high mobility. Even though mobility of the grain boundary can be obtained from experiments for certain materials and boundaries, an empirical expression was introduced in [134]:

$$M = M_0 \text{exp}\left(-\frac{H_m}{kT}\right) \tag{5.28}$$

where H_m is the activation enthalpy and M_0 is the pre-exponential factor. A generalized shape for the mobility curve that was introduced in the manuscript by Humphreys and Hatherly [7] is presented in Fig. 5.7. The solid lines represent the regions where some experimental data is available, while the dotted lines are the assumptions. It is accepted in the literature that higher misorientation angle boundaries have higher mobility (region B), while lower angle boundaries have lower mobility (regions A, C2, C1). The saturation angle is about 20 degrees. However, there are special boundaries that are more mobile than the others, for example, $\Sigma 7$ boundaries [134].

The experimental data of the mobility curve for magnesium is not available in literature. However, since the generalized shape is known, a step function is used in the current simulations for simplicity. The low angle grain boundaries are set to have lower mobility than high angle grain boundaries. The parametric study of the mobility function is presented in the Chapter 7.

In order to model DRX using CA, the sample is divided into the cells with state variables [142]. The cells in the current model correspond to the finite elements, therefore, no mapping procedure is needed. Note that cell and element are used interchangeably in the remainder of this work. State variables used in the cellular automata model are as follows:

- crystal orientation, T, which is assigned to each element as input and it evolves during deformation;

- dislocation density, ρ, calculated from the crystal plasticity part of the model as described above;

- the variables, N and R, which can take the values 0 or 1 depending on whether the element is a nucleus or a prior recrystallized element respectively.
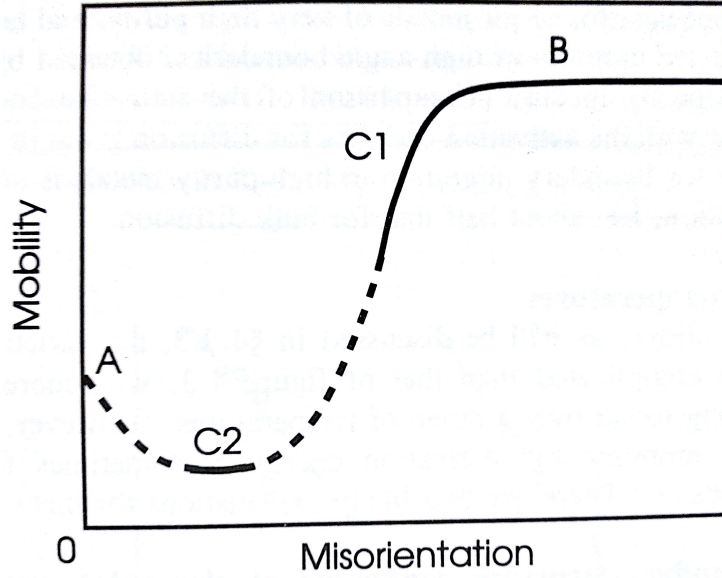
44

Figure 5.7: Schematic diagram of possible distribution of mobility function depending on misorientation angle [7].

The time and length scale are known to be one of the main challenges in the CA models [68]. In the present model, the parameter Δt_{DRX} is implemented in order to define the correlation between simulation time and DRX time step:

$$\Delta t_{DRX} = C_T \times \frac{(cellsize)_{avg}}{v_{avg}^{gb}} \tag{5.29}$$

where v_{avg}^{gb} is an average grain boundary velocity, and $cellsize$ is the element size used in the model, C_T is a constant, which is calibrated through a nucleation process.

A DRX step occurs once the velocity of the grain boundary is high enough to surpass the size of the element (Δt_{DRX} depends on the element size). Thus, Δt_{DRX} should have a lower value for a finer mesh (smaller element size) compared to that of a coarser mesh (larger element size). For instance, if the CPFEM total time step is 1000, the Δt_{DRX} will have a magnitude of 100, which raises the question of inhomogeneous distribution of the grain boundaries' velocity. There is a possibility that some boundaries with higher mobility, hence, the velocity, can travel more distance than the element size during DRX time step, since an average velocity is used in its calculation. However, this problem is taken care of by the probabilistic step that does not allow the boundaries with lower velocities to go

45

through recrystallization, so that the overall response will be representative (while some of the local behaviours might not be). Thus, the model cannot predict the outliers correctly, but statistically it will still be representative.

At the beginning of the deformation the recrystallization variables are set to zero, $N = 0$ and $R = 0$. The simulation proceeds in the CPFEM part of the model, until the DRX step is taken. Then, the state variables are passed to the DRX block, where, as a first step, the potential nucleation sites are found using the criteria described above.

Once the potential nucleation sites are determined, the probabilistic step is taken, where viable nuclei are chosen with certain probability. Depending on the state of the neighbouring cell, the probability switching rule is defined as:

$$\omega_{switch} = \frac{v_i^j}{v_{max}} \tag{5.30}$$

where v_{max} is the maximum velocity over the complete structure and v_i^j is the velocity of the current element i with respect to its neighbour j.

According to the probabilistic CA, a random number $\xi \in [0, 1]$ is generated, and if $\xi \leq \omega_{switch}$ then the current element is a feasible nucleus, and the switching variable for nucleation N takes a value of 1 (otherwise $N = 0$) if this is a nucleation step. For the growth step, if $\xi \leq \omega_{switch}$ then the current element, i, is recrystallized by the neighbouring element, j, if only the element j is a nucleus ($N = 1$) or it was recrystallized before ($R = 1$). When the element i is successfully recrystallized, it takes a state (orientation) of the element j, $T_i = T_j$, and a state variable R, which shows whether the element was recrystallized or not, takes a value of 1 (otherwise $R = 0$).

$$\xi = rand(0,1) \begin{cases} N/R = 1, \ \rho = 10^{-1}, \ \sigma = a\mu b^2 \sqrt{\rho} & \text{if } \omega_{switch} \geq \xi \\ N/R = 0 & \text{if } \omega_{switch} < \xi \end{cases} \tag{5.31}$$

Since the components of the stress tensor in the element are set to a lower value (the dislocation density in the recrystallized element is lower), it will decrease the total stress over the aggregate. Thus, the softening behaviour of the flow curve is captured only by the evolution of the DRX without an empirical equation. However, it should be noted that computational instabilities occur if the stress in the element is set to a low value at once. Therefore, during the simulation the stress in the recrystallized element is decreased gradually over a few time steps to avoid this computational instability.

In order to avoid situations when two or more elements can potentially consume the same element, probabilistic step is taken based on the velocity of each nuclei.

In the proposed model, two different neighbouring schemes are considered: 4-point and 8-point, which are known in CA models as von Neumann and Moore neighbours respectively as shown in Fig. 5.8 [111]. The closest four or eight elements (with corner elements) are taken into account for the state switching rule. However, in the present simulations, the modified von Neumann neighbourhood is used, because it gives potentially more freedom for the grain to grow. The neighborhood used is like the octagonal neighborhood as corner elements are harder to recrystalize with proportionality of 0.48. If it is assumed that the boundary has a spherical curvature (or elliptical), with the fixed radii, the hexagon (or in this case an octagon) inside this sphere with a fixed radii will cover more surface than a square, which is energetically more favorable. Moreover, the overall root mean square distance mismatch for hexagonal packing will be smaller than for square. The example of using four and eight point schemes is shown in Fig. 5.9, where 4-point scheme consists of the diamond pattern grains, while the 8-point scheme revealed more realistic grain shape.

Thus, for the corner elements, however, the switching parameter for the probabilistic step is taken to be:

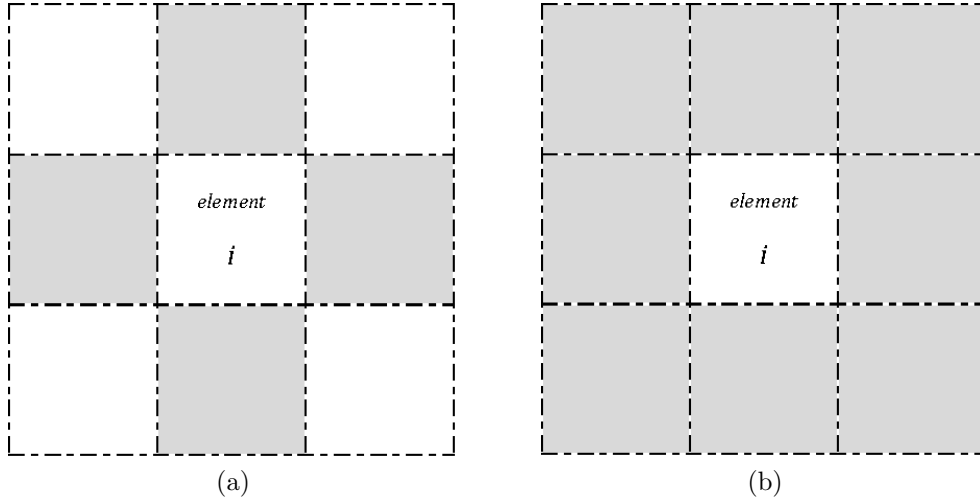$$\omega_{switch} = 0.48 \frac{v_i^j}{v_{max}}$$

Figure 5.8: Defining the element and its neighbours (a) 4-point scheme (b) 8-point scheme
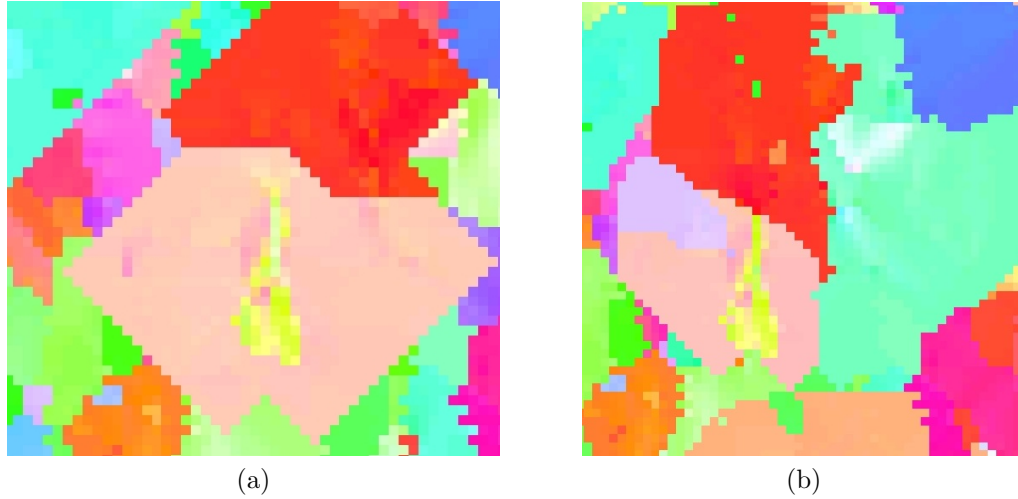
Figure 5.9: The shape of the grains after simulation using (a) 4-point and (b) 8-point schemes

5.2.3 Local behaviour of recrystallized grains

During dynamic recrystallization, grain boundaries move leaving behind a strain free grain, and as a consequence, dislocation density over the sample becomes lower. Hence, DRX is known to soften material response once nucleation happens. The effect of this phenomenon on the flow stress behaviour was discussed in [140], where DRX flow stress is studied on the influence of grain structure. An example of the behaviour of the stresses during DRX is demonstrated in Fig.5.10. With decreasing Zener-Hollomon parameter, Z, (lower strain rate and higher temperature) the peak stress shifts down.

In the current model, the dislocation density of a recrystallized element is set to be low ($\rho_{rx} = 10^{-1} * \rho$) and the flow stress of this element is recalculated as:

$$\sigma = a\mu b^2 \sqrt{\rho} \qquad (5.32)$$

where μ is shear modulus, b is the Burgers vector and ρ is the dislocation density.

The local softening of the recrystallized element results in the softening of the stress of the aggregate as the fraction of recrystallized elements increases. However, one of the goals of the model is also to predict that behaviour without any phenomenological expressions.
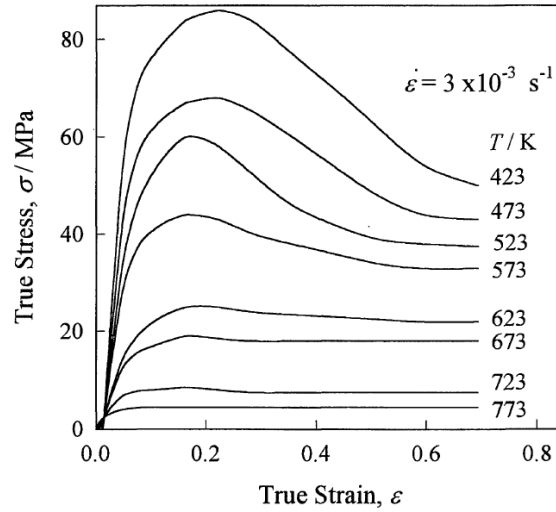
Figure 5.10: True stress vs. true strain curves deformed at different temperatures for pure magnesium tensile test [55]

5.3   Summary

In this Chapter, the modeling framework is presented (a graphical representation is given in Fig. 5.11). The model consists of two blocks: the CPFEM part and the Probabilistic CA. The CPFEM employs microstructural information (EBSD data) as input, and the calibrated parameters (CRSS values) are given. It should be noted that the CRSS values are calibrated with the experimental stress-strain curve. Then, in the CPFEM part, the dislocation density, ρ, is calculated, and crystal orientations, T, and stress state, σ, are passed to the DRX part of the model, where probabilistic CA is employed. Then, the updated crystal orientations and stresses are sent back to the CPFEM. The nucleation criteria are also included in the DRX part of the model. The numerical model predicts the final microstructure and the stress-strain curve.
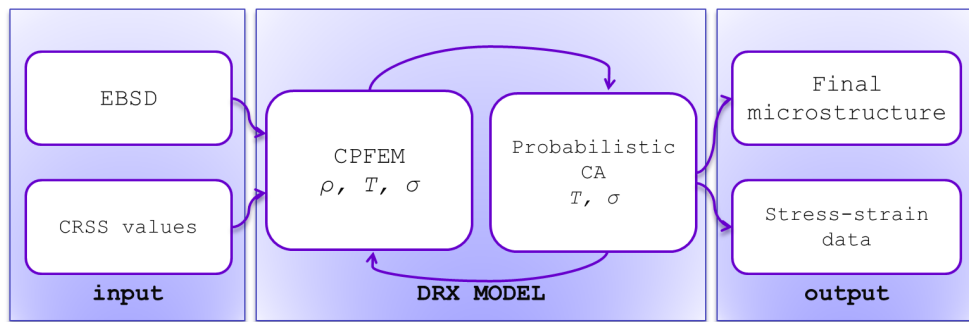
Figure 5.11: Flow chart of the coupling of CPFEM and CA

Chapter 6

Results and Discussions

6.1 Dynamic recrystallization without twinning: Tensile test of Mg AZ31 alloy

6.1.1 Experimental data

The electron backscatter diffraction (EBSD) scan for the simulations are obtained using LEO 1450 scanning electron microscope (SEM) fitted with a TSL EBSD camera. The scan area size is $2000 \times 2000 \mu m$ taken from the surface of AZ31 Mg alloy sheet. The average grain size of the sample is $14\mu m$. A cropped area of dimensions $800 \times 300 \mu m$ is assumed to be a representative scan size provided by the work of Brahme et al. [143], and it is selected from the full data set using TSL software.

The EBSD data was analyzed using the TSL$^{\text{TM}}$OIM software (Version 4.6). The data was cleaned to remove bad data points and only data points having a confidence index (CI) above 0.2 were retained for the analysis. Cleanup was performed using the TSL **Grain Dilation** feature by setting the *grain tolerance angle* to $5°$ and the *minimum grain size* to 10 data pixels. Also TSL **Neighbour CI Correlation** with *minimum confidence index* set to 0.2 was employed to remove bad data points. Grains were identified with a misorientation tolerance of $10°$, using the TSL **Single Orientation per Grain** set to $10°$. That is all the pixels having a misorientation of less than $10°$ were grouped together and identified as a grain. For the analysis, grains with less than 10 data points were excluded. Once grains were identified all the pixels in the grain were assigned an average orientation of the grain. As a result, the misorientation of any two pixels within a grain is zero.

6.1.2 Initial material and finite element discretization

The EBSD map is discretized with quadrilateral elements consisting of four constant strain triangular sub-elements, which contain a higher order integration scheme. The full details about the advantages of using these elements can be found in the work of Inal et al. [144].

The initial EBSD map and pole figures from AZ31 magnesium alloy sheet are given in Fig. 6.1. An area of $800\mu m \times 300\mu m$ is used as a representative scan size (RSS) [143]. The pole figures show a strong basal texture typical for this alloy. The EBSD pattern is mapped into the finite element mesh with 14972 quadrilateral elements (corresponding to 1300 grains). The element size corresponds to the EBSD step size of $3\mu m$. The grain colors represent their crystallographic orientation.

6.1.3 The simulation results

In order to validate the capability of the DRX model, tensile test data has been used in this study. During tension tests along the RD or TD, the grains of AZ31 sheets are not oriented for $\{10\bar{1}2\}$ extension twinning (c-axis is perpendicular to tensile axis). However, some contraction twins could appear acting as potential nucleation sites, but as reported in the experimental study of Al-Samman et al. [56], contraction twins do not influence texture during tensile test in any significant manner.

Experimental data for tension tests of AZ31 sheets at different temperature and strain rates as reported in [56, 9, 63] in the literature are used for this analysis.

The generated mesh was subjected to uniaxial tension along the RD. Parameters of the CPFEM part of the model are calibrated in order to fit the first peak of the flow stress, which is shown in Fig. 6.2. The behaviour of CRSS values for different slip systems in magnesium alloys were studied in [64, 145]. It was reported that CRSS for prismatic and pyramidal $\langle c + a \rangle$ slip systems decreases with increasing temperature. Thus, the ratio of the CRSS values for basal, prismatic, pyramidal $\langle a \rangle$ and pyramidal $\langle c + a \rangle$ is chosen to be 1:2:2.5:3 in the current simulation. Various parameters used in the model are presented in Table 6.1.

The threshold value for misorientation, θ_{cr}, is taken to be 15° degrees, which represents high angle grain boundaries. The critical value for the dislocation density mismatch, $d\rho_{cr}$, evolves during the deformation and is calculated based on the current maximum value, ρ_{max}, which occurs over the domain at the current simulation time step, as follows:

$$d\rho_{cr} = C_0\rho_{max} \tag{6.1}$$
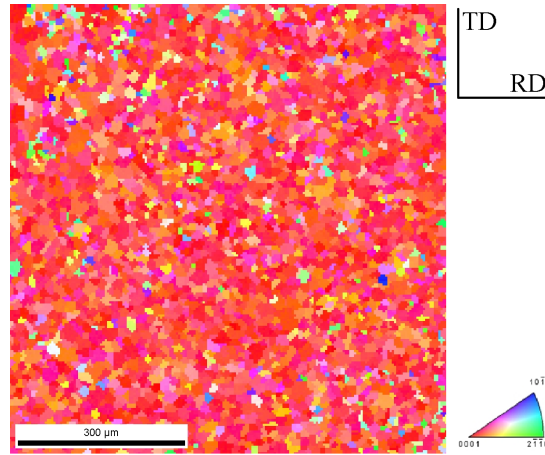
(a)
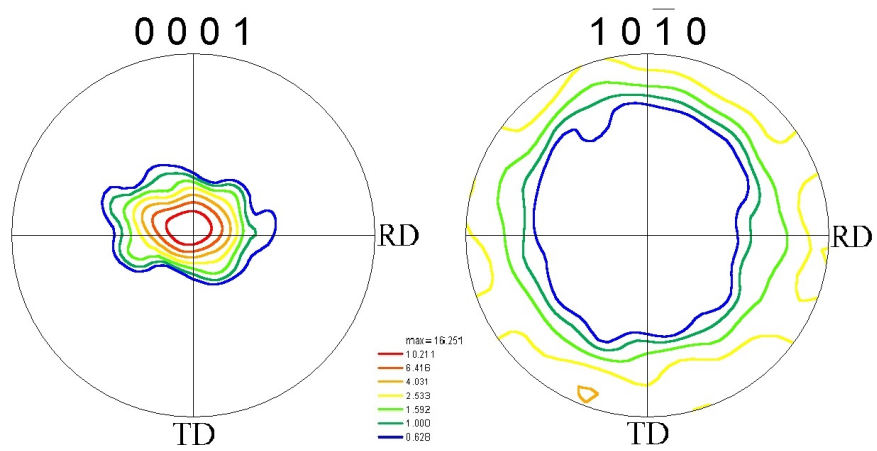
(b)

Figure 6.1: Initial EBSD IPF map and {0001} and {10$\bar{1}$0} pole figures of AZ31 Mg alloy sheet with strong basal texture

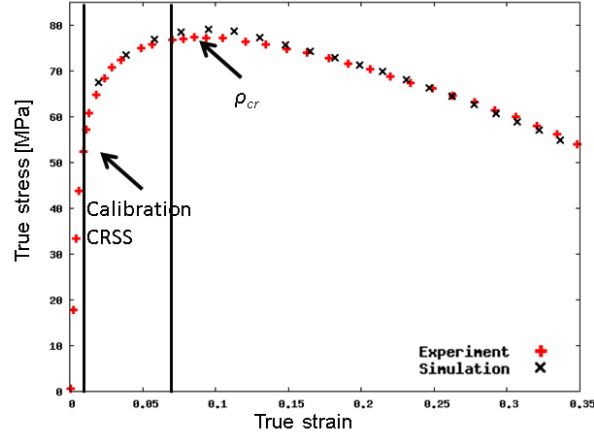C_0 is taken to be 0.5 in the current simulation.

Figure 6.2: Experimental flow curve [64] and simulation flow curve to show the point of the calibration of the CPFEM parameters.

Table 6.1: Various parameters used in the current tensile simulation

Parameter (Eqn.number)	Value used in the simulation
$\dot{\gamma}_{(0)}$ (eqn.5.9)	0.001
γ^{tw} (eqn.5.10)	0.06
$\dot{f}_{(0)}$ (eqn.5.10)	0.5
m (eqns.5.9,5.10,)	0.12
$h_{(0)}$ (eqn.5.13)	8.1
n (eqn.5.13)	0.13
K, c_2 (used for L)	10, 0.01

Comparison between experimental and predicted true stress vs. true strain curves are presented in Fig. 6.3. The experimental curve is taken from the work of Li et al. [64]. It can be seen that simulated results are in excellent agreement with the experimental results. Initiation of the DRX as well as continuous softening are both reproduced in the model.

In Fig. 6.4 a few viable nuclei and their growth are magnified in order to show the evolution of grain growth. Three or more different nuclei (elements) are seen growing in specific directions depending on the dislocation density. As seen from the IPF map (Fig. 6.4), these grains have high misorientation. The magnified area demonstrates the locations of a few nuclei (blue, magenta and red, for instance), which appear in a couple of the DRX
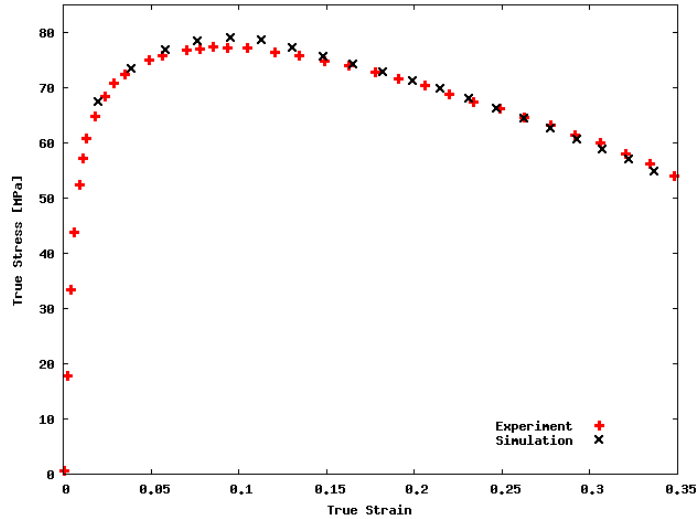
Figure 6.3: Predicted and experimental true stress vs.true strain curve during tension test along RD at $300°C$ and strain rate $5 \times 10^{-4}s^{-1}$.

steps. Further cycles of DRX were observed in FCC metals such as aluminum, copper [8]. It is known to cause the second peak in the stress-strain curve and grain refinement. However, in the stress-strain curve obtained for the magnesium alloy used in this study, only one peak stress is observed followed by continuous softening. Thus, the effect of the second or further cycles of recrystallization is not clear, therefore, in the current model, it is assumed that an element can be recrystallized only once. Furthermore, a viable nuclei cannot be consumed by other recrystallized grains (elements). Once the growing grains impinge, further growth is suppressed. In case if one element has two or more recrystallized neighbours and both can grow into that element, such competing situations are solved by the probabilistic step.

To further investigate the effects of DRX on the material response, uniaxial tension simulation for the magnesium alloy AZ31 is performed with the same material properties, but without DRX. The microstructure obtained from DRX and non-DRX simulations along with initial microstructure are presented in the Fig. 6.5. The deformed EBSD IPF map without DRX, (Fig. 6.5b) demonstrates a slight change in the microstructure compared to the initial one (Fig.6.5a), which is also confirmed in the work of [40]. The initial predominantly basal texture (Fig. 6.1b) changes slightly, when DRX does not take place. The final texture, without DRX, is a result of predominant slip along the prismatic and pyramidal $\langle c+a \rangle$ systems, in that order. The grain size is also fairly unchanged during the deformation without DRX. The completely different microstructure is obtained, when
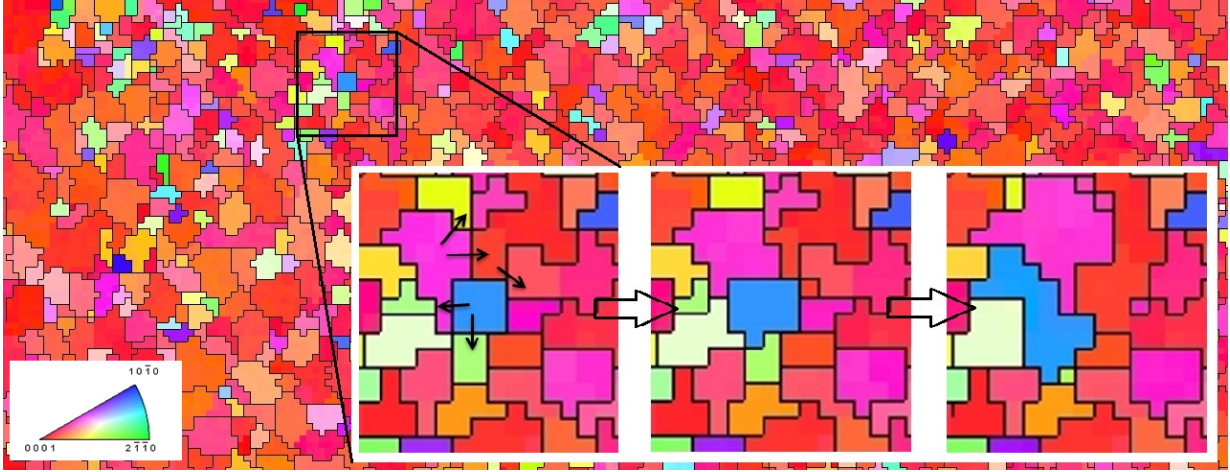
55

Figure 6.4: Schematic representation of growth of a few nuclei through two DRX steps

DRX has taken place, which is shown in Figure 6.5c. It can be clearly seen that a few grains have nucleated and grown to consume most of the matrix grains. The grains stop growing, when the recrystallized grains impinge on each other or they run out of the stored energy advantage. The initial microstructure (Fig. 6.5a) shows that most of the grains seem to have basal texture. This is also supported by the initial pole figure (Fig. 6.1b), which shows a strong basal texture. However, the final microstructure has grains with non-basal texture, which is also seen in the final pole figures shown in Fig. 6.6.

The experimental data of [9] shows that grain orientations do not change much, preserving initial orientation distribution after DRX. Strong fibre texture was maintained after deformation in a Mg-0.8%Al sample as reported by [37]. The predicted pole figures of the final texture after DRX are presented in Fig. 6.6. It can be seen that initial orientation has been slightly rotated, but overall texture is preserved. This effect was explained in [9] by nuclei having similar orientation as matrix. The same trend was seen during tensile tests of AZ31 at 400°C and 500°C performed by Liu et al. [63]. The experimental pole figures of the dynamically recrystallized at 400°C and $\dot{\epsilon} = 1 \times 10^{-3}$ sample from the work of Liu and Wu [63] are shown in Fig. 6.7. The original basal texture was rotated up to 30 degrees perpendicular to tensile axis parallel to RD. At higher strain of (77%) the basal plane was aligned normal to TD direction at 500°C.

To study the evolution of texture due to deformation and DRX, the initial and final misorientation distribution of the sample is calculated and presented in Fig. 6.8. These figures show the number fraction of pixel pairs having a certain misorientation. In both cases pixels with misorientation less than 2° are included in the analysis. Initial sample has

(a)

(b)

TD

RD

$10\bar{1}0$

0001 $2\bar{1}\bar{1}0$
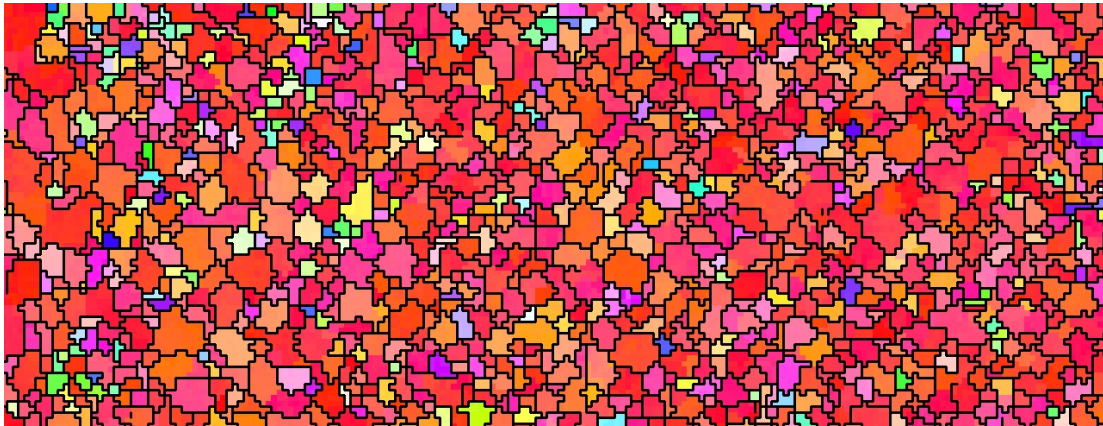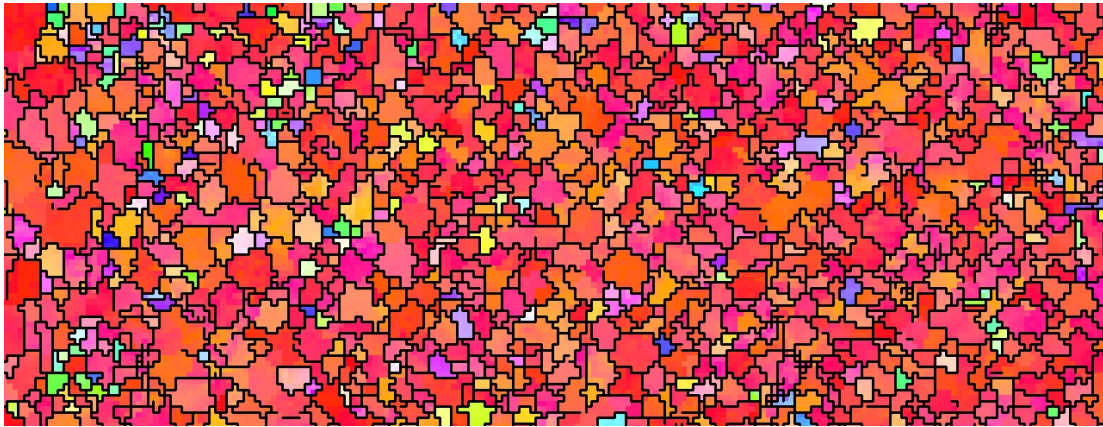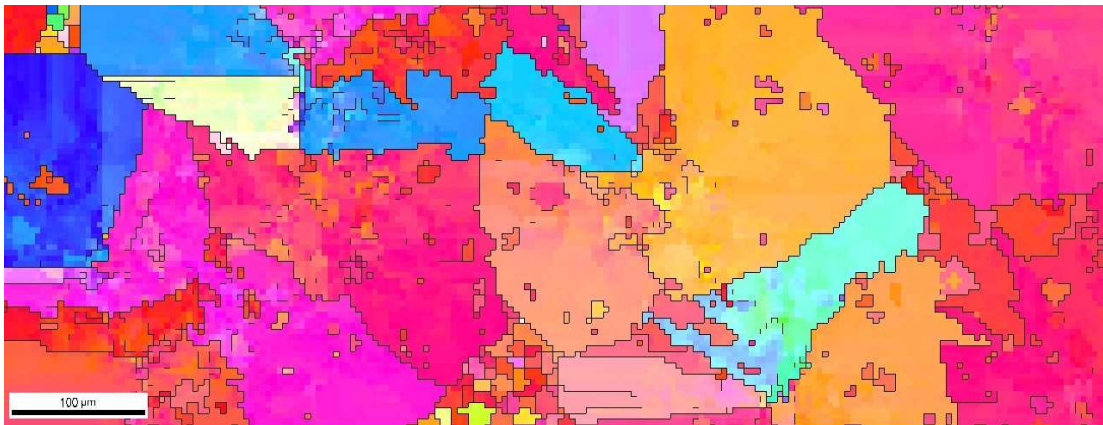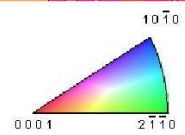
(c)

Figure 6.5: EBSD IPF maps of (a) Initial microstructure used as input (b) Simulated up to 35% of tensile strain without DRX (c) Final simulated microstructure after DRX
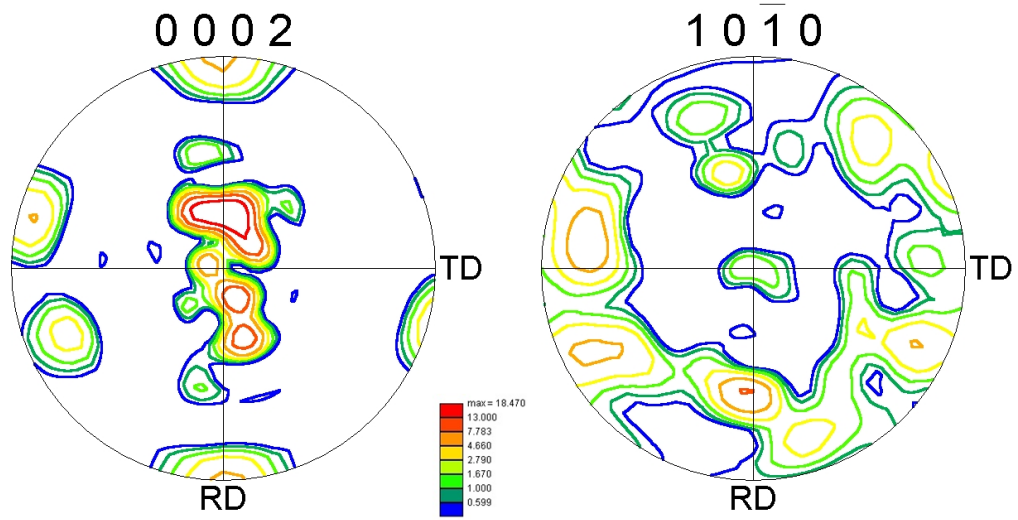
Figure 6.6: {0001} and {10$\bar{1}$0} pole figures of the recrystallized sample after 35% tension (after DRX)

Figure 6.7: Experimental {0001} and {10$\bar{1}$0} pole figures of the recrystallized sample after 40% tension at 400°C, 1×10^{-3} (after DRX) [63].

a wide spread of the misorientation angles with peak intensity at about 30° degrees. As stated earlier, all points inside the grain are initially assigned the same value as the average texture of the grain. Hence the contribution to the distribution is only from inter-granular boundaries. Thus, there are many high angle grain boundaries in the sample which can act as potential nucleation 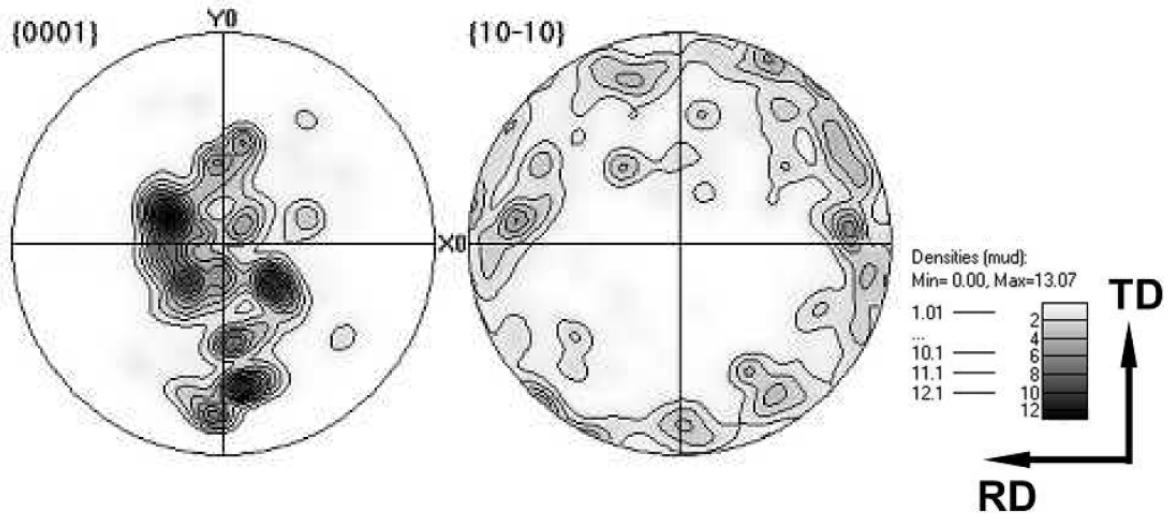sites for DRX since the mobility of the grain boundaries are directly related to the misorientation. However, the simulation shows that, after deformation, the peak density of the misorientation angle distribution shifts to the left (indicating low misorientation angle) (Fig.6.8). During the DRX the elements in the CPFEM undergo continuous deformation. This results in texture rotation in each element. Depending on the exact strain path each element sees the amount and nature of this texture rotation is different in each element. As a result the elements inside the same grain see different rotation paths. This leads to elements in the same grain to develop a misorientation higher than the cutoff of 2°. Thus, most of the contribution to the first 2 bins in Fig. 6.8b is due to intragranular boundaries. Some of the contribution can also be due to the new recrystallized grains having orientation close to the other grains they impinge on.

Grain size distribution is shown in Fig. 6.9. In the undeformed sample, the average grain size is $\sim 14\mu m$, and the final (after DRX) average grain size is $\sim 120\mu m$. The initial grain size distribution has a single peak around 16 μm and shows a log normal distribution of grain size. The deformed (and DRX) sample exhibits a double peak one close to the lower grain size while the other close to 100 μm. It can be seen from EBSD IPF map in Fig. 6.5c, that certain grains have grown drastically (DRX), while some grains are left with the initial size (no DRX). This similar to the behaviour observed during tensile test of AZ31 at 200C in the experimental work of [9]. To explain this phenomenon, why only a certain grains grow while others do not, the normalized dislocation density distribution (normalized with respect to the maximum) is analyzed at the beginning (after 3% strain) of the simulation and after DRX in Fig. 6.10. Both meshes were overlaid with grain boundaries. In Fig. 6.5c along bottom edge close to middle one can clearly see a group of grains that have not recrystallized. In the same area in Fig. ?? the normalized dislocation density is close to 0.3. Even though neighbouring grains can have high dislocation density content, their mismatch (Eqn.5.25) might not satisfy the nucleation criteria described in the previous chapter. At the end of the simulation the DDT in the same area is almost negligible. One can safely assume that at no point during the entire DRX process this area managed to generate the right conditions for DRX nucleation to take place or the area to be consumed by growing DRX nuclei.

During the deformation, the sample is not fully recrystallized after 35% strain in Fig. 6.11. The predicted behaviour of the volume fraction of recrystallized elements is similar to the Johnson-Mehl-Avrami-Kolmogorov curve, however, it is obtained from the CPFEM
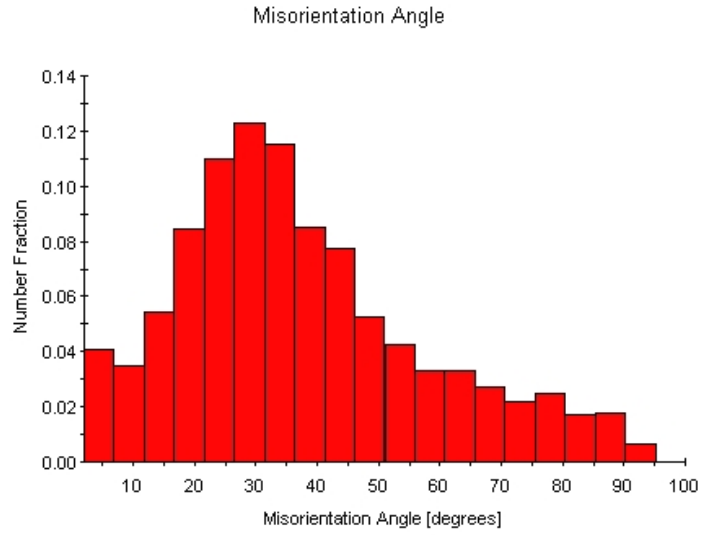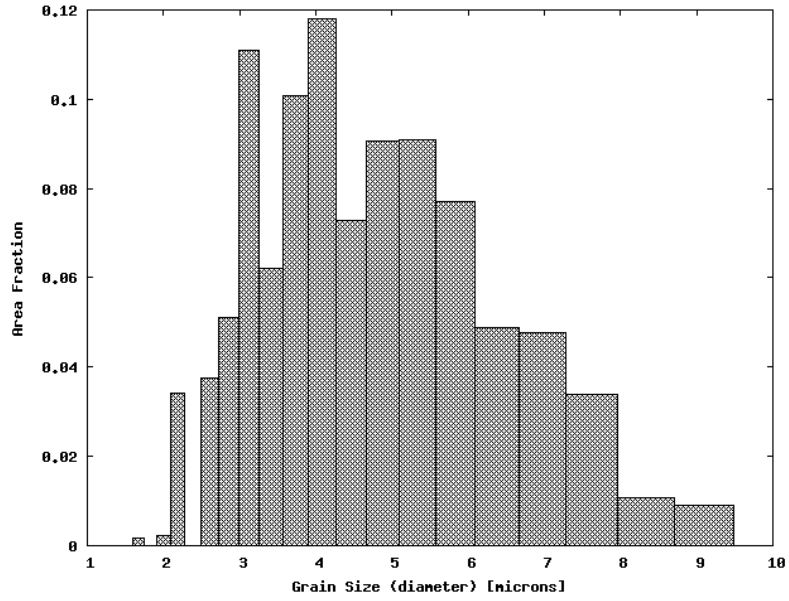
(a)
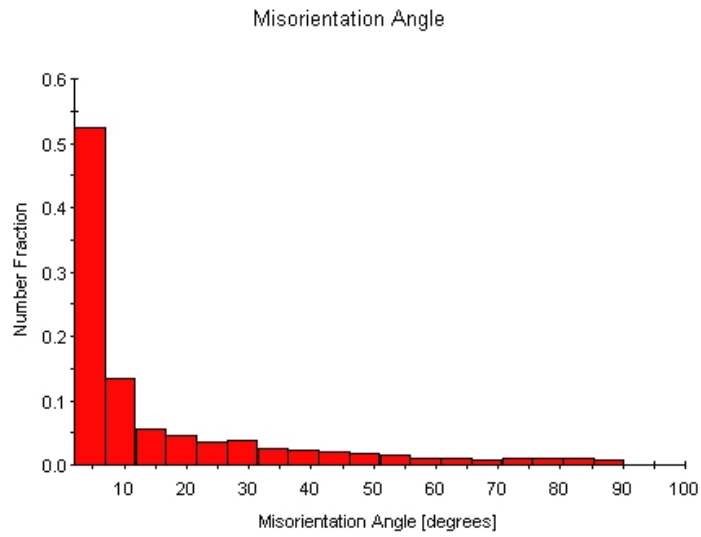
(b)

Figure 6.8: Distribution of the misorientation angle through the sample (a) Initial (unde-formed) and (b) Final (after DRX)

(a)
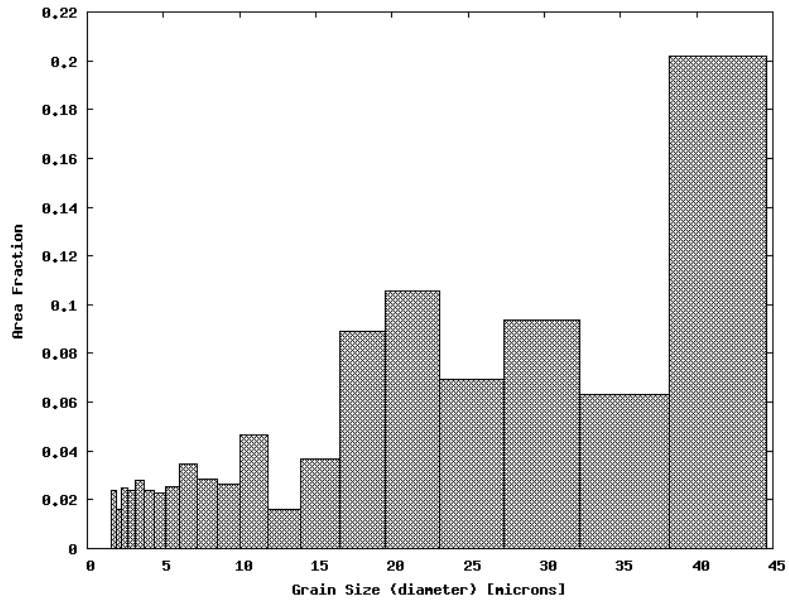
(b)

Figure 6.9: Grain size distribution (a) initial (undeformed) and (b) final (after DRX).

61
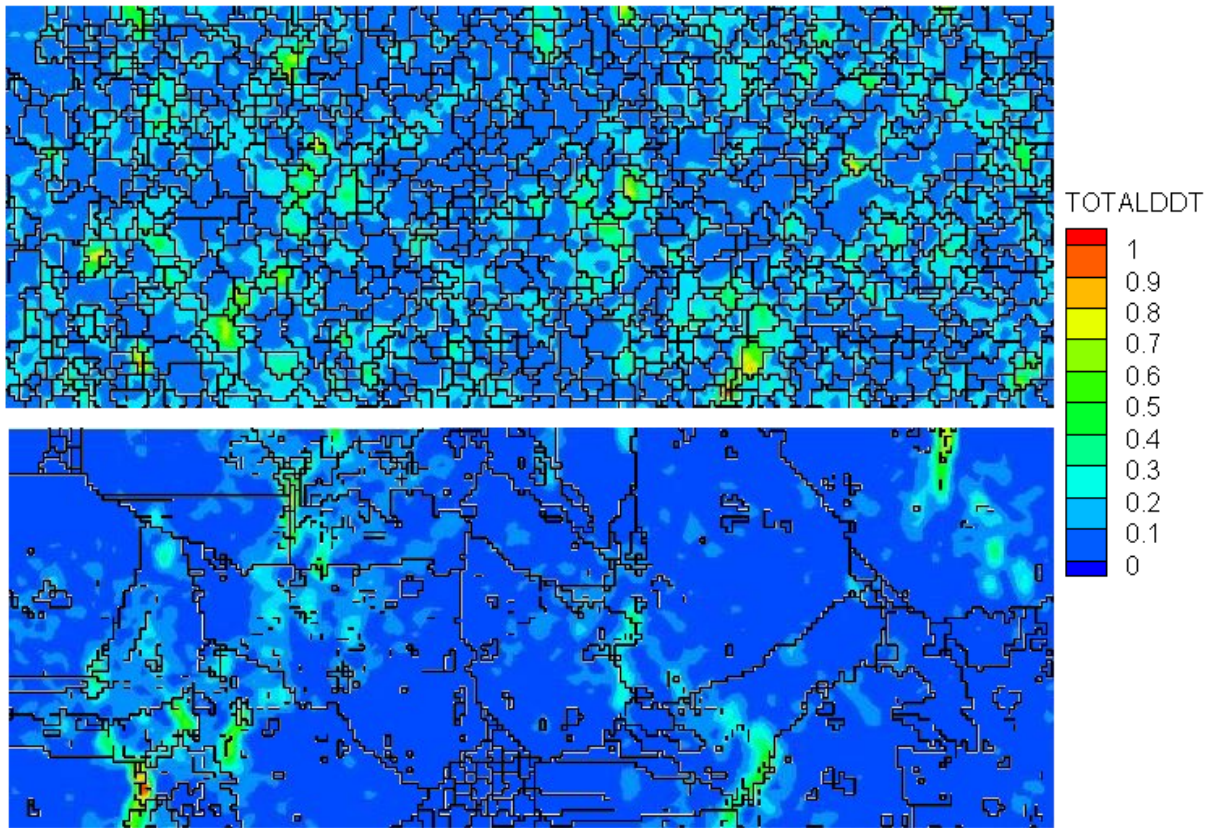
Figure 6.10: Normalized distribution of dislocation density over the sample (a) Initial at $\sim 3\%$ strain (b) Final (after DRX).

simulations rather than the analytical expression. Note that the rate of recrystallization can be controlled by changing threshold parameters $d\rho_{cr}$ and grain boundary mobility (depending on the temperature). The effect of these parameters is studied and presented in the Chapter 7.
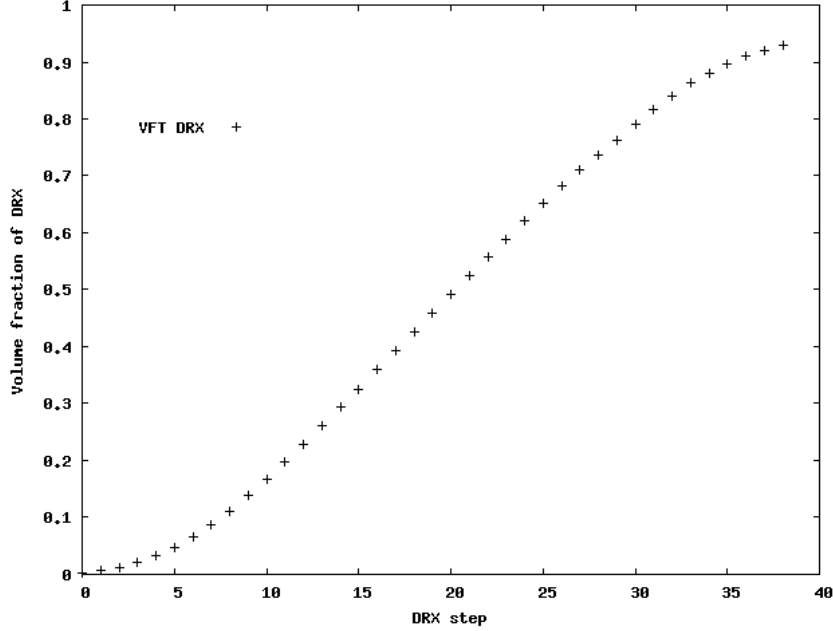
Figure 6.11: Volume fraction of recrystallized elements obtained from the simulation.

Predicted pole figures after 35% of tensile strain (Fig.6.13) show the development of $(10\bar{1}0)$ intensity. The same results were obtained for Mg AZ31 at various temperatures and strain rates in the experimental analyses of mechanical response of AZ31 alloy by Khan et al. [40]. The increasing intensity of the six prismatic planes with increasing temperature can be explained by the activation of prismatic slip due to low CRSS. The analysis of CRSS values for different slip systems at various temperatures demonstrates that basal slip is still the most favourable slip system during tension along RD, however, at higher strains ($\geq 40\%$) (and at higher temperature) $\{11\bar{2}2\}\langle11\bar{2}\bar{3}\rangle$ pyramidal slip is activated [63].

The predicted stress-strain curves obtained from models with and without DRX as well as the evolution of the volume fraction of recrystallized elements is presented in Fig. 6.12. The onset of DRX occurs right before the peak stress, causing softening later. This was reported in the experimental work of Galiyev et al. [10] validating the simulation results.
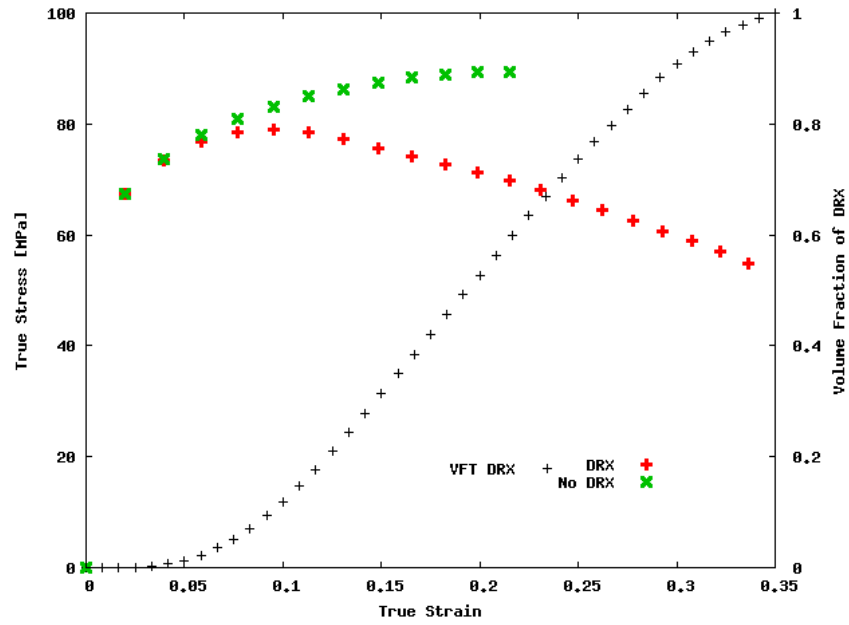
Figure 6.12: The plot of true strain vs. true stress curves of the simulations with and without DRX on top of the evolution of the volume fraction of DRX
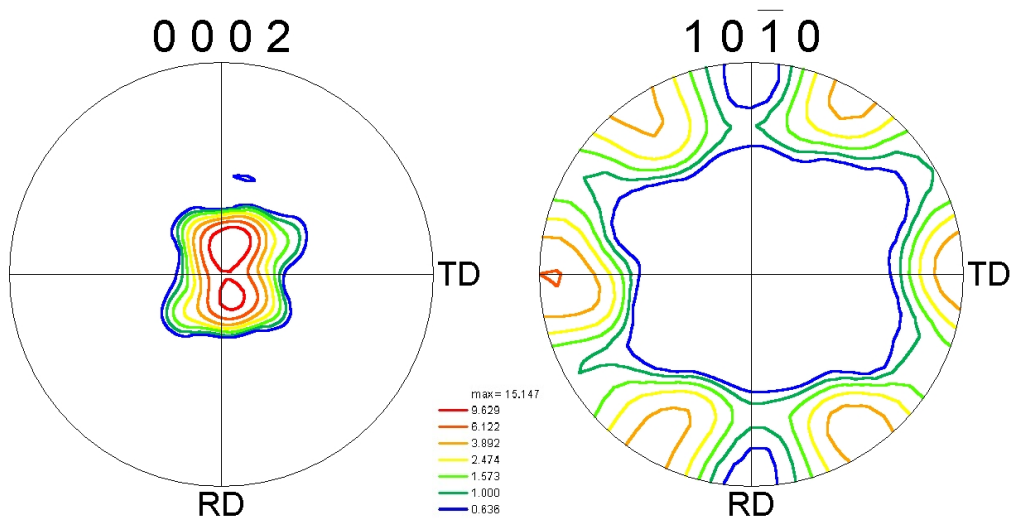
Figure 6.13: {0001} and {10$\bar{1}$0} pole figures after 35% tension without DRX

6.1.4 Conclusions

- The capability of the new DRX-CPFE model is demonstrated by simulating a tensile test of AZ31 Mg alloy.

- During the tensile test of AZ31 alloy twinning is not active and the deformation is accommodated by basal and prismatic slip systems.

- The model is able to capture the softening behaviour as well as dislocation density distribution during DRX. In the simulation, DRX reaches almost 100%, leaving 'strain free' grains.

- The grain size distribution shows that after DRX the average grain size increased compared to the initial distribution.

- According to the simulation results, the final texture does not change significantly after DRX in AZ31, which was also shown experimentally in [9, 64].

## 6.2 Dynamic recrystallization with twinning: The Role Of Deformation Twinning In Modeling DRX

The present section provides the extension of the model to include the deformation twinning and investigate its effect on the evolution of DRX. Extension twins are one of the major deformation mechanisms in magnesium alloys, they occur when a compressive load is applied perpendicular to the c-axis, so that c-axis is under a tensile load (Fig.6.14). Twinning is known to be more prominent at room temperature, and yet, the presence of deformation twinning at elevated temperatures was also reported in the literature [23, 146, 44]. However, much uncertainty still exists about twinning behaviour during high temperature deformation. This indicates a need to understand the effect of deformation twinning on DRX.

The incorporation of twins within the current model is accomplished by considering the effect of the twin orientations on the texture evolution during DRX. Contraction twins are not taken into account due to their thin size and inability to grow. When extension twins are active, they are known to induce S-shaped hardening curve [40, 147, 38]. However, capturing that behaviour of the stress-strain curve is beyond the scope of this study and will not be discussed here. Rather, modelling a softening due to DRX as well as a microstructure evolution are the main objectives of the proposed model.
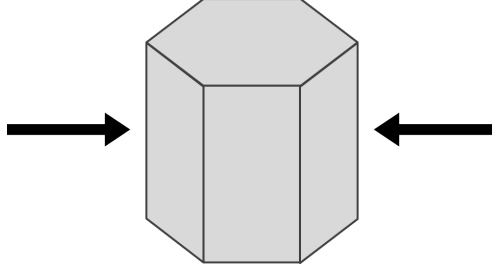
Figure 6.14: Schematic of loading direction

6.2.1 Modelling procedure

In order to include deformation twinning within the DRX-CPFEM, the following method is developed. The main idea of the proposed approach is a geometrical incorporation of twins into a discretized sample. Throughout the deformation before the initiation of DRX, an element is reoriented to the dominant twin orientation depending on the volume fraction of twins accumulated at that strain level. The volume fraction of twins has to reach a certain threshold to be reoriented. The threshold value is determined for each simulation. The reorientation procedure is similar to the predominant twin reorientation scheme (PTR) introduced by Tome in [27]. When an element takes a new orientation, the matrix fraction is set to zero (Fig. 6.15a). The basic assumption is that the nucleated twins do not grow during further deformation, and they can act as the potential nucleation sites. Therefore, a grain (consisting of a few elements) can be divided into two grains as presented in Fig. 6.15b, where M and TW denote matrix and twin respectively, or an entire grain can be reoriented to a twin orientation based on the volume fraction of twins. Another assumption is made regarding the dislocation content of the twins. Dislocation content inside twins is still not certainly understood in literature, and there is no evidence that twins have lower or higher dislocation density than the matrix. Therefore, in the model, a rotated element inherits the dislocation content accumulated by that element before the reorientation.

Since deformation twinning is not active during further deformation after the reorientation, the rate of twinning is set to zero the element is reoriented:

$$\dot{f}_{(\beta)} = 0 \tag{6.2}$$

Accordingly, the plastic parts of the rate of deformation and spin get the following simple form:

$$D^p = \sum_{\alpha=1}^{N^s} P_{(\alpha)} \dot{\gamma}_{(\alpha)} \quad \Omega^p = \sum_{\alpha=1}^{N^s} W_{(\alpha)} \dot{\gamma}_{(\alpha)} \tag{6.3}$$

66

M	M	M	M	M
M	M	M	M	M
M	M	M	M	M
M	M	M	M	M
M	M	M	M	M

$\longrightarrow$

M	M	Tw	Tw	Tw
M	M	Tw	Tw	Tw
M	M	Tw	Tw	Tw
M	M	Tw	Tw	Tw
M	M	Tw	Tw	Tw
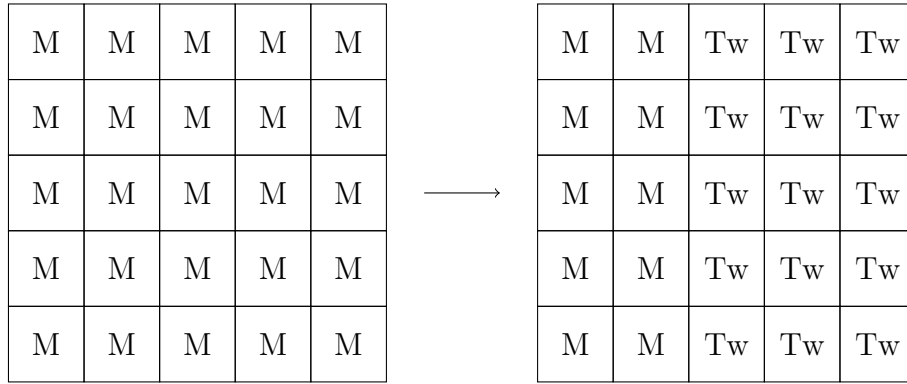
Figure 6.15: Schematic representation of the twin incorporation into the mesh

and where $\dot{\gamma}_{(\alpha)}$ is the shear rate on the slip system α. And the Cauchy stress is calculated without the twinned part.

For example, after the reorientation of the sample with the volume fraction of twins about 50%, the misorientation angle distribution reveals a high peak of 86 degrees compared to the initial distribution, which indicates the reoriented twins (Fig. 6.16). Note that extension twins reorient a crystal orientation for 86 degrees.
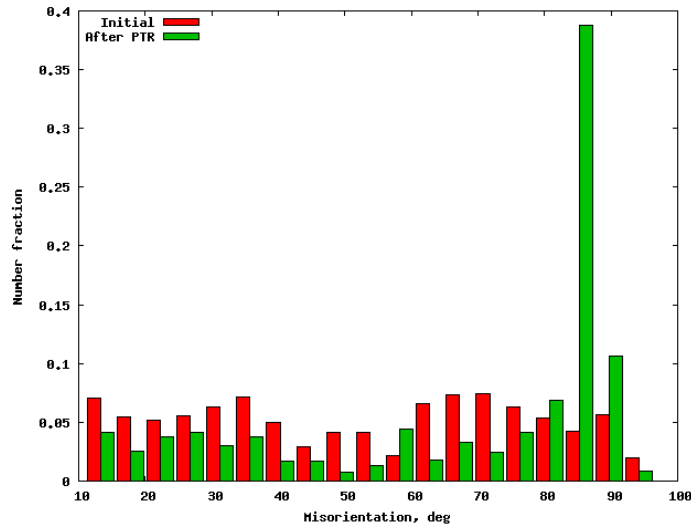
Figure 6.16: Misorientation angle distribution: initial and after reorientation (degrees < 10 are excluded)

Fig. 6.17 represents an example of the EBSD maps prior to and after the reorientation is

completed, as well as the partitioning of the twinned and matrix elements. The partitioning shows which elements were reoriented to the twin orientations. It can be seen that some of the grains were entirely reoriented, while some of the single elements within the grains were reoriented. The threshold of the volume fraction of twins for reorientation used in this simulation is 60%, and DRX proceeds with the "new" microstructure.

Thus, the general strategy of the incorporation of deformation twinning into DRX-CPFE model is as following:

- Deformation twinning is active and evolves until the DRX step is taken.

- The reorientation of an element (integration point) is accomplished based on the dominant twin orientation, once the volume fraction of twins reaches the chosen threshold.

- DRX proceeds with a new microstructure with rotated twin orientations. Further twin evolution is suppressed.

6.2.2 Experimental and input data

The experimental results for the model validation are taken from the published literature [23, 59, 66, 148, 56]. In these works, the authors performed the series of tests including uniaxial compression and channel die compression on the extruded commercial magnesium alloy AZ31. A few different orientations were considered, namely, when c-axis is parallel, perpendicular and 45 degrees to the loading direction. In the present work, in order to analyze the behaviour of the extension twins during DRX, the data for the orientation CD0ED (c-axis is perpendicular to the extrusion axis) is chosen. The EBSD map of an extruded AZ31 magnesium alloy used as input to the DRX-CPFEM is presented in Fig. 6.18 along with the pole figure. The pole figure is similar to the one provided in the experimental data. The ED is perpendicular to the plane, and a and b are the radial directions. The original EBSD map is re-sampled, and the step size is $9\mu m$ in both x and y directions.

6.2.3 The simulation results

Compressive load is applied along the extrusion direction (ED), so that c-axis is under a tensile load, which is favourable for the extension twinning [149]. The Fig. 6.19 shows the schematic of the HCP crystal orientations on the pole figure.

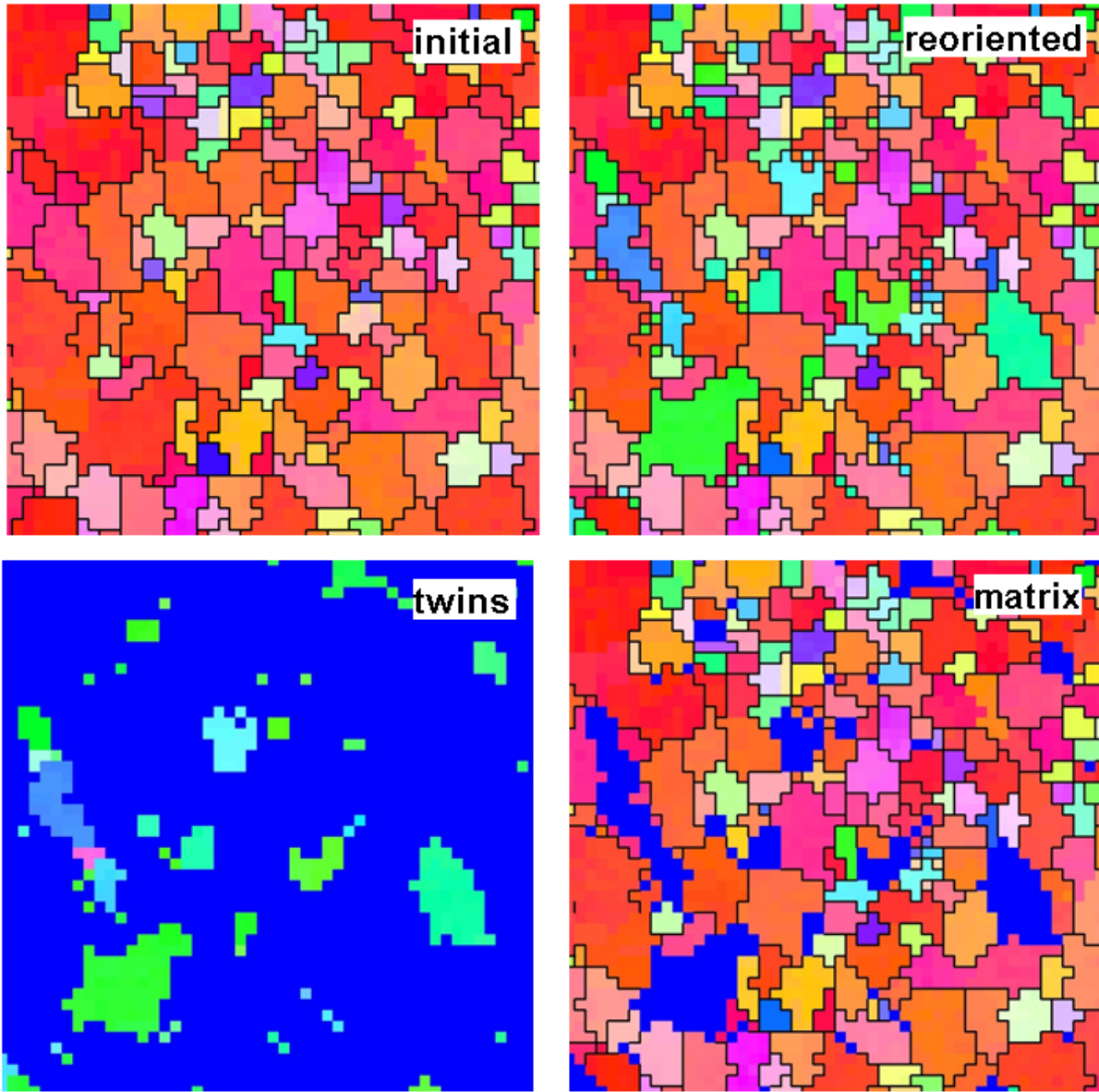Temperature-dependent parameters of the model are as follows:

Figure 6.17: Example of the reoriented structure: EBSD IPF maps showing initial and reoriented structure and partitioning of the twins and the matrix.
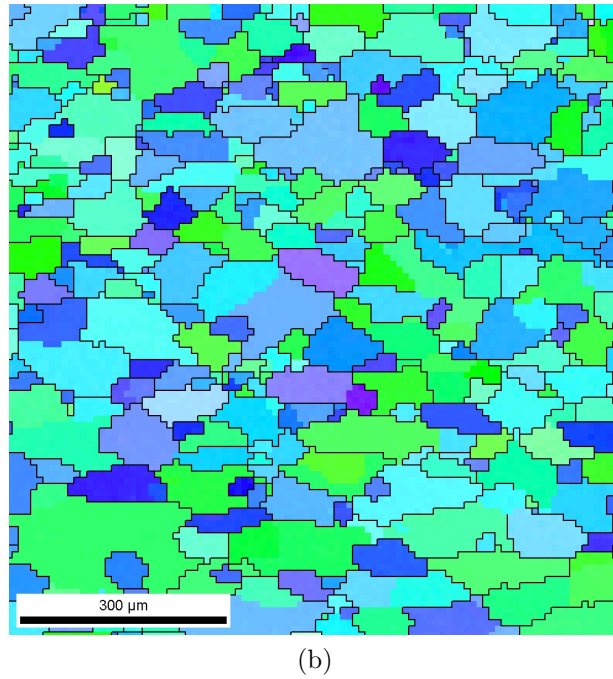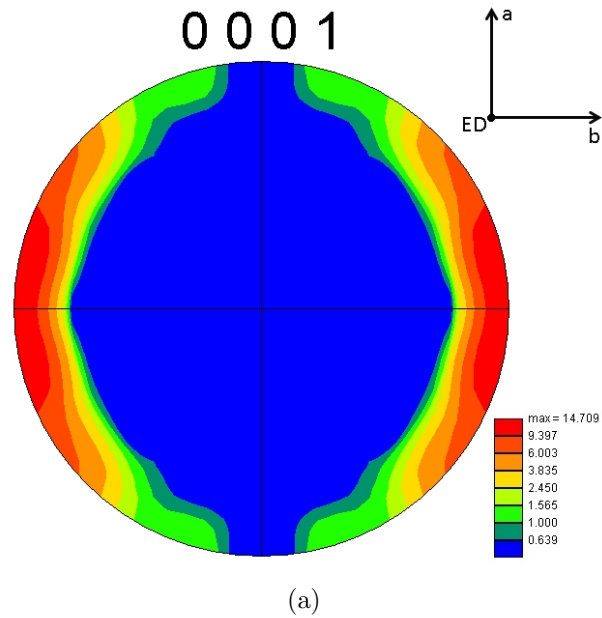
Figure 6.18: Initial texture of the extruded AZ31 Mg alloy (a) Pole figure; (b) EBSD IPF map.
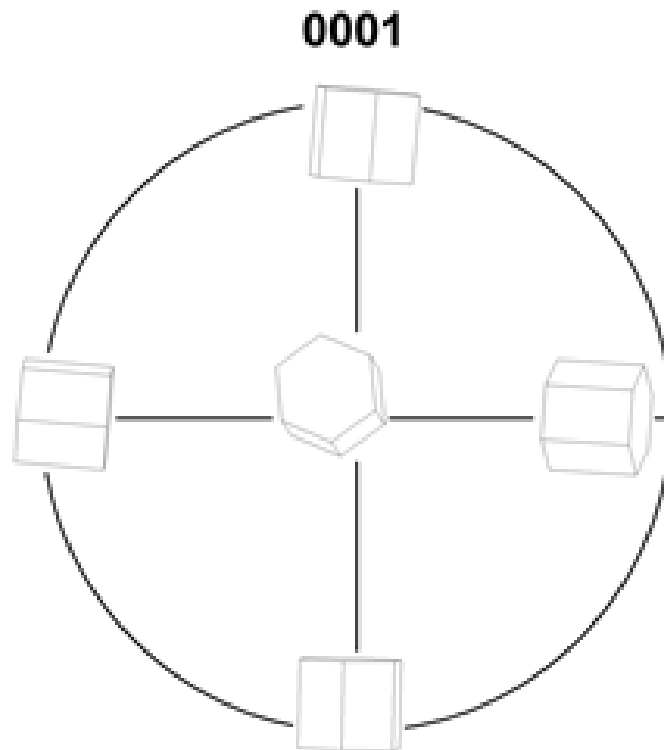
Figure 6.19: Schematic of the location of HCP crystal orientations on the pole figure.

- CRSS values for slip systems, which are calibrated depending on the yield point of the stress-strain curve.

- Critical condition for DRX initiation (Equation 5.22) and nucleation (Equation 5.25). Since at higher temperatures DRX starts earlier, the value of ρ_{cr} decreased to allow more grains to recrystallize. The magnitude of the $d\rho_{cr}$ is also lowered with increasing temperature providing more potential nucleation sites.

- Grain boundary velocity, which depends upon mobility curve. At higher temperatures, the mobility of the grain boundary is higher, hence, it has higher velocity to travel the size of the element. Therefore, the DRX time step becomes smaller.

First, the crystal plasticity model parameters need to be calibrated for each simulation temperature. The correlation between the critical resolved shear stress (CRSS) values for different slip systems and temperature was investigated in many works, however, the evidence for this relationship is still inconclusive. For the various crystal plasticity models the obtained CRSS values have a broad spread [147], for example, in [42], the ratio of CRSS values for intermediate hot working temperatures is taken to be as $\tau_{basal} : \tau_{prismatic} : \tau_{\langle c+a \rangle} : \tau_{twinning} \sim 1 : 6 : 5 : 6$. The CRSS for deformation twinning is assumed to be temperature insensitive [64, 42], therefore, in the current simulations, the CRSS is kept the same for all the temperatures. The CRSS magnitudes used in the present simulations are presented in Table 6.2.

Table 6.2: CRSS values for different temperature simulations. The strain rate is the same $\dot{\epsilon} = 10^{-4} s^{-1}$

Temperature	basal	prismatic	pyramidal $\langle a \rangle$	pyramidal $\langle c + a \rangle$	twinning
200°C	18.0	30.0	45.0	38.0	30
300°C	6.0	9.0	14.0	14.0	30
400°C	2.5	4.2	4.2	5.0	30

In the current simulations, the CRSS values have been calibrated to fit the yield point of the experimental curves. First, the assumption was made that CRSS values are linearly dependent on temperature. Hence, the values for 200°C and 400°C were obtained by fitting, then, the values for 300°C were interpolated. However, since the compression at 200°C was dominated by twinning, the yielding point was governed by the CRSS of the twin systems. Therefore, the linear interpolation did not give a good match (the results are not presented here), and the values for 300°C also were obtained by calibration. The CRSS values for different simulated temperatures are presented in Fig. 6.20. It is clear from the figure that
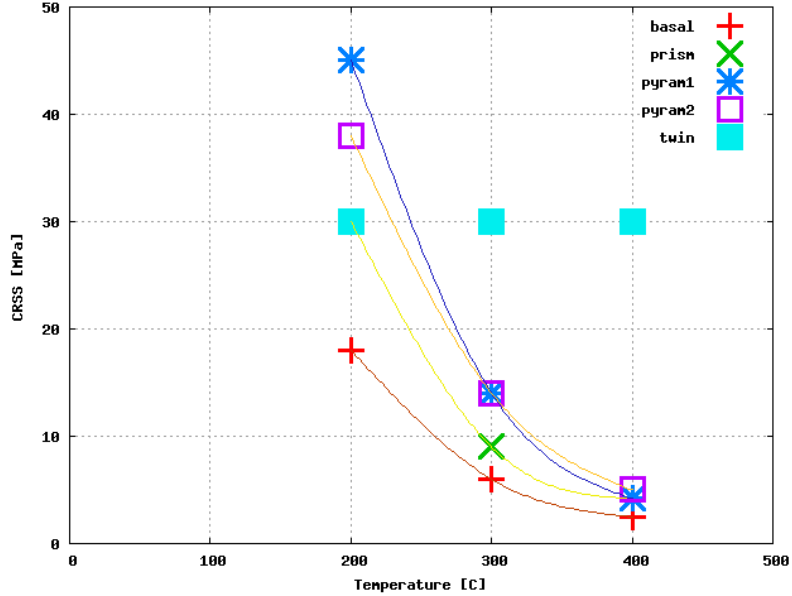
Figure 6.20: CRSS values for slip systems used in the simulations for different temperatures

the dependence is not linear. However, when the radial direction compression is simulated, a lower fraction of twins is observed, and the yielding point is not completely defined by the twin CRSS. And therefore, the linear approximation gives better fit (not presented here). Taken together, these results suggest that there is no linear correlation between CRSS values and temperature (between 200°C and 400°C), when twinning is active.

The simulation results for the compression test at 200°C are presented below. The strain rate is taken to be the same for all the simulations ($\dot{\epsilon} = 10^{-4}s^{-1}$). During the earlier stages of the deformation, the reorientation of the elements is performed once the volume fraction of twins in the element reaches a certain threshold (taken to be 60% in the simulations). The histogram of the number of the reoriented elements at each incremental time step is given in Fig. 6.21 along with the evolution of the total volume fraction of twin. The total number of the reoriented elements for 200°C compression is about 70%.

The experimental and simulated stress - strain curves for compression test at 200°C are presented in Fig. 6.22. The predicted stress-strain curve shows a good match with experimental data. The peak stress is controlled in this case mostly by the twinning, and the softening behaviour is well captured by the DRX-CPFE model. It should be mentioned that the calibration of the flow curves is performed only to fit the yielding point, the rest of the flow curve as the first peak and subsequent softening behaviour are controlled by the DRX evolution.
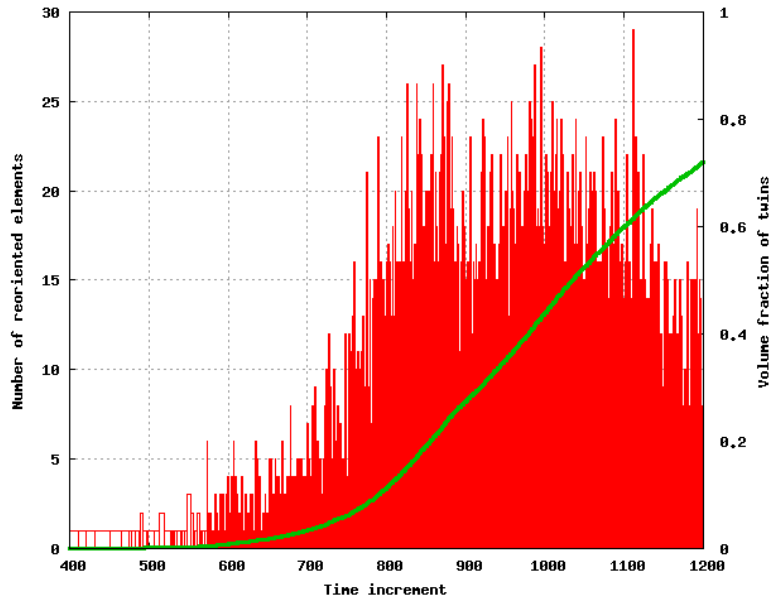
Figure 6.21: Histogram of the number of the reoriented elements and the volume fraction of the reoriented elements vs. time increment.
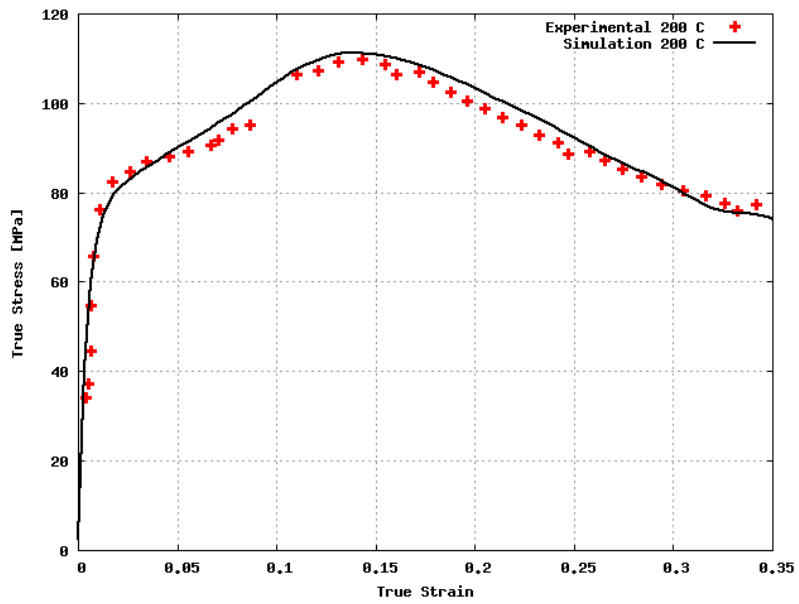
Figure 6.22: Experimental [148] and simulated true stress vs. true strain curves for 200°C

74

The final texture, obtained from the simulation at 200°C is presented in Fig. 6.23. The initial extruded sample had c-axes lying perpendicular to the extrusion direction (ED) with basal plane normals pointing around the radial direction (see Fig. 6.18). The final texture shows that the orientations between 0002 and 10$\bar{1}$0 poles have been reoriented during the deformation. However, the texture strength did not change significantly, which might be because the nuclei inherited those initially strong orientations at 0002 and 10$\bar{1}$0. Hence, the slip systems activity shows that the deformation is dominated by prismatic and basal slip systems, also pyramidal $\langle c + a \rangle$ slip is activated due to the twin reorientation (Fig. 6.24a). The deformation twinning causes 86 degrees rotation of the basal 0002 planes towards the extrusion direction, and it becomes favourable for pyramidal $\langle c+a \rangle$ slip. The total fraction of twins during this simulation reached about 70%. Fig. 6.24b presents the evolution of the volume fraction of the recrystallized elements throughout the deformation.
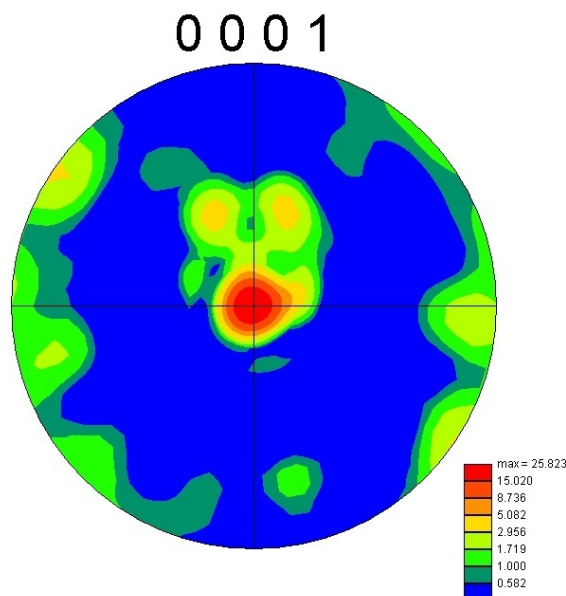
Figure 6.23: Final {0001} pole figure after DRX at 200°C

The experimental pole figures after DRX taken from literature [39] are presented in Fig. 6.25. The initial pole figure was fiber textured with c-axes perpendicular to the ED. The final pole figure at 200°C (Fig. 6.25a) shows that most of the crystals were reoriented about 90 degrees forming basal texture at the end.

The stress-strain curves of the compression along the ED at 300°C and 400°C are presented in Fig. 6.26. The results show a very good match with experimental curves.
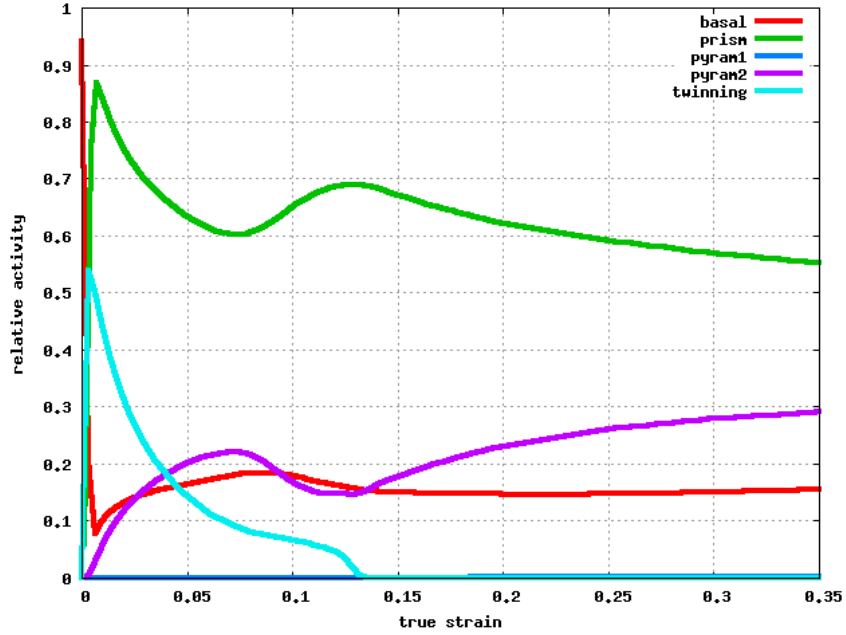
(a)
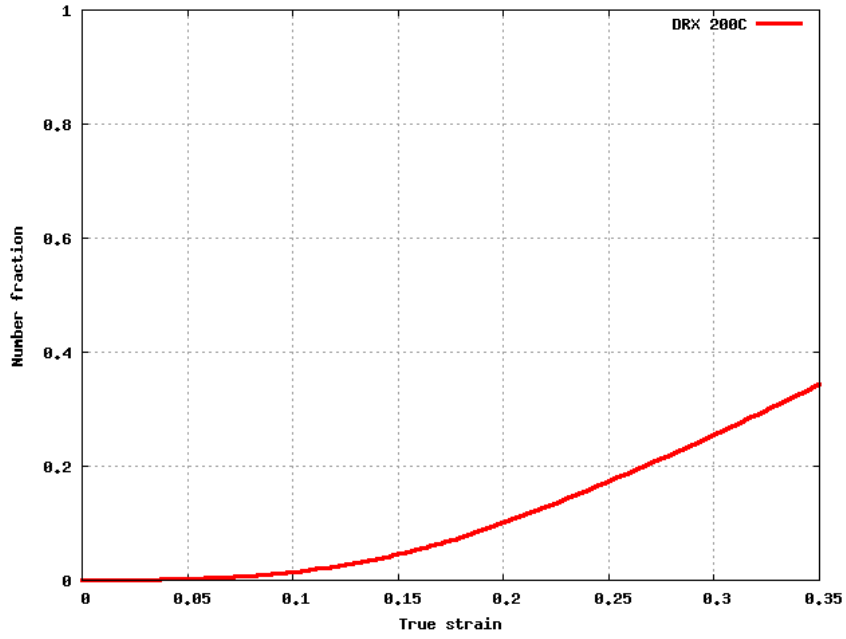
(b)

Figure 6.24: Simulation results of 200°C compression (a) Slip systems activity (pyram1 and pyram2 denote pyramidal a and $\langle c + a \rangle$ systems respectively (b) Evolution of the volume fraction of DRX.
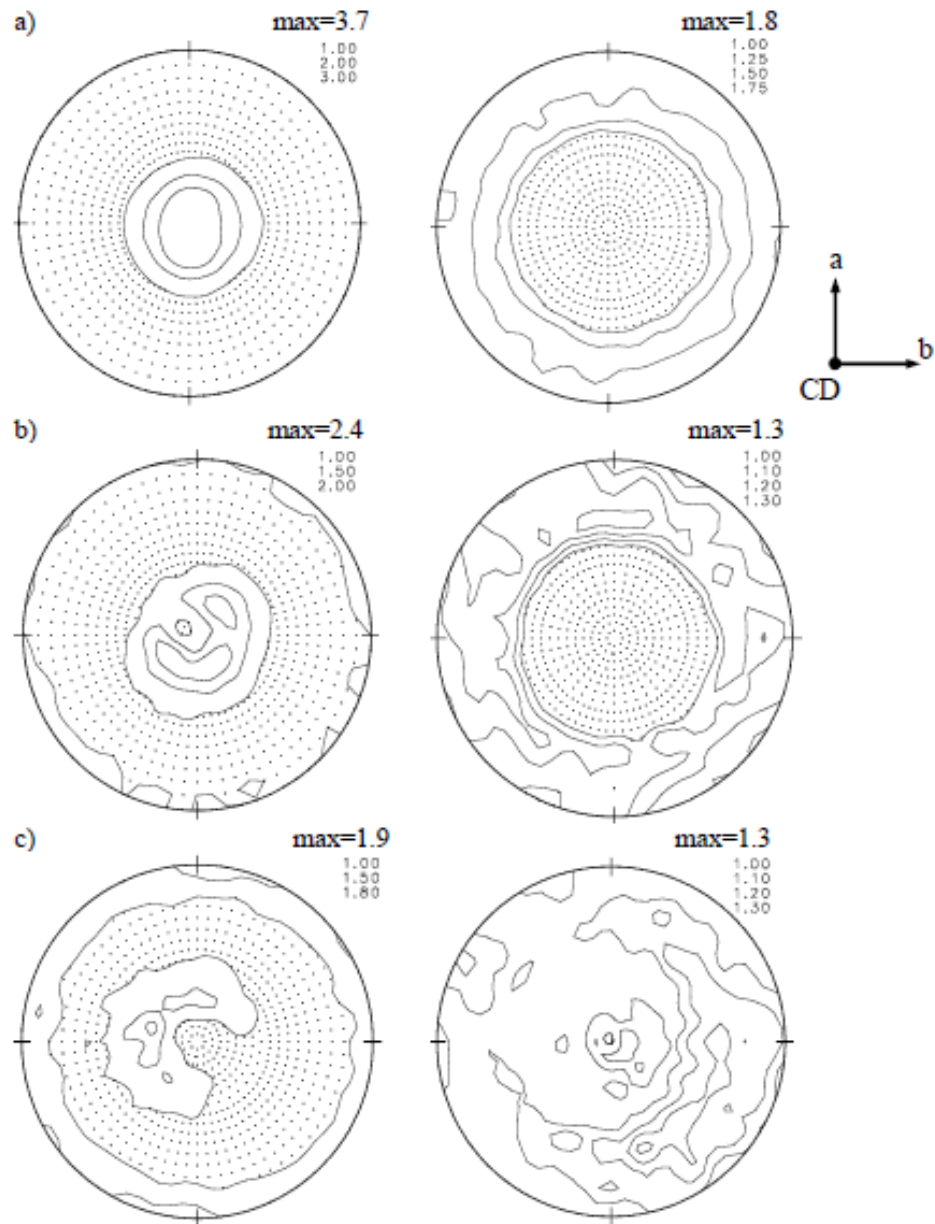
Figure 6.25: Experimental final {0001} and {10$\bar{1}$0} pole figures after DRX at different temperatures from [39] (a) 200°C (b) 300°C (c) 400°C.
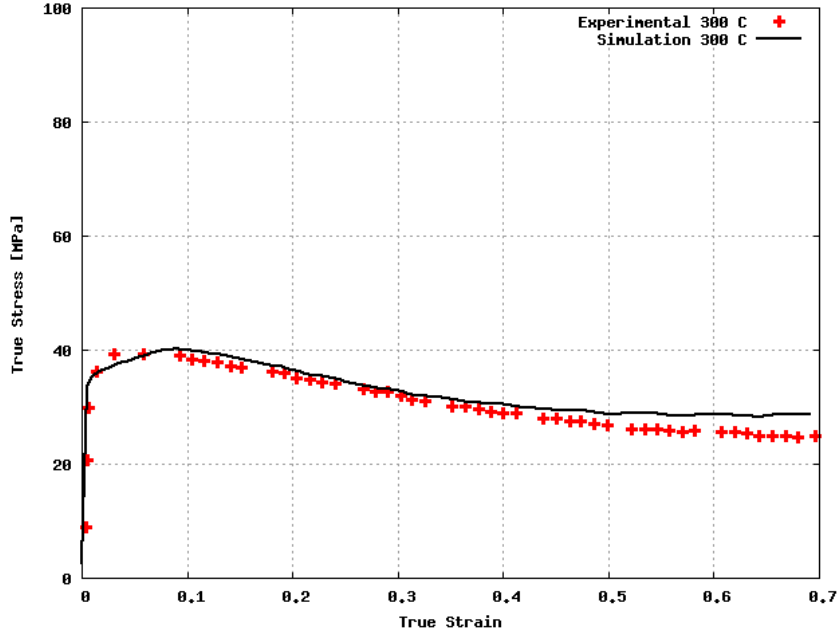
(a)
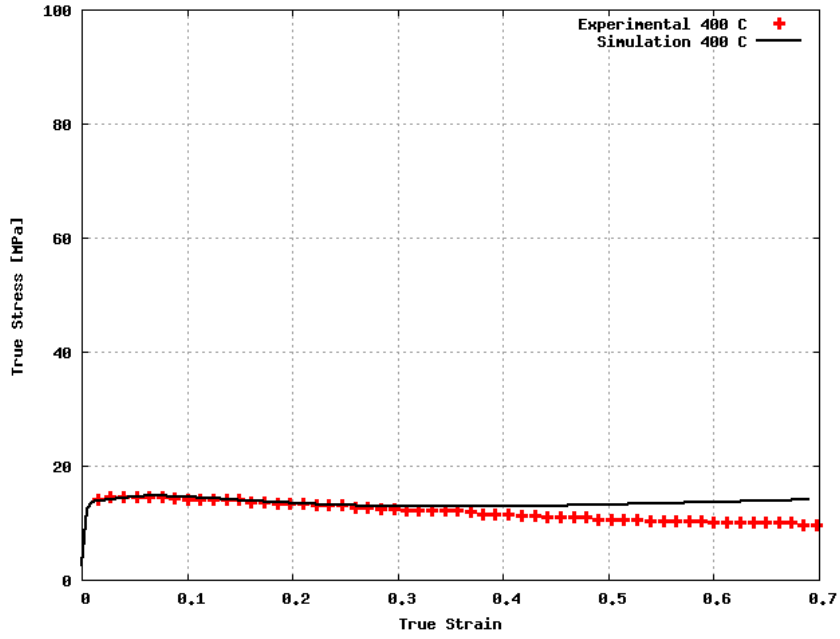
(b)

Figure 6.26: Experimental [148] and simulated true stress vs. true strain curves for the ED compression at (a) 300°C (b) 400°C

At the higher temperatures, the deformation twinning is not observed due to the lower CRSS values for non-basal slip systems. During uniaxial compression along the ED, prismatic slip is highly favourable as well as twinning or pyramidal $\langle c + a \rangle$ slip. However, as shown in Fig. 6.27a, prismatic slip is dominant throughout the deformation at 300°C. Only about 2% of twinning is observed during 300°C compression. Since the CRSS for pyramidal $\langle c + a \rangle$ slip is lower than the CRSS for twinning, the strain along c-axis is accommodated by pyramidal $\langle c + a \rangle$ slip system. Such more favourable conditions for DRX were reported in [49], when basal, prismatic and pyramidal $\langle c + a \rangle$ slip systems were active. However, at 400°C deformation, pyramidal $\langle c + a \rangle$ slip is the most dominant, and the first order pyramidal a is active along with prismatic slip system (Fig. 6.27b). The results indicate that non-basal slip systems take over the deformation at elevated temperatures, and twinning is not active at these deformation conditions.

Fig. 6.28 illustrates the evolution of the volume fraction of recrystallized elements during the compression simulations at 300°C and 400°C. At 400°C the sample was fully recrystallized by the end of the simulation, while at 300°C 80% of the elements were recrystallized. These results are consistent with those of the other studies [23] and suggest that the lower temperature DRX leads to a lower fraction of the recrystallized grains.

The grain size distribution histograms at different temperatures after DRX are illustrated in Fig. 6.29. The initial data has bimodal distribution, while at 200°C the recrystallized grains (35% see Fig. 6.24b) appear in the first peak of the histogram. However, the rest of the distribution remains the same with lower fraction. After 400°C simulation it can be seen that a larger grain size is developed and formed a peak at $40\mu m$. This implies that the viable nuclei from the earlier steps have grown into larger size grains, and the grains recrystallized later contribute to the first high peak of the histogram plot.

In the present model, since the nucleation sites consist of the subgrains, they have the same or similar orientations as the parent grains. The rotation of crystal due to slip alone in magnesium alloys reaches up to ~ 30 degrees, and texture in magnesium alloys is known to not change significantly after DRX compared to FCC metals [39]. The reason is the activation of basal and prismatic slip systems, which accommodate most of the strain during the deformation. Therefore, the final textures are not much different from the initial one after 300°C and 400°C compression tests (Fig. 6.30). The 400°C pole figure shows the splitting poles that form pyramidal texture, which also was reported in previous studies [148]. The predicted {0001} pole figure after DRX at 300°C does not have any signs of twinning, however, in the experimental pole figure (see Fig. 6.25b), there are basal poles with c-axes oriented parallel to the ED, which indicate twinning. The reason of this mismatch might be that the CRSS value for twins at 300°C is much higher than the CRSS value for $\langle c + a \rangle$ pyramidal slip system. This can lead to the assumption that the CRSS
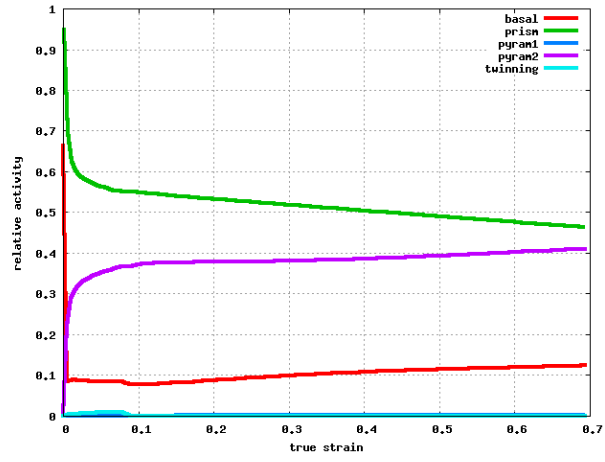
(a)
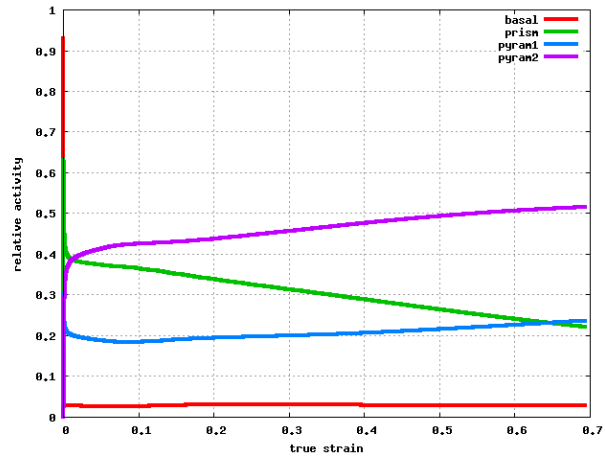
(b)

Figure 6.27: Slip systems activity during ED compression simulations at (a) 300°C (b) 400°C.
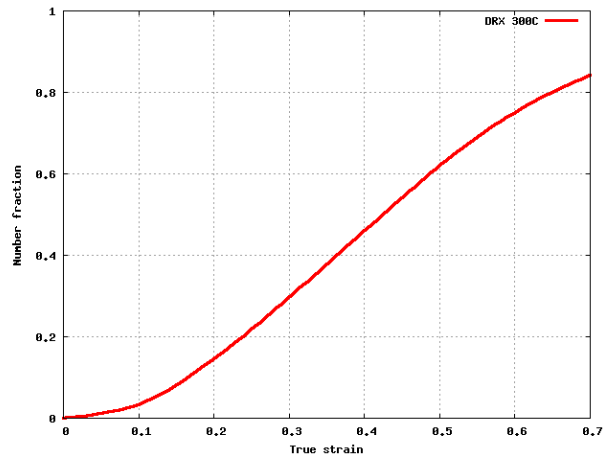
(a)
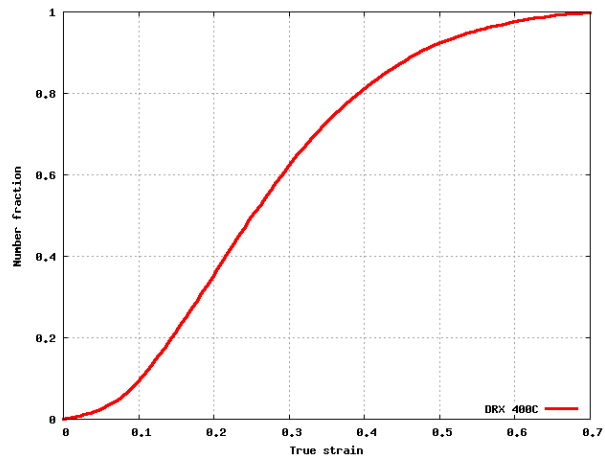
(b)

Figure 6.28: Evolution of the volume fraction of DRX (a) 300°C (b) 400°C.

81
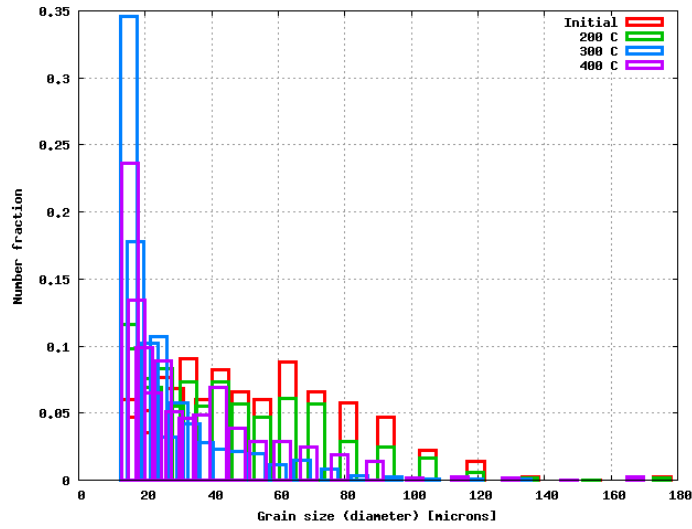
Figure 6.29: The histogram of the grain size distribution: initial and final after DRX at three simulated temperatures.

value for extension twins is not constant at elevated temperatures, and further study in this field is needed.
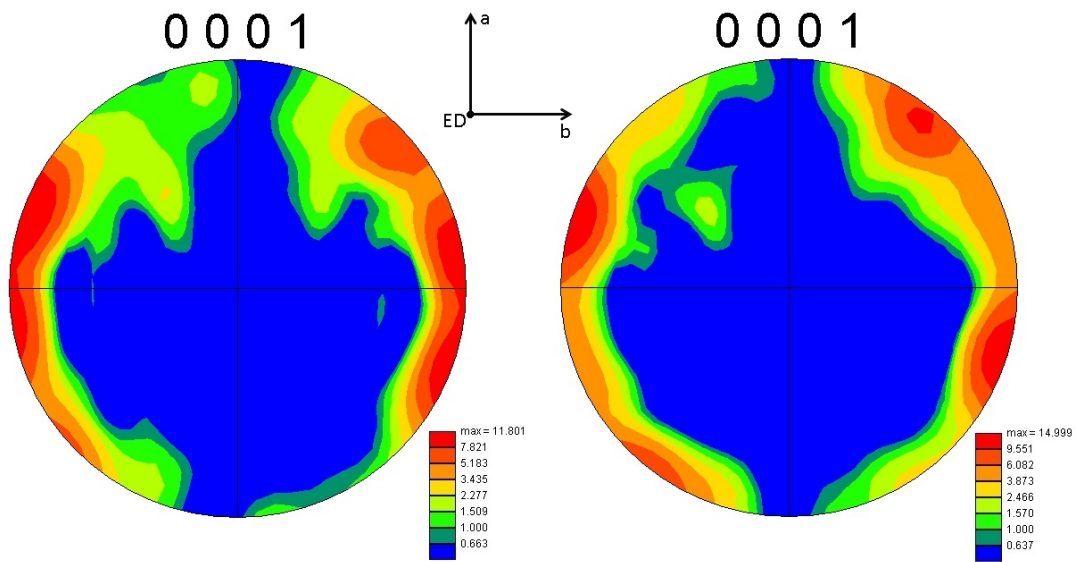
Figure 6.30: Final {0001} pole figures after DRX at (a) 300°C (b) 400°C.

6.2.4 Conclusions

The effect of the extension twinning on dynamic recrystallization in magnesium alloy AZ31 was investigated using the DRX-CPFE model. The compression test along the extrusion direction (ED) is simulated at various temperatures with the $10^{-4}s^{-1}$ strain rate. The following conclusions have been made:

- Since the CRSS values for slip systems are much lower at the elevated temperatures, extension twinning is not active at temperatures higher than 300°C.

- The study of slip system activity shows that during compression along the ED of the extruded AZ31 alloy, the majority of plastic deformation is accommodated by prismatic, basal and pyramidal $\langle c + a \rangle$ slip systems. Pyramidal $\langle c + a \rangle$ slip systems are known to be activated at elevated temperatures. As temperature rises, the CRSS value for pyramidal $\langle c+a \rangle$ slip decreases, and it overtakes the strain accommodation.

- At 200°C twinning still has a big impact on the texture evolution. Most of the grains were reoriented into twin orientation, which can be seen from the final pole figures. The experimental data suggests that most of the grains underwent twinning at 200°C, and the simulations showed that 70% of the grains have been twinned.

- The simulations at 300°C and 400°C have not revealed the active twinning, and the deformation was dominated by prismatic and pyramidal $\langle c + a \rangle$ slip. However, the predicted pole figures at 300°C does not match with the experimental pole figures. These results suggest that the CRSS value for extension twins might not be constant at elevated temperatures, and further study in this field is needed.

Chapter 7

Effect Of The Model Parameters On DRX

The proposed model contains various parameters, which are calibrated to fit the experimental stress-strain curve. The effect of the model parameters on the nucleation sites and the growth rate will be studied in this chapter. In Fig.7.1 a schematic of the areas in the stress-strain curve during DRX is presented. The stress-strain is divided into five sections: the first one represents the curve up to yielding, the second - hardening before DRX initiation due to slip and twinning, the third - peak stress, when DRX starts, the fourth - softening in the flow curve, and finally, the fifth is the final microstructure and texture formation after DRX. The parameters, which have an influence on each of the aforementioned sections, are summarized in Table 7.1.

7.1 Critical conditions for the DRX initiation and nucleation

In the critical condition for the DRX initiation (Eqn.5.22) S represents the grain boundary energy per unit area, M is the grain boundary mobility, τ $(c\mu b^2)$ is the dislocation line energy and L is the dislocation mean free path, $(L = K/c_2\sqrt{\rho})$, the constants K, c are of the order 10 and 0.5 respectively. The effect of parameters such as K, c_2, c on the DRX behaviour will be studied. This criterion was developed by Roberts and Ahlblom [132] for the pre-existing grain boundary bulging mechanism, and it was used as a nucleation criterion for numerous DRX/SRX models. However, in the current model this criterion is
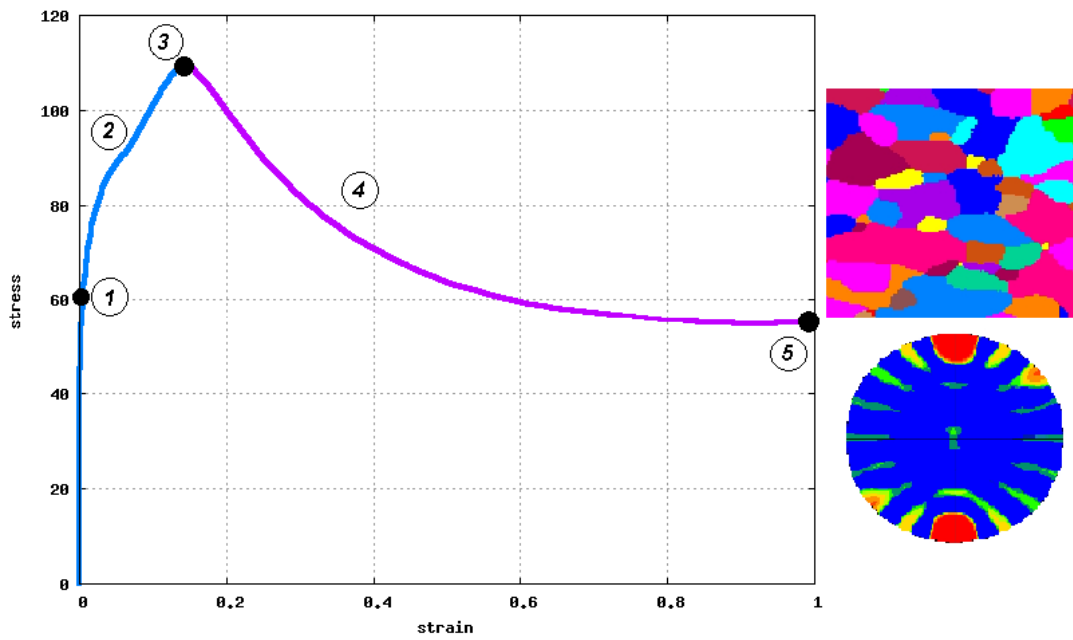
Figure 7.1: Schematic of the influence of the model parameters on different regions of a flow curve

Table 7.1: Temperature dependent parameters of the model and their influence on the DRX evolution based on Fig.7.1.

Parameter	1	2	3	4	5
CRSS	√	√			
ρ_{cr}			√	√	
$d\rho_{cr}$				√	√
M				√	√
Δt_{DRX}			√	√	

used as a criterion for the onset of DRX to determine the critical value of the dislocation density before it can be a potential nucleation site.

Another parameter that should be studied is the threshold value for the nucleation criterion. The nucleation criterion states that if $\theta \geq \theta_{cr}$ and $d\rho \geq d\rho_{cr}$ for the current element, then the site is identified as a potential nucleus. From these, viable nuclei are chosen with a probability depending on the stored energy difference and the grain boundary mobility.

The first threshold value is the critical misorientation angle, θ_{cr}, picked to define high angle grain boundaries. The value of $15°$ degrees is accepted in the literature [7], and therefore, this values also used in the simulations.

The threshold value $d\rho_{cr}$ controls the amount of nuclei over the structure. If a low value is picked then more potential nucleation sites will be defined. It also affects the number of nuclei, which occur during the later stages of DRX. The value of $d\rho_{cr}$ in the simulations evolves during the deformation, and it is calculated based on the current maximum dislocation density value, ρ_{max}, which occurs over the domain at the current simulation time step, as follows:

$$d\rho_{cr} = C_0 \rho_{max} \tag{7.1}$$

Since the dislocation density in the non-recrystallized structure grows during the deformation, it is important to take into account the current state of the dislocation density in the nucleation criterion. The factor C_0 is chosen to control the amount of the nuclei that will grow. The simulation results show that this parameter has significant effect on the recrystallization texture. Therefore, the effect of the critical value in dislocation density mismatch is investigated.

C_0	0.2	0.4	0.6	0.5	0.5	0.5	0.6	0.3
c_2	0.01	0.01	0.01	0.01	0.1	1.0	0.001	0.1

Table 7.2: Variation of the parameters considered in the study

First, the $d\rho_{cr}$ value is kept constant, and the simulations are performed for various ρ_{cr} to study its effect on the results. The results obtained from the simulations are presented in Fig. 7.2 and Fig. 7.3. The pole figures (Fig. 7.2) show that ρ_{cr} does not have a significant effect on the final DRX texture. However, the first peak of the stress-strain curve is controlled by this parameter. As it was shown before, with increasing the temperature, the peak stress shifts down, and therefore, the ρ_{cr} value should be lowered as well.

The evolution of the volume fraction of the recrystallized elements (Fig.7.4) demonstrates that the recrystallization rate is not changed significantly, however, the final fraction

86
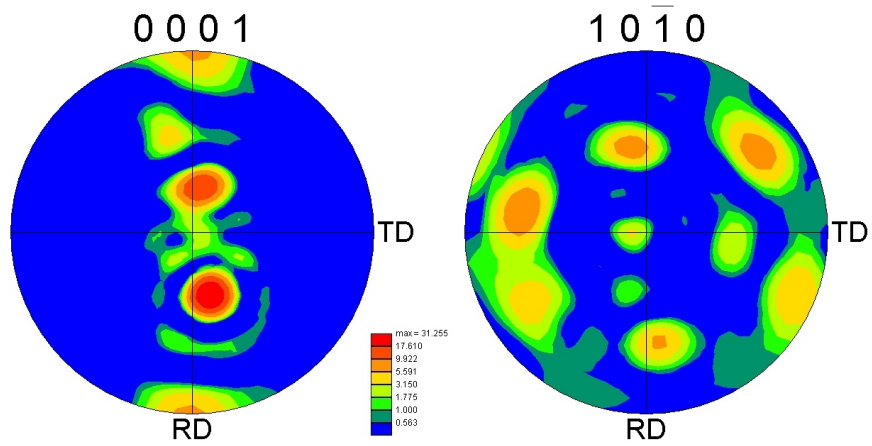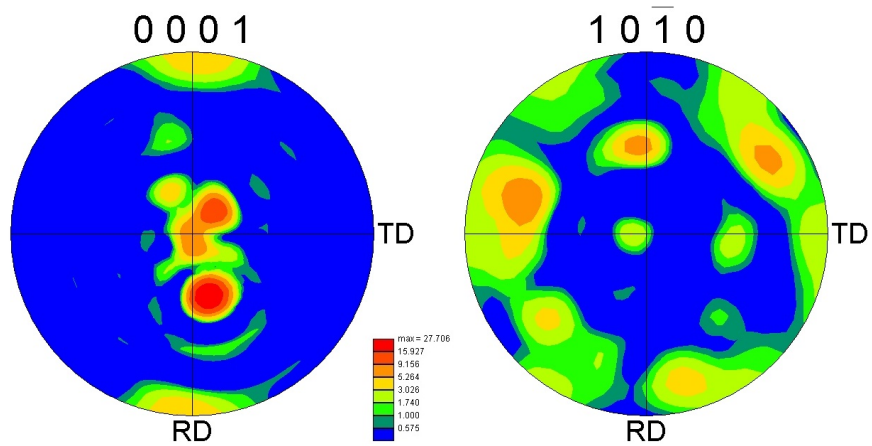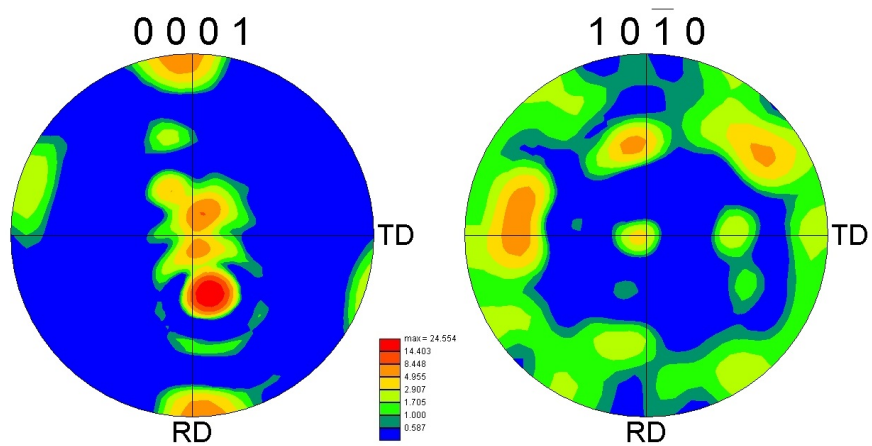
Figure 7.2: Final DRX pole figures for the different values of c_2 in the ρ_{cr}

of the recrystallized elements varies from 0.6 to 0.85.
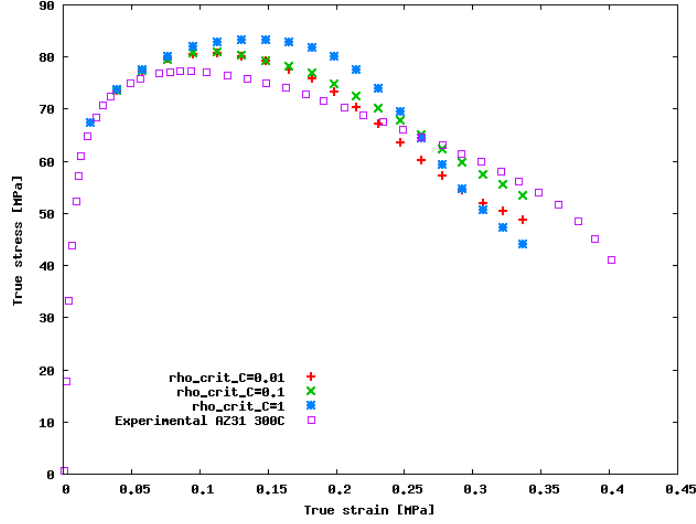
Figure 7.3: Stress-strain curves for different values of c_2 ($d\rho_{cr} = const$).
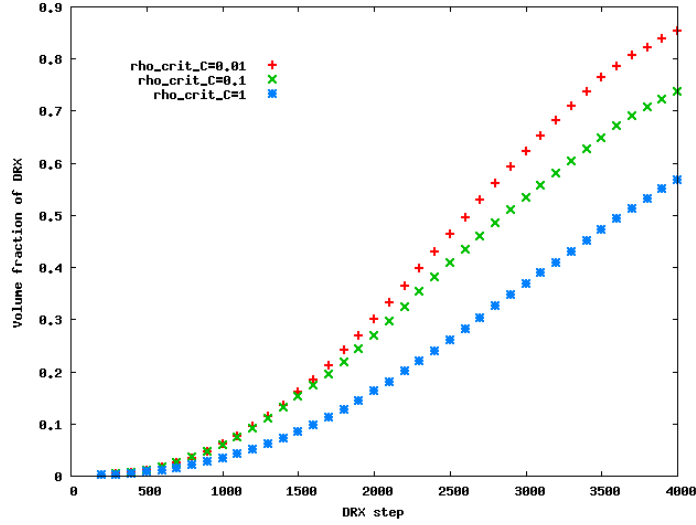
Figure 7.4: Volume fraction of recrystallized elements for different values of c_2 ($d\rho_{cr} = const$).

The next simulations are performed for different values of C_0 in the critical condition based on the dislocation density mismatch (eq. 7.1). The values for the ρ_{cr} is kept constant

during these simulations. The results are presented in Fig. 7.5. EBSD IPF maps illustrate the final microstructure after the DRX. It can be seen that for the lower threshold value the amount of the viable nucleation sites increases, and it leads to the fully recrystallized structure (Fig. 7.5a). The new nuclei replaced the matrix grains developing different texture than in the latter two cases. The final pole figures are given in Fig. 7.7. They indicate that the critical value for the nucleation condition has the stronger effect on the texture formation compared to the ρ_{cr} value. Furthermore, the critical condition, $d\rho_{cr}$, influences the rate of the recrystallization (Fig. 7.6). The results suggest that the magnitude of the critical value can be related to the temperature of the deformation. It is reported in literature that at higher temperatures the fully recrystallized samples are observed, whereas the lower temperature DRX leads a lower fraction of recrystallized grains [23].

7.2 Effect of the grain boundary mobility on texture evolution

The mobility of the grain boundary is a function of the temperature and misorientation that should be measured experimentally. The general shape of the mobility curve is given in the monograph by Humphreys and Hatherly [7]. For FCC metals the data can be found in the literature, however, for HCP metals such as magnesium experimental observations are not available in the literature. Therefore, in this work, the step function is used to incorporate the mobility curve in the model. Due to this, the effect of the mobility function should be studied within the model. Assigning different mobility values to the different grain boundaries should effect the location of the nucleation sites as well as their consequent growth since the switching rule is based on the velocity of the grain boundary, which is calculated depending on its mobility (eqn.5.26).

The twinned elements provide a high misorientation angle, and hence, higher mobility for those boundaries. Therefore, the twinned elements are favorable sites for the potential nuclei. In order to study the effect of the mobility function, another curve is chosen to be the one peak function as presented in Fig. 7.8b.

The results of the simulations for both types of the mobility are shown in Fig.7.9. The crops of the same area of the full microstructure demonstrate the effect of the mobility function. The indicated areas are the twins with 86 degrees of misorientation. For the first case, twins have a high mobility, and therefore, they are recrystallized during the deformation. However, the second case shows that twins are left unrecrystallized due to the lower mobility.
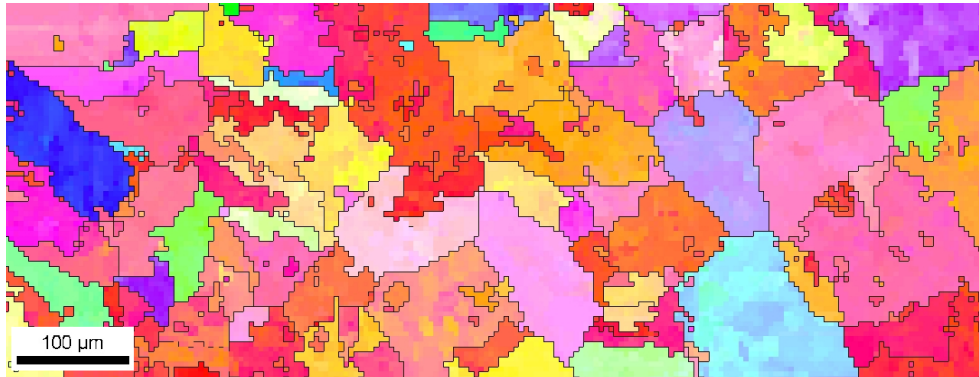
(a)
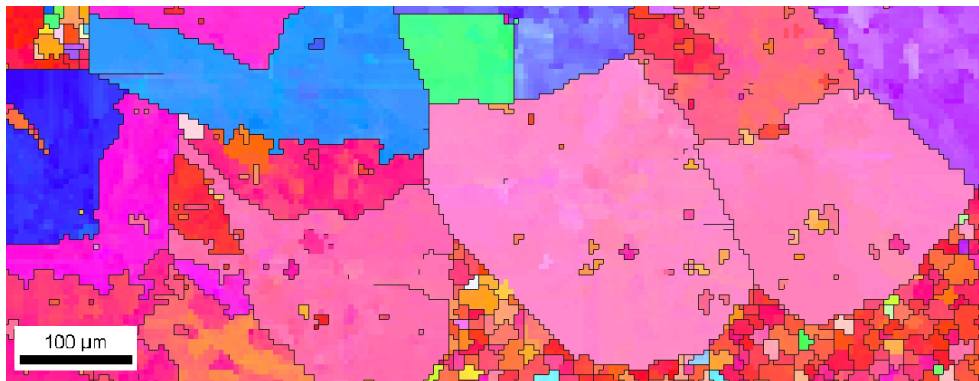
(b)
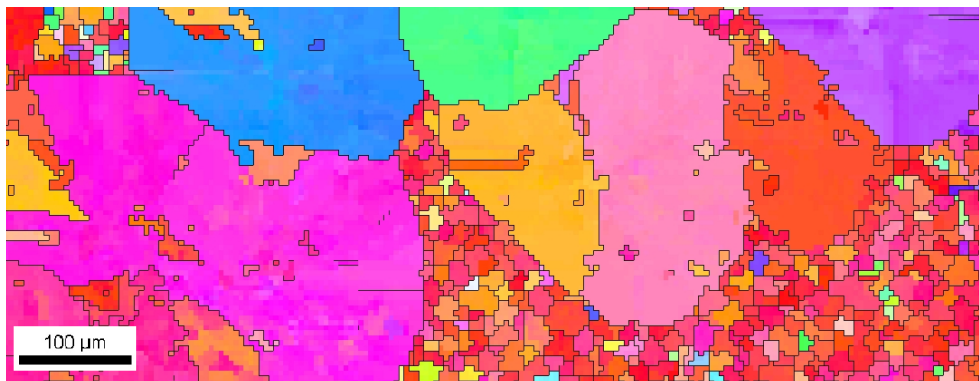
(c)

Figure 7.5: Final EBSD IPF maps after DRX for the different values of C_0 in the $d\rho_{cr}$.
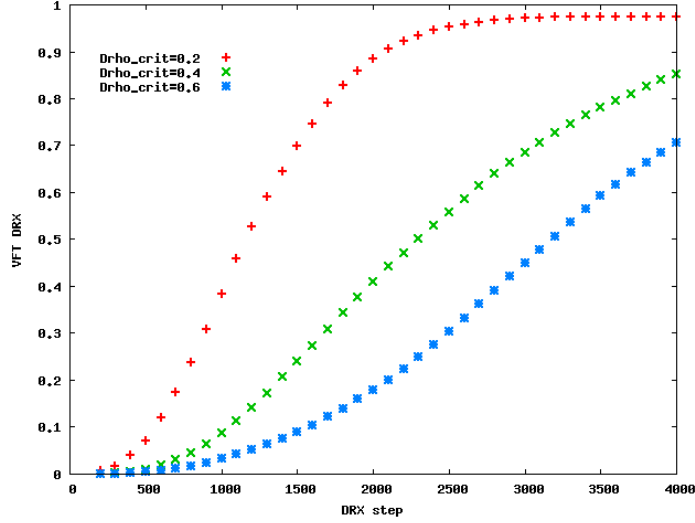
Figure 7.6: Volume fraction of recrystallized elements during the simulations for the different values of C_0 in the $d\rho_{cr}$.

In the experimental works of [23], the authors observed extension twins without recrystallization at the end of the test. The reason why twins were left unrecrystallized was unknown. However, the simulation results show that if the mobility function had the one-peak shape, the twin boundaries are less mobile, and hence, twins might not become the nuclei for DRX. Another possible explanation for this is that the twins might have a lower dislocation content than the matrix grain, and therefore, the dislocation density does not reach the critical value to become DRX nuclei.

7.3 Conclusions

The following conclusions can be drawn from the present study of the model parameters:

- The critical condition for DRX initiation, ρ_{cr}, does not effect the texture evolution, however, it controls the first peak in the stress-strain curve. This parameters is responsible for early or late initiation of DRX, which depends on the deformation temperature. At the higher temperatures, DRX is known to start earlier than at the lower temperatures.

- The critical condition for DRX nucleation based on the local mismatch in dislocation density, $d\rho_{cr}$, has a significant influence on the final recrystallized texture and recrys-

91

0 0 0 1   1 0 1̄ 0

(a)

0 0 0 1   1 0 1̄ 0

(b)

0 0 0 1   1 0 1̄ 0
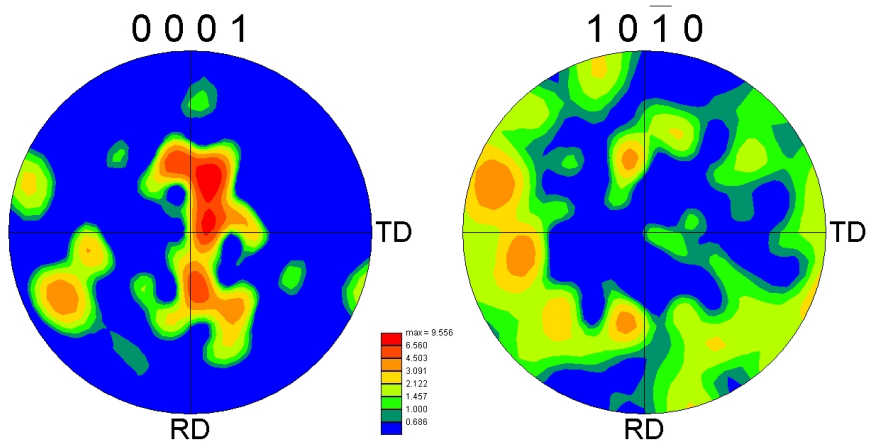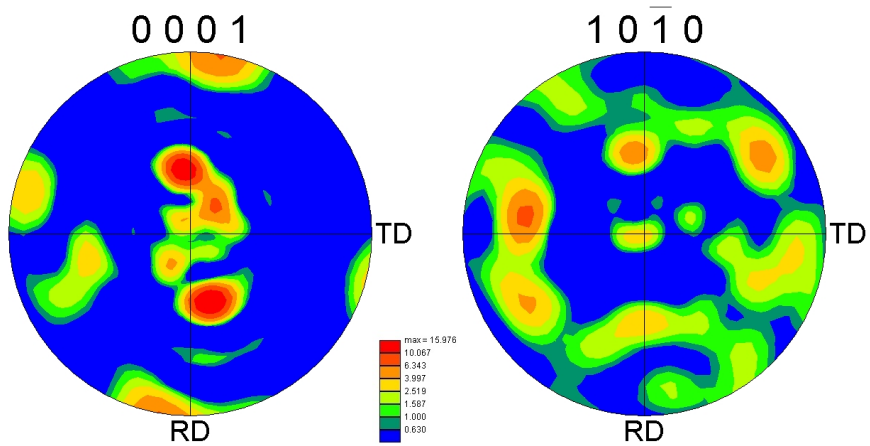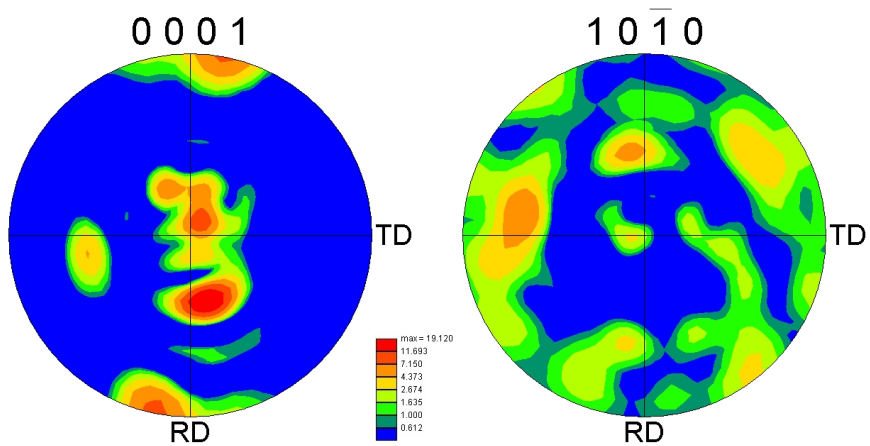
(c)

Figure 7.7: Final DRX pole figures for the different values of C_0 in the $d\rho_{cr}$.
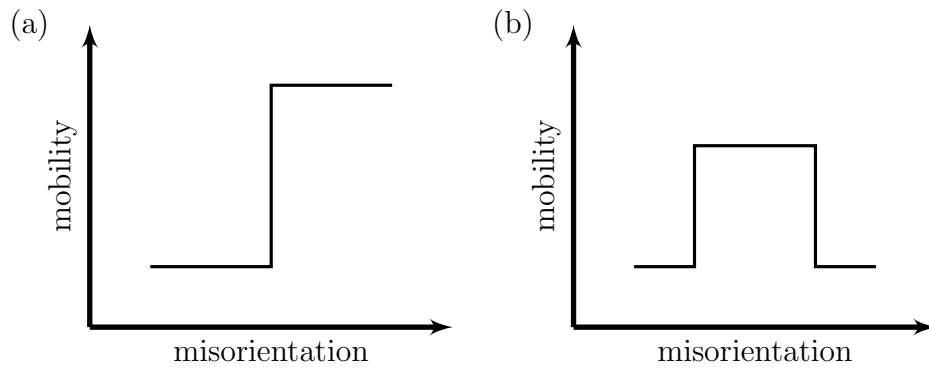
Figure 7.8: Schematic of mobility functions used in the study (a) step function; (b) one peak function.

Figure 7.9: Crops from the final full EBSD samples after simulations with different mobility functions (a) step function (b) one peak function

tallization rate. The lower the chosen magnitude, the more potential nucleation sites will be generated. Therefore, this parameter is responsible for the number of nuclei, and consequently, the final grain size.

- The mobility function for magnesium alloy might follow the one peak function at the temperatures when twinning is active.

Chapter 8

Summary and Conclusions

The proposed combined CPFEM-CA model is capable of predicting the mechanical response of the material as well as its microstructure evolution synchronously. This model has an advantage over other methods that use a phenomenological approach to obtain either the stress state or the DRX. The simulation results at elevated temperatures, where DRX occurs, show a good agreement with published experimental data. The softening behaviour of the DRX flow curve is predicted without phenomenological representation, and additionally, microstructure development during grain growth is captured satisfactorily. The final microstructure is in excellent correspondence with published microstructural observations. The major conclusions of the work are as follows:

- A new model for dynamic recrystallization is developed by coupling the crystal plasticity finite element method with probabilistic cellular automata. Even though this new approach is applied to HCP metals, magnesium alloys in particular, the numerical framework can easily be applied to other metals. The model uses microstructure data collected by EBSD as input. The state variables are extracted from the crystal plasticity simulation, and used in the CA model, where the cells are represented by finite elements.

- A new nucleation criterion based on the mismatch in dislocation density between neighbouring elements is implemented in the model. The grain boundaries with high disorientation and high local mismatch ("jump") in dislocation density are considered to be the potential nucleation sites. This nucleation criterion satisfies the mechanical instability, which is based on the inhomogeneous distribution of the dislocation density.

- Recrystallization occurs by nucleation and subsequent growth of viable nuclei defined by the probability switching rule depending on the grain boundary velocity. The threshold value for the dislocation mismatch controls the amount of potential nucleation sites, while the critical condition for the onset of DRX is set to fit the first peak of the flow curve.

- The capability of the model is demonstrated by simulating tensile and compressive loading, when different deformation mechanisms are active in magnesium alloys. The stress-strain curves and final pole figures show a good match with experimental data.

- Deformation twinning has a significant effect on the texture evolution at 200°C. The stress-strain curve also indicates an active deformation twinning during 200°C compression. However, at the temperatures 300°C and 400°C, twinning is not active because the CRSS for other slip systems becomes lower than twin CRSS. The results indicate that non-basal slip systems take over the deformation at elevated temperatures.

- Attempts were made to find the correlation between CRSS values and the temperature. The simulation results suggest that the correlation between CRSS values and temperature (between 200°C and 400°C)is not linear, when twinning is active. However, the CRSS for twins seems to be not constant as it was assumed in the previous studies.

- The study of the grain boundary mobility suggests that the mobility function for the extruded Mg alloy might have one peak shape at 200°C. The high angle boundaries (> 80) can be less mobile compared to the middle angles, which can leave some twins unrecrystallized after DRX.

- The effect of the model parameters on DRX evolution and texture formation is studied. The nucleation criterion threshold has an impact to the final DRX texture, as well as the nuclei amount, while the critical condition for the DRX initiation influences the first peak of the stress-strain curve and further nucleation site formations.

Chapter 9

Future Work

In this chapter the recommendations are given regarding a future work for the extension of the model:

- the second cycle of recrystallization;

- particle stimulated nucleation (PSN);

- random new orientation nucleation;

The second cycle of recrystallization

During primary recrystallization, material can undergo a few cycles of recrystallization [150, 151]. The proposed model takes into account only the first cycle, and therefore, the element (cell) can be recrystallized only once. In the future work, the second cycle can be included in the model. In order to do so, the condition whether recrystallization and nucleation variables are zero ($N = 0$ and $R = 0$) in the DRX block should be skipped, so any element can be recrystallized second time.

The general behaviour of the DRX volume fraction for a few cycles is given in the work of Brown and Bammann [126]. Although it is represented by the phenomenological expression, each curve has a JMAK (chapter 3) type behaviour.

The major challenge in this approach is to determine the initiation of the second cycle of DRX. In literature, the critical strain for the second and subsequent DRX cycles is assumed to be smaller than for the initial one [150]. In the proposed model, the critical condition for DRX initiation is based on the dislocation content in the grain and its high

mismatch between the neighbouring grains. Therefore, the critical condition is needed for the subsequent cycles of DRX.

The assumption that the cell (element) can be recrystallized once is no longer needed. However, once the growing grains impinge each other, the further grain boundary movement is suppressed.

A new variable should be introduced for the second cycle of recrystallization. New nuclei are allowed to appear if the dislocation density is high enough no satisfy the critical condition. Dislocation density is set to a low value (10^{-8}), once the element is recrystallized. However, during further deformation, those recrystallized elements still undergo plastic deformation and accumulate dislocations. But the dislocation density will most likely never reach the same critical amount of dislocations needed to become a feasible nucleation site. Therefore, another critical condition is required separately for the second cycle of DRX.

Particle stimulated nucleation (PSN) Particles are known to provide a nucleation site for recrystallization and grow a new nuclei [8]. PSN provides a good tool to attain a random texture after DRX, which leads to the next recommendation.

Random new orientation nuclei In order to attain a randomized texture after DRX, a new nucleation orientation has to be created. One approach as to how to choose a new orientation was proposed by Raabe et al. [112]. A new grain orientation was calculated based on the middle orientation between the neighbouring grains.

Appendix

The flow chart of the DRX model is presented in this Appendix.
All the **NO** response lead to **EXIT TO THE NEXT ELEMENT**.

CPFEM
Deformation
Gradient $F=F*Fp$
$$\gamma_a = \int_0^t \sum_{\alpha=1}^{N^s} |\gamma_{(\alpha)}|\,dt$$

DRX BLOCK

ELEMENT i

$R(i)=0$
$N(i)=0$

EXIT TO THE NEXT ELEMENT

NO

YES

Calculate dislocation density
$$\varrho_{GN(s)}^{\alpha} b = \mathbb{V}^{\alpha} \quad \mathbf{n}^{\alpha} = \gamma_{,k}^{\alpha} \mathbf{n}_k^{\alpha}$$
$$\varrho_{GN(e)}^{\alpha} b = -\mathbb{V}^{\alpha} \quad \mathbf{m}^{\alpha} = -\gamma_{,k}^{\alpha} \mathbf{s}_k^{\alpha}$$

Calculate misorientation angle
$$\Theta = min\left[cos^{-1}\left(\frac{tr(\Omega_i \Omega_j^T)-1}{2} \right) \right]$$

Nucleation
step or
Growth step

Nucleation Step

$\Theta \geq \Theta_{cr}$

YES

Calculate
$$\varrho_{cr} = \left(\frac{20 S \varepsilon}{3 b L M \tau^2} \right)^{1/3}$$

$\rho \geq \rho_{cr}$

YES

Calculate
$$d|\alpha| = ||\alpha_i| - |\alpha_j||$$

$d\alpha \geq d\alpha_{cr}$

YES

Calculate velocity of the element
$V = MP$

Growth Step

Calculate velocity of the element
$V = MP$

Cellular Automata

$R(j)=1$ or
$N(j)=1$

YES

Monte-Carlo Step

Calculate switching parameter
$$\omega_{switch} = \frac{v_i^j}{v_{max}}$$
Generate random number $\xi \notin 0,1]$

$\xi \leq \omega_{switch}$

YES

$$\Omega_i = \Omega_j$$
$$R(i)=1$$
$$\rho = 10e\text{-}8$$
$$\sigma = a \mu b^2 \sqrt{\varrho}$$

YES

Nucleus!
$N(i)=1$

Exit to the next element

References

[1] Key to Metals AG. Automotive uses of magnesium alloys: Part one. http://www.keytometals.com, Jul 2010.

[2] Charlie R Brooks. *Heat treatment, structure, and properties of nonferrous alloys.* American Society for metals, 1982.

[3] Manesium Elektron. Magnesium in automotive. http://www.magnesium-elektron.com, 2014.

[4] M. Gupta and N.M.L. Sharon. *Magnesium, magnesium alloys, and magnesium composites.* John Wiley & Sons, 2011.

[5] L. L. Rokhlin. *Magnesium alloys containing rare earth metals: structure and properties.* Crc Press, 2003.

[6] B. L. Adams, S. R. Kalidindi, and D. T. Fullwood. *Microstructure sensitive design for performance optimization.* Butterworth-Heinemann, 2012.

[7] F. J. Humphreys and M. Hatherly. *Recrystallization and related annealing phenomena*, volume 416. Elsevier Oxford, 2004.

[8] R.D. Doherty, D.A. Hughes, F.J. Humphreys, J.J. Jonas, D.Juul Jensen, M.E. Kassner, W.E. King, T.R. McNelley, H.J. McQueen, and A.D. Rollett. Current issues in recrystallization: a review. *Materials Science and Engineering: A*, 238(2):219 – 274, 1997.

[9] S.B. Yi, S. Zaefferer, and H.-G. Brokmeier. Mechanical behaviour and microstructural evolution of magnesium alloy az31 in tension at different temperatures. *Materials Science and Engineering: A*, 424(1):275 – 281, 2006.

[10] A. Galiyev, R. Kaibyshev, and G. Gottstein. Correlation of plastic deformation and dynamic recrystallization in magnesium alloy zk60. *Acta Materialia*, 49(7):1199 – 1207, 2001.

[11] F. Roters, P. Eisenlohr, L. Hantcherli, D.D. Tjahjanto, T.R. Bieler, and D. Raabe. Overview of constitutive laws, kinematics, homogenization and multiscale methods in crystal plasticity finite-element modeling: Theory, experiments, applications. *Acta Materialia*, 58(4):1152 – 1211, 2010.

[12] S. R. Kalidindi. Incorporation of deformation twinning in crystal plasticity models. *Journal of the Mechanics and Physics of Solids*, 46(2):267 – 290, 1998.

[13] J. Levesque, K. Inal, K.W. Neale, and R.K. Mishra. Numerical modeling of formability of extruded magnesium alloy tubes. *International Journal of Plasticity*, 26(1):65 – 83, 2010.

[14] A. Izadbakhsh, K. Inal, R. K. Mishra, and M. Niewczas. New crystal plasticity constitutive model for large strain deformation in single crystals of magnesium. *Computational Materials Science*, 50(7):2185 – 2202, 2011.

[15] P.G. Partridge. The crystallography and deformation modes of hexagonal close-packed metals. *International Materials Reviews*, 12(1):169–194, 1967.

[16] Inc. Encyclopaedia Britannica. Encyclopaedia britannica. http://www.britannica.com/EBchecked/media/1527/The-commonest-metallic-crystal-structures, 2011.

[17] M. Niewczas. Lattice correspondence during twinning in hexagonal close-packed crystals. *Acta Materialia*, 58(17):5848 – 5857, 2010.

[18] W. F. Hosford. *The mechanics of crystals and textured polycrystals.* Oxford University Press(USA), 1993.

[19] M. Hatherley and W. B. Hutchinson. An introduction to textures in metals. *Institution of Metallurgists, 1979,*, page 76, 1979.

[20] W. F. Hosford. *Materials science: an intermediate text.* Cambridge University Press, 2006.

[21] P. Cotterill and P. R Mould. *Recrystallization and grain growth in metals*, volume 266. Surrey University Press London, 1976.

[22] G. Gottstein. Physical foundations of materials science. *Heidelberg, Springer-Verlag Berlin Heidelberg, 2004.*, pages 1–502, 2004.

[23] T. Al-Samman and G. Gottstein. Dynamic recrystallization during high temperature deformation of magnesium. *Materials Science and Engineering: A*, 490(1):411 – 420, 2008.

[24] J. Dennis, P.S. Bate, and F.J. Humphreys. Abnormal grain growth in al–3.5 cu. *Acta materialia*, 57(15):4539–4547, 2009.

[25] G. Sachs. Plasticity problems in metals. *Transactions of the Faraday Society*, 24:84–92, 1928.

[26] G. I. Taylor. The mechanism of plastic deformation of crystals. part i. theoretical. *Proceedings of the Royal Society of London. Series A, Containing Papers of a Mathematical and Physical Character*, pages 362–387, 1934.

[27] C.N. Tome', R.A. Lebensohn, and U.F. Kocks. A model for texture development dominated by deformation twinning: Application to zirconium alloys. *Acta Metallurgica et Materialia*, 39(11):2667 – 2680, 1991.

[28] R.A. Lebensohn and C.N. Tomé. A self-consistent anisotropic approach for the simulation of plastic deformation and texture development of polycrystals: application to zirconium alloys. *Acta Metallurgica et Materialia*, 41(9):2611–2624, 1993.

[29] D. Raabe and F. Roters. Using texture components in crystal plasticity finite element simulations. *International Journal of Plasticity*, 20(3):339–361, 2004.

[30] K. Inal, P.D. Wu, and K.W. Neale. Finite element analysis of localization in fcc polycrystalline sheets under plane stress tension. *International Journal of Solids and Structures*, 39(13):3469–3486, 2002.

[31] D P Mika and P R Dawson. Effects of grain interaction on deformation in polycrystals. *Materials Science and Engineering: A*, 257(1):62–76, 1998.

[32] A. Ma, F. Roters, and D. Raabe. A dislocation density based constitutive model for crystal plasticity fem including geometrically necessary dislocations. *Acta Materialia*, 54(8):2169–2179, 2006.

[33] A. Izadbakhsh, K. Inal, and R. K. Mishra. Numerical formability assessment in single crystals of magnesium. *Computational Materials Science*, 50(2):571 – 585, 2010.

[34] A Staroselsky and L Anand. Inelastic deformation of polycrystalline face centered cubic materials by slip and twinning. *Journal of the Mechanics and Physics of Solids*, 46(4):671–696, 1998.

[35] A Staroselsky and L Anand. A constitutive model for hcp materials deforming by slip and twinning: application to magnesium alloy az31b. *International Journal of Plasticity*, 19(10):1843–1864, 2003.

[36] P. Van Houtte. Simulation of the rolling and shear texture of brass by the taylor theory adapted for mechanical twinning. *Acta Metallurgica*, 26(4):591 – 604, 1978.

[37] S.E. Ion, F.J. Humphreys, and S.H. White. Dynamic recrystallisation and the development of microstructure during the high temperature deformation of magnesium. *Acta Metallurgica*, 30(10):1909 – 1919, 1982.

[38] C. Bettles and M.R. Barnett. *Advances in wrought magnesium alloys: Fundamentals of processing, properties and applications*. Elsevier, 2012.

[39] T.Al-Samman. *Magnesium The Role of Crystallographic Texture, Deformation Conditions and Alloying Elements on Formability*. PhD thesis, Rheinisch-Westflischen Technischen Hochschule Aachen, 2008.

[40] A. S. Khan, A. Pandey, T. Gnäupel-Herold, and R. K Mishra. Mechanical response and texture evolution of az31 alloy at large strains for different strain rates and temperatures. *International Journal of Plasticity*, 27(5):688–706, 2011.

[41] A. Jain and S.R. Agnew. Modeling the temperature dependent effect of twinning on the behavior of magnesium alloy az31b sheet. *Materials Science and Engineering: A*, 462(1):29–36, 2007.

[42] M.R. Barnett. A taylor model based description of the proof stress of magnesium az31 during hot working. *Metallurgical and materials transactions A*, 34(9):1799–1806, 2003.

[43] M.M Myshlyaev, H.J. McQueen, A. Mwembela, and E. Konopleva. Twinning, dynamic recovery and recrystallization in hot worked mg–al–zn alloy. *Materials Science and Engineering: A*, 337(1):121–133, 2002.

[44] B. Srinivasarao, N.V. Dudamell, and M.T. Pérez-Prado. Texture analysis of the effect of non-basal slip systems on the dynamic recrystallization of the mg alloy az31. *Materials Characterization*, 2012.

103

[45] N. Li, G. Huang, R. Xin, and Q. Liu. Effect of initial texture on dynamic recrystallization and deformation mechanisms in az31 mg alloy extruded at 573k. *Materials Science and Engineering: A*, 569(0):18 – 26, 2013.

[46] Maoyin Wang, Renlong Xin, Bingshu Wang, and Qing Liu. Effect of initial texture on dynamic recrystallization of az31 mg alloy during hot rolling. *Materials Science and Engineering: A*, 528(6):2941 – 2951, 2011.

[47] M.R Barnett. Influence of deformation conditions and texture on the high temperature flow stress of magnesium az31. *Journal of Light Metals*, 1(3):167 – 177, 2001.

[48] N.V. Dudamell, I. Ulacia, F. Galvez, S. Yi, J. Bohlen, D. Letzig, I. Hurtado, and M.T. Perez-Prado. Influence of texture on the recrystallization mechanisms in an az31 mg sheet alloy at dynamic rates. *Materials Science and Engineering: A*, 532(0):528 – 535, 2012.

[49] B. Srinivasarao, N.V. Dudamell, and M.T. Perez-Prado. Texture analysis of the effect of non-basal slip systems on the dynamic recrystallization of the mg alloy az31. *Materials Characterization*, 75(0):101 – 107, 2013.

[50] É. Martin, R. K Mishra, and J. J Jonas. Effect of twinning on recrystallisation textures in deformed magnesium alloy az31. *Philosophical Magazine*, 91(27):3613–3626, 2011.

[51] Q. Ma, B. Li, E.B. Marin, and S.J. Horstemeyer. Twinning-induced dynamic recrystallization in a magnesium alloy extruded at 450 c. *Scripta Materialia*, 65(9):823–826, 2011.

[52] J.R. Morris, K.M. Ho, K.Y. Chen, G. Rengarajan, and M.H. Yoo. Large-scale atomistic study of core structures and energetics of (c+a) dislocations in hexagonal close packed metals. *Modelling and Simulation in Materials Science and Engineering*, 8(1):25, 2000.

[53] Q. Ma, B. Li, W.R. Whittington, A.L. Oppedal, P.T. Wang, and M.F. Horstemeyer. Texture evolution during dynamic recrystallization in a magnesium alloy at 450 c. *Acta Materialia*, 67:102–115, 2014.

[54] D. Kuc, E. Hadasik, G. Niewielski, and A. Płachta. Structure and plasticity of the az31 magnesium alloy after hot deformation. *Journal of Achievements in Materials and Manufacturing Engineering*, 27(1):27–30, 2008.

[55] O. Sitdikov and R. Kaibyshev. Dynamic recrystallization in pure magnesium. *Materials Transactions(Japan)*, 42(9):1928–1937, 2001.

[56] T. Al-Samman, X. Li, and S G. Chowdhury. Orientation dependent slip and twinning during compression and tension of strongly textured magnesium az31 alloy. *Materials Science and Engineering: A*, 527(15):3450–3463, 2010.

[57] G. Gottstein and T. Al-Samman. Texture development in pure mg and mg alloy az31. In *Materials Science Forum*, volume 495, pages 623–632. Trans Tech Publ, 2005.

[58] R. Gehrmann, M. M Frommert, and G. Gottstein. Texture effects on plastic deformation of magnesium. *Materials Science and Engineering: A*, 395(1):338–349, 2005.

[59] T. Al-Samman, K. D. Molodov, D. A. Molodov, G. Gottstein, and S. Suwas. Softening and dynamic recrystallization in magnesium single crystals during c-axis compression. *Acta Materialia*, 60(2):537 – 545, 2012.

[60] E.W. Kelley and W.F. Hosford. The deformation characteristics of textured magnesium. *Trans Met Sos AIME*, 242(4), 1968.

[61] E.W. Kelley and W.F. Hosford. Plane-strain compression of magnesium and magnesium alloy crystals. *Trans Met Soc AIME*, 242(1):5–13, 1968.

[62] B.C Wonsiewicz and W.A Backofen. Independent slip systems and ductility of hexagonal polycrystals. *Transaction of Metallurgical Soc. AIME*, 239:1422–1433, 1967.

[63] Yi Liu and Xin Wu. An electron-backscattered diffraction study of the texture evolution in a coarse-grained az31 magnesium alloy deformed in tension at elevated temperatures. *Metallurgical and Materials Transactions A*, 37(1):7–17, 2006.

[64] Nali Li, Guangjie Huang, Xiaoyu Zhong, and Qing Liu. Deformation mechanisms and dynamic recrystallization of az31 mg alloy with different initial textures during hot tension. *Materials & Design*, 2013.

[65] L. Jiang, J. J. Jonas, A. A. Luo, A. K. Sachdev, and S. Godet. Twinning-induced softening in polycrystalline am30 mg alloy at moderate temperatures. *Scripta Materialia*, 54(5):771 – 775, 2006.

[66] T. Al-Samman. Modification of texture and microstructure of magnesium alloy extrusions by particle-stimulated recrystallization. *Materials Science and Engineering: A*, 560(0):561 – 566, 2013.

105

[67] A. Galiyev and R. Kaibyshev. Superplasticity in a magnesium alloy subjected to isothermal rolling. *Scripta Materialia*, 51(2):89 – 93, 2004.

[68] H. Hallberg. Approaches to modeling of recrystallization. *Metals*, 1(1):16–48, 2011.

[69] A.D. Rollett. Overview of modeling and simulation of recrystallization. *Progress in Materials Science*, 42(1):79 – 99, 1997.

[70] W. A. Johnson and R. F. Mehl. Reaction kinetics in processes of nucleation and growth. *Trans. Aime*, 135(8):396–415, 1939.

[71] M. Avrami. Kinetics of phase change. i general theory. *The Journal of Chemical Physics*, 7:1103, 1939.

[72] A. N. Kolmogorov. On the statistical theory of the crystallization of metals. *Bull. Acad. Sci. USSR, Math. Ser*, 1:355–359, 1937.

[73] R. Sandstttröm. Subgrain growth occurring by boundary migration. *Acta Metallurgica*, 25(8):905–911, 1977.

[74] T. Furu, R. Ørsund, and E. Nes. Subgrain growth in heavily deformed aluminiumexperimental investigation and modelling treatment. *Acta metallurgica et materialia*, 43(6):2209–2232, 1995.

[75] R. Sandstrom and R. Lagneborg. A model for hot working occurring by recrystallization. *Acta Metallurgica*, 23(3):387 – 398, 1975.

[76] K. G. F. Janssens, D. Raabe, E. Kozeschnik, M. A Miodownik, and B. Nestler. *Computational materials engineering: an introduction to microstructure evolution*. Academic Press, 2010.

[77] M. A. Miodownik. A review of microstructural computer models used to simulate grain growth and recrystallisation in aluminium alloys. *Journal of Light Metals*, 2(3):125–135, 2002.

[78] R. B. Potts. Some generalized order-disorder transformations. In *Proceedings of the Cambridge Philosophical Society*, volume 48, pages 106–109. Cambridge Univ Press, 1952.

[79] M.P Anderson, D.J Srolovitz, G.S Grest, and P.S Sahni. Computer simulation of grain growthi. kinetics. *Acta metallurgica*, 32(5):783–791, 1984.

[80] M.P Anderson, D.J Srolovitz, G.S Grest, and P.S Sahni. Computer simulation of grain growth–i. kinetics. *Acta Metallurgica*, 32(5):783 – 791, 1984.

[81] M.P. Anderson, G.S. Grest, and D.J. Srolovitz. Grain growth in three dimensions: A lattice model. *Scripta Metallurgica*, 19(2):225 – 230, 1985.

[82] M.P. Anderson, G.S. Grest, R.D. Doherty, Kang Li, and D.J. Srolovitz. Inhibition of grain growth by second phase particles: Three dimensional monte carlo computer simulations. *Scripta Metallurgica*, 23(5):753 – 758, 1989.

[83] D.J. Srolovitz, G.S. Grest, and M.P. Anderson. Computer simulation of recrystallizationi. homogeneous nucleation and growth. *Acta metallurgica*, 34(9):1833–1845, 1986.

[84] D.J. Srolovitz, M.P. Anderson, G.S. Grest, and P.S. Sahni. Grain growth in two dimensions. *Scripta Metallurgica*, 17(2):241 – 246, 1983.

[85] D.J Srolovitz, M.P Anderson, P.S Sahni, and G.S Grest. Computer simulation of grain growth–ii. grain size distribution, topology, and local dynamics. *Acta Metallurgica*, 32(5):793 – 802, 1984.

[86] D.J. Srolovitz, M.P. Anderson, G.S. Grest, and P.S. Sahni. Computer simulation of grain growth–iii. influence of a particle dispersion. *Acta Metallurgica*, 32(9):1429 – 1438, 1984.

[87] D.J Srolovitz, G.S Grest, and M.P Anderson. Computer simulation of grain growth – v. abnormal grain growth. *Acta Metallurgica*, 33(12):2233 – 2247, 1985.

[88] D.J. Srolovitz, G.S. Grest, and M.P. Anderson. Computer simulation of recrystallization – i. homogeneous nucleation and growth. *Acta Metallurgica*, 34(9):1833 – 1845, 1986.

[89] D.J Srolovitz, G.S Grest, M.P Anderson, and A.D Rollett. Computer simulation of recrystallization – ii. heterogeneous nucleation and growth. *Acta Metallurgica*, 36(8):2115 – 2128, 1988.

[90] G.S. Grest, D.J. Srolovitz, and M.P. Anderson. Computer simulation of grain growth – iv. anisotropic grain boundary energies. *Acta Metallurgica*, 33(3):509 – 520, 1985.

[91] P. Peczak and M.J. Luton. The effect of nucleation models on dynamic recrystallization i. homogeneous stored energy distribution. *Philosophical Magazine B*, 68(1):115–144, 1993.

[92] P. Peczak and M.J Luton. The effect of nucleation models on dynamic recrystallization ii. heterogeneous stored-energy distribution. *Philosophical Magazine B*, 70(4):817–849, 1994.

[93] D. Raabe. Scaling monte carlo kinetics of the potts model using rate theory. *Acta Materialia*, 48(7):1617 – 1628, 2000.

[94] J. A Glazier, M. P Anderson, and G. S Grest. Coarsening in the two-dimensional soap froth and the large-q potts model: a detailed comparison. *Philosophical Magazine B*, 62(6):615–645, 1990.

[95] A.D. Rollett, M.J. Luton, and David J. Srolovitz. Microstructural simulation of dynamic recrystallization. *Acta metallurgica et materialia*, 40(1):43–55, 1992.

[96] P. Peczak. A monte carlo study of influence of deformation temperature on dynamic recrystallization. *Acta Metallurgica et Materialia*, 43(3):1279 – 1291, 1995.

[97] F.J. Humphreys. Modelling mechanisms and microstructures of recrystallisation. *Materials Science and Technology*, 8(2):135–144, 1992.

[98] C.E. Krill III and L.-Q. Chen. Computer simulation of 3-d grain growth using a phase-field model. *Acta Materialia*, 50(12):3059 – 3075, 2002.

[99] T. Takaki, Y. Hisakuni, T. Hirouchi, A. Yamanaka, and Y. Tomita. Multi-phase-field simulations for dynamic recrystallization. *Computational Materials Science*, 45(4):881 – 888, 2009.

[100] V. Tikare, E.A. Holm, D. Fan, and L.-Q. Chen. Comparison of phase-field and potts models for coarsening processes. *Acta Materialia*, 47(1):363 – 371, 1998.

[101] M. T Lusk. A phase–field paradigm for grain growth and recrystallization. *Proceedings of the Royal Society of London. Series A: Mathematical, Physical and Engineering Sciences*, 455(1982):677–700, 1999.

[102] Y. Suwa, Y. Saito, and H. Onodera. Phase-field simulation of recrystallization based on the unified subgrain growth theory. *Computational Materials Science*, 44(2):286 – 295, 2008.

[103] M. E. Gurtin and M. T. Lusk. Sharp-interface and phase-field theories of recrystallization in the plane. *Physica D: Nonlinear Phenomena*, 130(1):133 – 154, 1999.

[104] K. Piekoś, J. Tarasiuk, K. Wierzbanowski, and B. Bacroix. Generalized vertex model of recrystallization–application to polycrystalline copper. *Computational Materials Science*, 42(4):584–594, 2008.

[105] K. Nakashima, T. Nagai, and K. Kawasaki. Scaling behavior of two-dimensional domain growth: Computer simulation of vertex models. *Journal of Statistical Physics*, 57(3-4):759–787, 1989.

[106] K. Kawasaki, T. Nagai, and K. Nakashima. Vertex models for two-dimensional grain growth. *Philosophical Magazine B*, 60(3):399–421, 1989.

[107] D. Weygand, Y. Brechet, and J. Lepinoux. A vertex dynamics simulation of grain growth in two dimensions. *Philosophical Magazine B*, 78(4):329–352, 1998.

[108] D. Weygand, Y. Bréchet, J. Lépinoux, and W. Gust. Three-dimensional grain growth: a vertex dynamics simulation. *Philosophical Magazine B*, 79(5):703–716, 1999.

[109] R. Carel, C.V. Thompson, and H.J. Frost. Computer simulation of strain energy effects vs surface and interface energy effects on grain growth in thin films. *Acta materialia*, 44(6):2479–2494, 1996.

[110] J Von Neumann. *Theory of Self-Reproducing Automata*. University of Illinois Press, Champaign, IL, USA, 1966.

[111] D. Raabe. Cellular automata in materials science with particular reference to recrystallization simulation. *Annual review of materials research*, 32(1):53–76, 2002.

[112] D. Raabe and R. C Becker. Coupling of a crystal plasticity finite-element model with a probabilistic cellular automaton for simulating primary static recrystallization in aluminium. *Modelling and Simulation in Materials Science and Engineering*, 8(4):445, 2000.

[113] A.D. Rollett and D. Raabe. A hybrid model for mesoscopic simulation of recrystallization. *Computational Materials Science*, 21(1):69 – 78, 2001.

[114] R.L Goetz and V. Seetharaman. Modeling dynamic recrystallization using cellular automata. *Scripta Materialia*, 38(3):405 – 413, 1998.

[115] R. Ding and Z.X Guo. Coupled quantitative simulation of microstructural evolution and plastic flow during dynamic recrystallization. *Acta materialia*, 49(16):3163–3175, 2001.

[116] H. Hallberg, M. Wallin, and M. Ristinmaa. Simulation of discontinuous dynamic recrystallization in pure cu using a probabilistic cellular automaton. *Computational Materials Science*, 49(1):25 – 34, 2010.

[117] H.W. Hesselbarth and I.R. Gobel. Simulation of recrystallization by cellular automata. *Acta Metallurgica et Materialia*, 39(9):2135 – 2143, 1991.

[118] Koenraad GF Janssens. Random grid, three-dimensional, space-time coupled cellular automata for the simulation of recrystallization and grain growth. *Modelling and Simulation in Materials Science and Engineering*, 11(2):157, 2003.

[119] R. Logé, M. Bernacki, H. Resk, L. Delannay, H. Digonnet, Y. Chastel, and T. Coupez. Linking plastic deformation to recrystallization in metals using digital microstructures. *Philosophical Magazine*, 88(30-32):3691–3712, 2008.

[120] B. Merriman, J. K Bence, and S. J Osher. Motion of multiple junctions: A level set approach. *Journal of Computational Physics*, 112(2):334–363, 1994.

[121] T. Takaki, A. Yamanaka, Y. Higa, and Y. Tomita. Phase-field model during static recrystallization based on crystal-plasticity theory. *Journal of Computer-Aided Materials Design*, 14(1):75–84, 2007.

[122] T. Takaki and Y. Tomita. Static recrystallization simulations starting from predicted deformation microstructure by coupling multi-phase-field method and finite element method based on crystal plasticity. *International Journal of Mechanical Sciences*, 52(2):320–328, 2010.

[123] B. Radhakrishnan, G.B Sarma, and T. Zacharia. Modeling the kinetics and microstructural evolution during static recrystallizationmonte carlo simulation of recrystallization. *Acta materialia*, 46(12):4415–4433, 1998.

[124] B. Radhakrishnan and G.B Sarma. Coupled simulations of texture evolution during deformation and recrystallization of fcc and bcc metals. *Materials Science and Engineering: A*, 494(1):73–79, 2008.

[125] Hongwei Li, Chuan Wu, and He Yang. Crystal plasticity modeling of the dynamic recrystallization of two-phase titanium alloys during isothermal processing. *International Journal of Plasticity*, 2013.

[126] Arthur A. Brown and Douglas J. Bammann. Validation of a model for static and dynamic recrystallization in metals. *International Journal of Plasticity*, 32(0):17 – 35, 2012.

110

[127] Namin Xiao, Chengwu Zheng, Dianzhong Li, and Yiyi Li. A simulation of dynamic recrystallization by coupling a cellular automaton method with a topology deformation technique. *Computational Materials Science*, 41(3):366–374, 2008.

[128] R.C. Pond and S.M. Casey. Topological theory of line-defects on crystal surfaces, and their interactions with bulk and interfacial defects. In *Equilibrium Structure and Properties of Surfaces and Interfaces*, pages 139–174. Springer, 1992.

[129] R.J. Asaro and A. Needleman. Overview no. 42 texture development and strain hardening in rate dependent polycrystals. *Acta Metallurgica*, 33(6):923 – 953, 1985.

[130] R.W. Cahn. A new theory of recrystallization nuclei. *Proceedings of the Physical Society. Section A*, 63(4):323, 1950.

[131] J.E. Bailey and P.B. Hirsch. The recrystallization process in some polycrystalline metals. *Proceedings of the Royal Society of London. Series A. Mathematical and Physical Sciences*, 267(1328):11–30, 1962.

[132] W. Roberts and B. Ahlblom. A nucleation criterion for dynamic recrystallization during hot working. *Acta Metallurgica*, 26(5):801 – 813, 1978.

[133] R. Sandstrom and R. Lagneborg. A controlling factor for dynamic recrystallisation. *Scripta Metallurgica*, 9(1):59 – 65, 1975.

[134] Lazar Simkhovich Shvindlerman. *Grain boundary migration in metals: thermodynamics, kinetics, applications*, volume 9. CRC PressI Llc, 1999.

[135] MF Ashby. The deformation of plastically non-homogeneous materials. *Philosophical Magazine*, 21(170):399–424, 1970.

[136] J.F. Nye. Some geometrical relations in dislocated crystals. *Acta Metallurgica*, 1(2):153 – 162, 1953.

[137] CS Hartley and Y Mishin. Characterization and visualization of the lattice misfit associated with dislocation cores. *Acta Materialia*, 53(5):1313–1321, 2005.

[138] A. Arsenlis and D.M. Parks. Crystallographic aspects of geometrically-necessary and statistically-stored dislocation density. *Acta Materialia*, 47(5):1597 – 1611, 1999.

[139] M. Taheri, H. Weiland, and A. Rollett. A method of measuring stored energy macroscopically using statistically stored dislocations in commercial purity aluminum. *Metallurgical and Materials Transactions A*, 37(1):19–25, 2006.

111

[140] T. Sakai. Dynamic recrystallization microstructures under hot working conditions. *Journal of Materials Processing Technology*, 53(12):349 – 361, 1995.

[141] R.K. Mishra A. Brahme, Y. Staraselski and K. Inal. A New Model to Predict Grain Nucleation during Dynamic Recrystallization. In *The 9th International Conference on Magnesium Alloys and their Applications (Mg 2012)*, 2012.

[142] K.G.F. Janssens. An introductory review of cellular automata modeling of moving grain boundaries in polycrystalline materials. *Mathematics and Computers in Simulation*, 80(7):1361 – 1381, 2010.

[143] A. Brahme, Y. Staraselski, K. Inal, and R. K. Mishra. Determination of the minimum scan size to obtain representative textures by electron backscatter diffraction. *Metallurgical and Materials Transactions A*, 43(13):5298–5307, 2012.

[144] K. Inal, P.D. Wu, K.W. Neale, and S.R. MacEwen. Numerical simulation of large deformation polycrystalline plasticity. *Mathematical Modelling in Metal Processing and Manufacturing - COM2000. Ottawa*, 2000.

[145] S. R Agnew and Ö. Duygulu. Plastic anisotropy and the role of non-basal slip in magnesium alloy az31b. *International journal of plasticity*, 21(6):1161–1193, 2005.

[146] S.M. Fatemi-Varzaneh, A. Zarei-Hanzaki, and H. Beladi. Dynamic recrystallization in az31 magnesium alloy. *Materials Science and Engineering: A*, 456(1):52–57, 2007.

[147] XY Lou, Min Li, RK Boger, SR Agnew, and RH Wagoner. Hardening evolution of az31b mg sheet. *International Journal of Plasticity*, 23(1):44–86, 2007.

[148] T. Al-Samman and G. Gottstein. The influence of straib path on texture evolution in magnesium alloy az31. In K.U. Kainer, editor, *Magnesium: Proceedings of the 7th International Conference on Magnesium Alloys and Their Applications*, pages 553–559. Wiley, 2007.

[149] M.R. Barnett. Twinning and the ductility of magnesium alloys: Part ii.contraction twins. *Materials Science and Engineering: A*, 464(1):8–16, 2007.

[150] T. Sakai and J.J. Jonas. Overview no. 35 dynamic recrystallization: Mechanical and microstructural considerations. *Acta Metallurgica*, 32(2):189 – 209, 1984.

[151] M.J. Luton and C.M. Sellars. Dynamic recrystallization in nickel and nickel-iron alloys during high temperature deformation. *Acta Metallurgica*, 17(8):1033–1043, 1969.